Schweizerische Eidgenossenschaft
Confédération suisse
Confederazione Svizzera
Confederaziun svizra

Départmenet fédéral de l'environnement, des transports,
de l'énergie et de la communication DETEC

Ofiice fédéral de l'énergie OFEN

Rapport annuel 2010

Dimensionnement des galeries et puits blindés

Design of steel lined pressure tunnels and shafts

Mandant:
Office fédéral de l'énergie OFEN
Programme de recherche Force hydraulique
CH-3003 Berne
www.bfe.admin.ch

Cofinancement:
Competence Center for Energy and Mobility CCEM-CH, CH-5232 Villigen PSI

Mandataire:
Ecole Polytechnique Fédérale de Lausanne EPFL
Laboratoire de Constructions Hydrauliques LCH
Station 18
CH-1015 Lausanne
lchwww.epfl.ch

Auteurs:
Fadi Hachem, EPFL-LCH, fadi.hachem@epfl.ch
Prof. Dr. Anton Schleiss, EPFL-LCH, anton.schleiss@epfl.ch

Responsable de domaine de l'OFEN: Dr. Michael Moser
Chef de programme de l'OFEN: Dr. Klaus Jorde
Numéro du contrat et du projet de l'OFEN: SI/500169-01 / SI/500169

Office Fédérale de l'Energie (OFEN)

- Rapport d'avancement – 2010

Projet de recherche

Dimensionnement des galeries et puits blindés

(Design of steel lined pressure tunnels and shafts)

Lausanne, November 2010

EPFL Ecole Polytechnique Fédérale de Lausanne
ENAC Faculté Environnement Naturel Architectural et Construit
IIC Institut d'Ingénierie Civil
LCH Laboratoire de Constructions Hydrauliques

EPFL ENAC IIC LCH, Bât. GC A3 504
Station 18
CH – 1015 Lausanne
Tél: 021 693 2385 Fax: 021 693 2264 E-mail: secretariat.lch@epfl.ch

ÉCOLE POLYTECHNIQUE FÉDÉRALE DE LAUSANNE

Table of content

List of Figures

Sommaire

En raison de la forte demande de l'énergie de pointe, les centrales hydro-électriques doivent opérer à des vitesses variables pour assurer l'équilibre de la production et de la demande avec efficacité, flexibilité et sécurité. Les projets de pompage-turbinage ont gagné ainsi une importance majeure vu leur capacité à produire l'énergie dans un temps relativement court.

Un consortium technique nommé *CCEM-HydroNet* a été mis en place pour définir une nouvelle méthodologie pour le dimensionnement, la fabrication, l'opération, l'auscultation et le contrôle des centrales hydro-électriques de pompage-turbinage. L'objectif stratégique de ce consortium est de maintenir la position privilégiée de la Suisse dans le domaine de la production hydro-électrique et dans l'exportation de la haute technologie.

Le sujet de cette thèse fait partie de la branche de génie civil du consortium et peut se résumer en deux points principaux:

- L'analyse du comportement des galeries et puits blindés sous l'action des pressions hydrauliques dynamiques qui agissent sur la paroi interne du blindage durant les épisodes transitoires.
- La surveillance et le contrôle non-intrusifs et à temps réel de ces ouvrages avec le minimum d'intervention humaine et sans arrêt de production des centrales dont ils sont associés.

Une attention particulière est consacrée à l'interaction Fluide-Structure ainsi qu'au phénomène de la propagation des ondes de pression dans l'eau connues sous le nom de coups de bélier. L'exploitation des résultats des essais effectués sur modèle physique à échelle réduite ainsi que l'analyse des mesures effectuées sur prototype nous permettent de suivre la propagation de ces ondes, de déterminer leur vitesse et degré d'atténuation et de comprendre leur interaction avec la structure (blindage, béton et rocher) qui les entoure. Un modèle théorique pourra ainsi être développer en considérant cette interaction Fluide-Structure durant les fluctuations de pressions provoquées par les coups de bélier. Le calage et la validation d'un tel modèle théorique permettra de développer des nouvelles méthodes et procédures de dimensionnement pour les puits blindés. Elles seront basées sur le comportement contraintes-déformations et sur la théorie de rupture fragile du chemisage en acier à haute résistance. Les résultats de ces analyses représentent une des cibles cruciales de la production hydro-électrique en Suisse après la rupture, en décembre 2000 , du puits blindés de l'aménagement *Cleuson-Dixence* suite au développement et propagation des micro-fissures dans les soudures de l'acier du blindage de haute résistance.

En plus d'une procédure moderne de dimensionnement pour le calcul des nouvelles constructions, l'auscultation des galeries et puits blindés existants s'avèrent primordiale pour la métrise du risque résiduel lié à la rupture de ces constructions sous l'action de la pression interne dynamique de l'eau. Une méthode de surveillance non-intrusive est proposée dans le but de détecter à temps réel, l'existence, l'endroit et la sévérité d'une éventuelle faiblesse locale de la rigidité de la paroi du puits. L'idée clef de cette méthode repose sur l'analyse et le traitement des signaux de pression dynamique, d'acoustique et de la vibration radiale du blindage mesurés aux deux extrémités accessible du puits.

Ce projet de recherche vise donc à développer de nouvelles et innovatrices procédures de dimensionnement et de surveillance des galeries et puits blindés. Les points suivants sont traités dans le cadre d'une thèse:

1- **Etude de littérature** qui indique les paramètres principaux d'intérêt du problème, les lacunes et déficits des méthodes de dimensionnement et de surveillance existantes ainsi que les nouvelles pistes à conquérir.
2- **Bases théoriques** ayant comme objectif de décrire la physique derrière les différents phénomènes envisagés.
3- **Mesures sur prototype** effectuées sur le puits blindés de la centrale électrique de pompage-turbinage de Grimsel II (*KWO*). Deux sections de mesures de ce puits (une à l'entrée de la centrale et une autre à coté de la chambre d'équilibre) sont équipées par des capteurs de pression, par des géophones et par des hydrophones. L'acquisition et le traitement de ces mesures permettent de valider les procédures de calcules et d'auscultation à l'échelle du prototype.
4- **Modélisation physique à échelle réduite** effectuée sur une conduite en acier constituée par l'assemblage de plusieurs bouts. La simulation d'une faiblesse de rigidité de la paroi de la conduite est réalisée en remplaçant un bout de conduite en acier (de 50 ou 100 cm de long) avec un autre fabriqué en PVC ou en aluminium. Plusieurs configurations de la conduite d'essai sont testées sous l'action des coups de bélier produits par la fermeture rapide d'une vanne installée à son extrémité aval.
5- **Développement d'un modèle théorique** basé sur les connaissances actuelles et validé par l'analyse des résultats des essais physiques et mesures sur prototype.
6- **Développement d'une méthode de surveillance** à temps réel de la rigidité du système complexe (acier, béton et rocher) de la paroi des galeries et puits blindés. Cette méthode est basée sur le traitement et l'analyse des signaux générés durant les épisodes transitoires de la pression hydraulique interne.
7- **Rapport de thèse** et **publications scientifiques**.

Ce rapport décrit brièvement les objectifs de la thèse et résume les travaux effectués durant la période entre août 2009 et août 2010.

Mots clés : *Centrales hydro-électriques de pompage-turbinage, dimensionnement des puits blindés, structure composée, pression interne transitoire, mécanique de rupture fragile, coups de bélier, mesures sur prototype, propagation des ondes, traitement des signaux, modèle théorique, surveillance, faiblesse de la rigidité de la paroi.*

1. Recall

Modern power plants are expected to operate at variable speed in a wide range of output power with improved efficiency, flexibility and safety. Therefore, the pumped storage power generation has gained in importance since it allows storing and generating high peak energy by moving water back and forth between two reservoirs at different elevations.

A project consortium, called ***HydroNet*** (*Modern Methodologies for Design, Manufacturing and Operation of Pumped-Storage Power Plant*) (Figure 1.1) has been built aiming to converge towards a consistent standardized methodology for design, manufacturing, operation, monitoring and control of pumped storage power plants in order to give new impulsions in the hydropower technology and maintain the strong position of Switzerland in peak hydropower production as well as in the exportation of high valued technology.

One of the civil engineering field involved in this consortium is ***the design and control of pressurized shafts and tunnels*** with a special focus on safety. Since 1980's, no significant fundamental research has been performed aiming to integrate design with interaction between water, steel lining and rock mass. The results of these investigations stand for a crucial target in Switzerland since the collapse of the shallow buried pressure shaft of *Cleuson-Dixence* hydropower plant in December 2000.

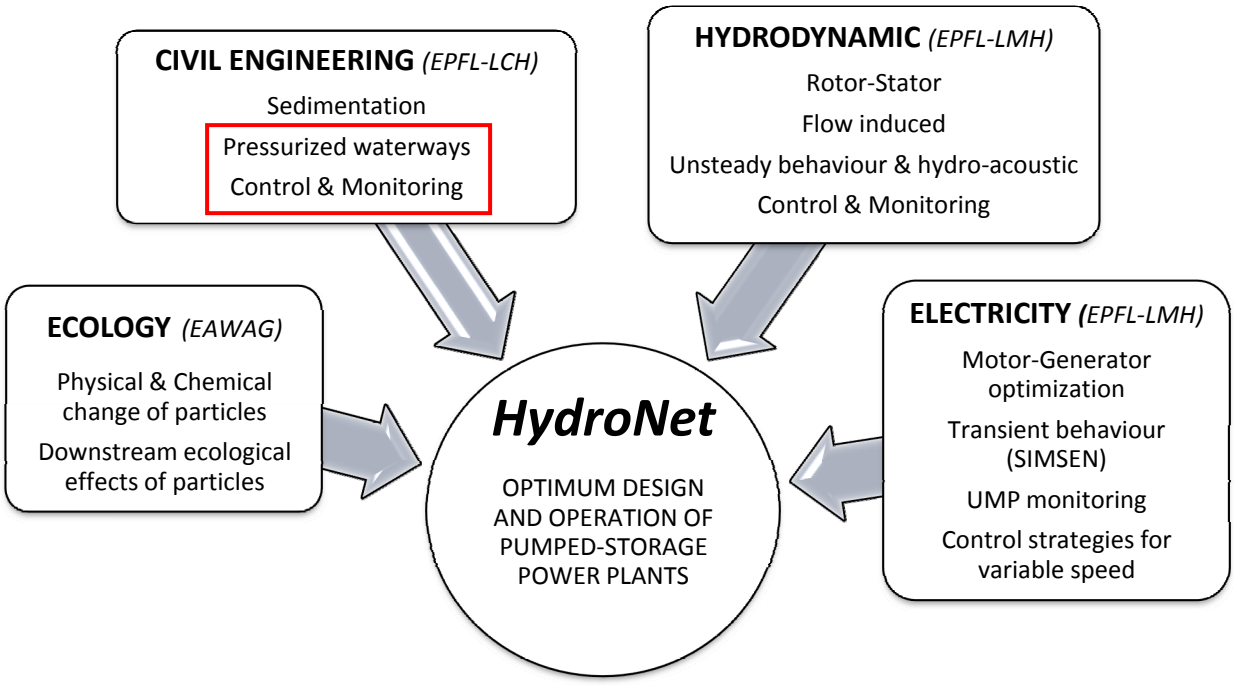

Figure 1.1 : Partners and main objectives of *HydroNet* project consortium

2. Practical relevance and main objectives of this research

This research project will end to some practical applications, mainly:

1- **Development of new theoretical model** based on the actual state-of–the-art knowledge validated by the analysis of results of the scaled model physical tests and the real prototype measurements during severe interior hydraulic transients.

2- **Relevant monitoring methods** for steel lined tunnels and shafts using non-intrusive instrumentation. These methods will detect in real time the existence, location and severity of local drop of stiffness of the structure wall. This aims to predict maintenance works that minimize the risk of a catastrophic failure.

The main objectives of this research project are summarized in Figure 2.1.

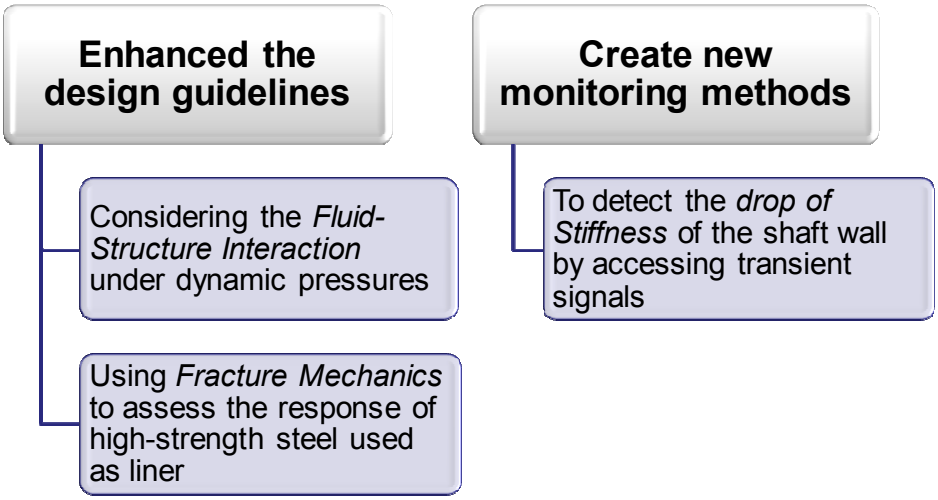

Figure 2.1 : Main objectives of the research project

The research plan has been submitted to the Director of the ''Doctoral Program in Structures – EPFL'' in the 8th August 2008. It was accepted by the dean of the doctoral school in the 22nd August 2008.

3. State-of-the-art

The State-of-the-art of the thesis subject has been prepared in years 2008 and 2009 and has been published in the *International Journal on Hydropower & Dams* in 2009. It covers the actual knowledge of the essential design requirements related to the steel lining structure. To understand the behaviour of such composite structure, a discussion has been done on the materials properties and the way that may influence the resistance of the structure. It was shown that the actual design is based upon the same concept of any composite structure where the need for a full understanding of the behaviour of its three composing materials: Steel, Concrete and Rock is essential for any attempt for design. It is known that the steel lining must carry loads without excessive yielding or rupture and that the geological and geotechnical parameters of the hosted rock are the key issue for determining the load sharing ratios between the composite materials of the steel lining system.

4. Gaps of knowledge

The actual design rules for pressurized steel lined tunnels and shafts are the result of research that has been conducted mainly during the period of construction of hydropower plant in Europe between the 40's and the 80's. Since then, no significant fundamental works have been performed aiming to integrate design with interaction between lining and rock mass during transients nor to develop modern monitoring methods.

The true behaviour of combined steel-concrete-rock linings is not yet fully understood, especially the influence of severe transient flow phenomena, such as water-hammer effects, on the short and long term structural behaviour, fatigue, and safety of the lining. The existing design methods have been based on the idea of keeping the allowable stress in steel liner below yielding point and respecting some construction details and tolerances to minimize stress raiser points. These design methods and safety assessment have become insufficient since the beginning of use of very high strength steel liners which have high risk of brittle failure and fatigue.

Traditionally, well equipped steel-lined shafts and tunnels are monitored by a set of pressure sensors, water level measurements and downstream–upstream flow meters. Pressure sensing devices are normally used to check the magnitude of the dynamic pressures relative to a predefined serviceability value with no further pressure signal processing. If the water flow velocity exceeds a certain threshold, indicating a possible failure, a security shut-off valve closes automatically limiting the volume of water leaking out from the failure. Nevertheless, and even in this case, catastrophic failure consequences can occur since the volume of leaking water between the valve and the failure location may still be very high. Any additional investigation of the steel-liner regarding excessive local deformations and steel yielding requires a dewatering of the conveying system for visual checking. Such inspection is often awkward due to the hostile conditions. Furthermore, no information can be obtained easily about the stiffness of the rock mass surrounding the steel-liner.

5. Theoretical model

A Fluid-Structure Interaction (*FSI*) theoretical model with axisymmetrical behaviour and longitudinal motion has been prepared. The actual model based on static pressure sharing between the different parts of the tunnel wall has been enhanced according to Figure 5.1. This new model can detect the compressional water mode and the radial and axial propagation modes in the steel liner and in the far field rock zone.

The time-dependent stress diagrams, resulting from the *FSI* problem can be used as input for the deterministic and probabilistic fracture mechanics models of steel liners. The physical and prototype measurements will be used for calibration and verification.

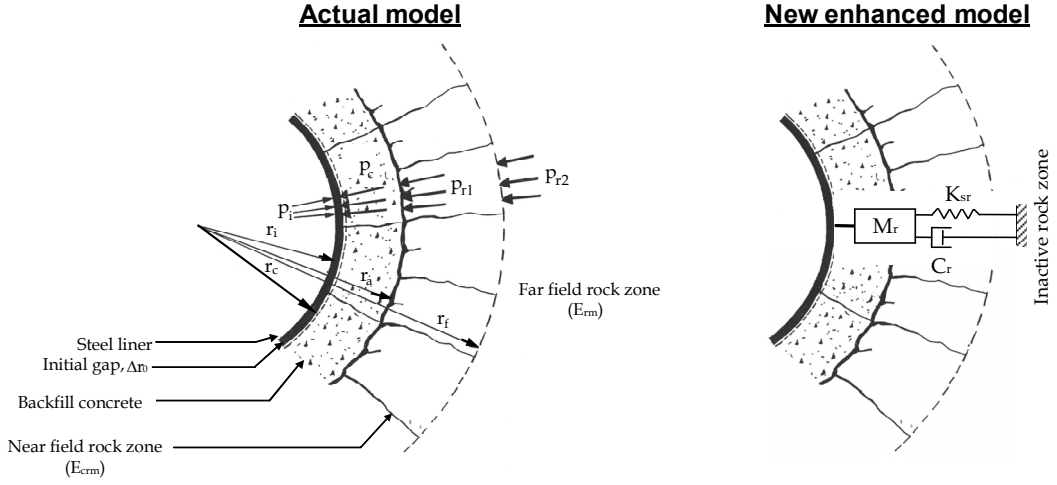

Figure 5.1 : The two cross-sectional views of the actual and enhanced theoretical model of pressurized steel lined tunnels and shafts

The new theoretical model has been discussed in detail in the scientific paper entitled: "A review of wave celerity in frictionless and axisymmetrical steel-lined pressure tunnels" which has been submitted and accepted for publication in the *Journal of Fluids and Structures*.

6. Physical scaled model

An experimental facility was assembled at the Laboratory of Hydraulic Machines of EPFL (Ecole Polytechnique Fédérale de Lausanne). This facility was specially designed for detecting the change of wall stiffness of a test pipe using recorded pressure data generated either by an external water pressure excitation source or by a rapid change of the flow rate's producing water-hammer phenomena inside the pipe. The configuration of the experimental set-up is shown in Figure 6.1 and presented more in detail in Appendix A.1.

It consists of a test pipe with an internal diameter of 150 mm and a length of 6.25 m supplied with water by a reservoir and a variable speed pump. The pipe is divided into several reaches of 0.5 m and 1.0 m length fitted together with flanges having an external diameter of 285 mm and a thickness of 24 mm. The flanges are also used to rigidly fix the test pipe along its length in order to minimize any longitudinal and transversal movements during test events. On the 10 m supply conduit, an electromagnetic flow meter is placed to measure the steady state flow. On the highest point of this conduit, an air purge valve is installed to evacuate the captured air inside the test rig. A first control and security valve followed by an elastic deformable joint (TUBOFLEX) are located at the downstream end of the supply conduit, which is protected against water-hammer by a pressurized air vessel. The downstream end of the test pipe is equipped with a shut-off valve operated by an air jack. It is followed by a purge valve, an elastic TUBOFLEX joint and a second control valve located at the entrance of the supply reservoir. The external pressure excitation, transmitted to the water through the jack axis, and the closure of the shut-off valve are carried out automatically by the air jack with input and output electro-valves. The volume of air needed to activate the jack is provided by an air compressor with a constant pressure of 10 bars. The opened and closed states of the shut-off valve are detected by two diffuse sensors with an infrared beam. The data acquisition system comprises: (i) two pressure transducers (HKM-375M-7-BAR-A, Kulite) with a pressure range from 0 to 7 bars and an accuracy of 0.5%, (ii) a NI-USB-6259 acquisition card M series with 32 analogue input channels and 2 analogue output channels to activate the two electro-valves of the shut-off valve, and (iii) a notebook computer connected to the acquisition card through a USB cable. The sampling frequency was fixed to 15 KHz. *LabView* 8.6, *MATLAB* 2008b and *Diadem* 11.0 software were used for acquiring, controlling and processing the experimental data.

Five pipe configurations were tested with approximately the same initial steady flow conditions, the same air pressure in the compressor, and the same mean pressure at the entrance of the test pipe. The basic configuration of the test pipe, named "Steel," corresponds to steel pipe reaches of 100 and 50 cm length with 4.5 mm wall thickness arranged in a basic configuration according to Figure 6.2. In the configuration "Steel+Alu1," the first 50 cm pipe reach (the first pipe reach is that nearest the air vessel) is replaced by an aluminum pipe with 5 mm wall thickness. In the configurations "Steel+PVC1, 2 or 3" the first, second or third 50 cm long pipe reach is replaced by a 5 mm thick PVC pipe. For each test pipe configuration, many repetitive tests were carried out

giving a total number of 67 tests (19 for “Steel,” 6 for “Steel+Alu1,” 18 for “Steel+PVC1,” 12 for “Steel+PVC2” and 12 for “Steel+PVC3”).

A typical test result record of transient pressure p1 is shown in Figure 6.3. The processing of the first part of the signal that concerns the transient pressure induced by the external exciter has been done using the Fast Fourier Transform and the Wavelet filtering and decomposition techniques. The analysis aims to detect the existence, location and severity of the weak reach modelled by the PVC and the aluminium pipe reach. A scientific paper has been prepared and submitted to the *Journal of Hydraulic Engineering* and it is now under reviewing. The second part of the pressure signal (limited by the blue rectangle of dashed lines in Figure 6.3) shows small fluctuations induced by the water-hammer phenomenon and reflections from the weak reaches. The accessing of this part of signal is more difficult than the first part due to noise. Two conference papers have been prepared dealing with the water-hammer part of the signal. The first paper present a procedure to estimate the water-hammer wave speed in pipes and tunnels with local weak wall stiffness and the second propose a new monitoring method of steel-lined pressure shafts using Wavelet filtering and decomposition. The abstracts of these two papers have been accepted in September and October 2010. The full papers are ready to be submitted for reviewing by the end of this year. The thesis objectives and main outlines have been also presented in the First European IAHR Congress that was held in Edinburgh in 2010.

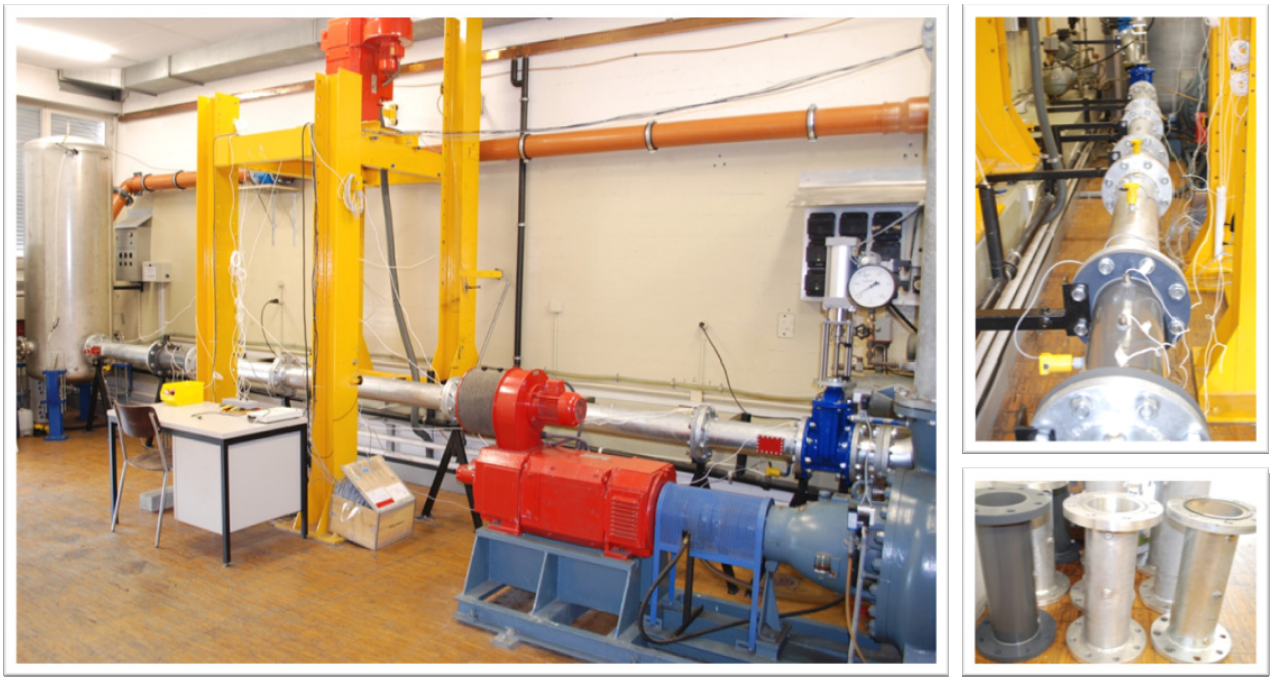

Figure 6.1 : Photos of the physical scaled model with the steel, PVC, and aluminum reaches

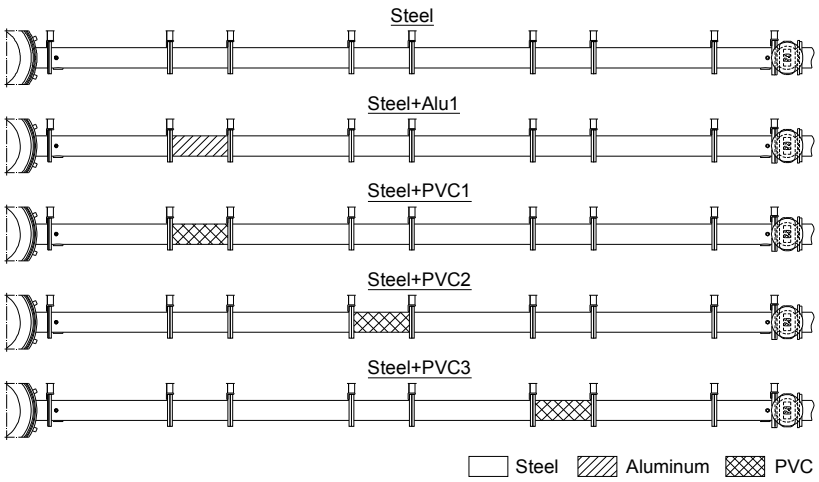

Figure 6.2 : The five different configurations of the test pipe.

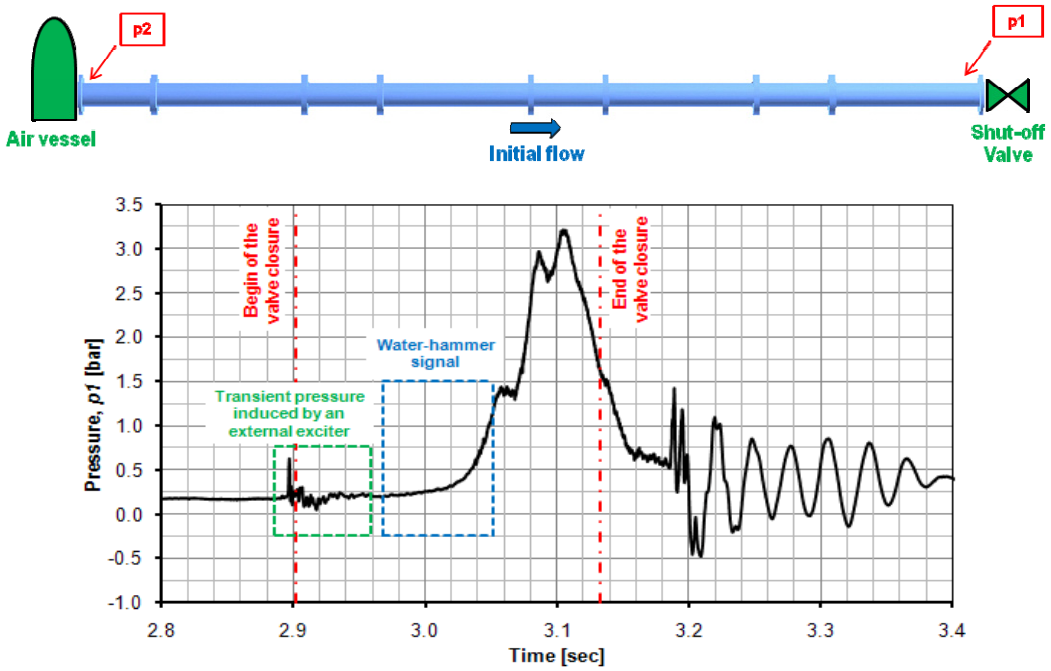

Figure 6.3 : A typical test result of the water-hammer transient pressure acquired by the pressure sensor p1 situated near the shut-off valve

7. Prototype measurements

The pressurized shaft of the high-pressure side of the pumping-storage hydropower plant of *Grimsel II* in Switzerland is now being equipped with pressure sensors, geophones and hydrophones sensors. The first version of the acquiring scheme has been prepared and is actually under testing process. A part of this scheme (measurement section in the power house, see Figure 7.1) can be now controlled and pressure and vibration signals can be retrieved on-line from *Grimsel II* to our laboratory in Lausanne.

The ongoing work will try to end the equipment works of the upper part of the shaft and by the end of 2010 and to validate the estimation procedure of the water-hammer wave speed. It will feed us also with additional information about the steepness, energy and dissipation of water-hammer wave generated during start-up and shut-down of pumps and turbines. The influence of the water temperature, turbidity, and the captured

air inside the shaft on the estimation of the wave speed will be also investigated. The localization procedure of weak reaches will be implemented in purpose to detect the position of some eventual geological and geotechnical weaknesses of the rock mass surrounding the steel liner. The estimated positions will be compared to the real ones which can be obtained from the existing as-built drawings of the shaft.

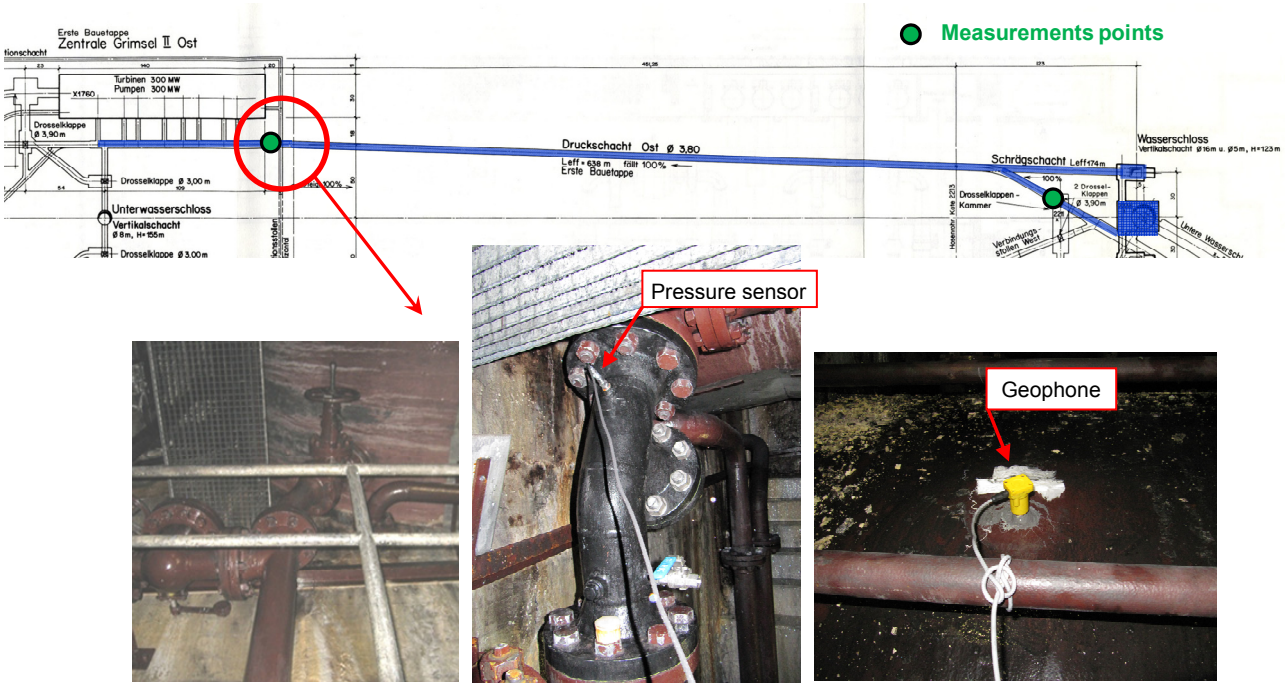

Figure 7.1 : The lower measurement section of the pressurized shaft in *Grimsel II* power house

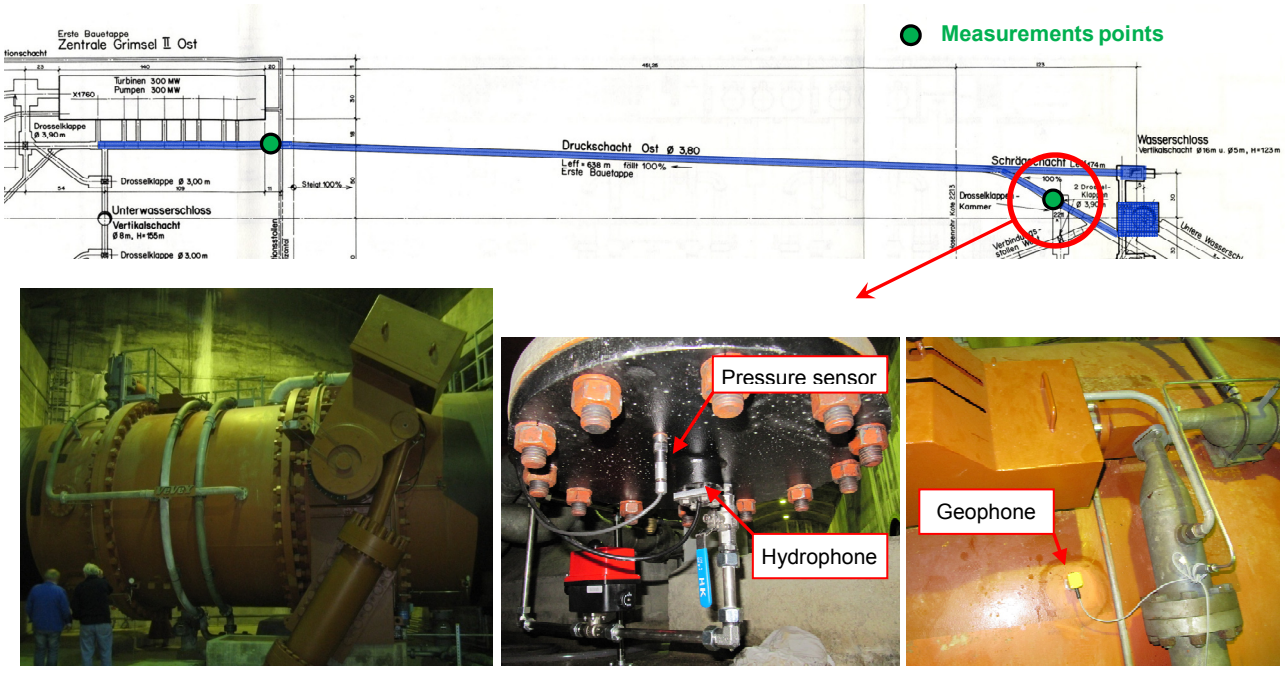

Figure 7.2 : The upper measurement section of the pressurized shaft in the shut-off valve gallery near the surge tank

8. Project timetable

The updated time schedule of the different phases of the project is the following :

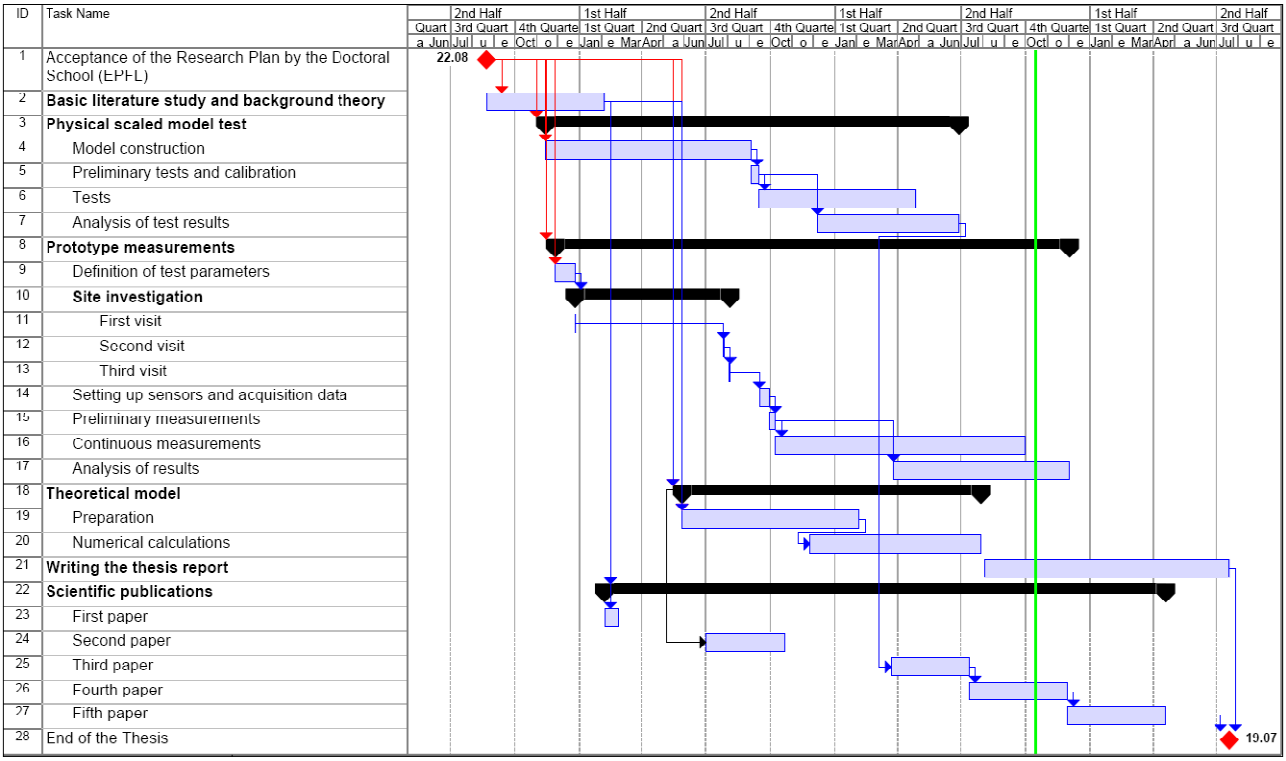

Figure 8.1 **:** Project timetable schedule

9. Follow-up of the project

Beside the following-up by the director of this research work, Prof. Anton Schleiss, this research project is supervised closely by Dr Erik Bollaert, senior research associates. Accordingly, progress meetings are planned regularly, every five to six weeks, with the research project director and the senior research associates.

One to two times a year, the progress state of the project will be presented as an internal conferences at LCH (Three internal conferences have been given till now on the 7th November 2008, on 18th September 2009 and on 27th August 2010). Furthermore, two intermediate reports have been submitted to the OFEN in August 2008 and in August 2009).

In the framework of the multidisciplinary CCEM-project, periodical sessions (2 per year) will be organized to share information and to discuss the progress of the project (five technical meetings have took place until now).

10. Collaboration

The academic program at EPFL gives the opportunity to researcher to collaborate with scientists worldwide by inviting them to spend some weeks at Lausanne. Mrs. Dídia Isabel Cameira Covas had accepted our invitation as academic guest at EPFL. We will have the pleasure to collaborate and discuss with her during her stay among us in November 2010. Mrs. Covas is an Assistant Professor at the Centro de Estudos e Hidrossistemas (CEHIDRO), Instituto Superior Técnico of Lisboa. She has been working in the water

transient field for the last 13 years including the unsteady friction modelling, pipe wall viscoelasticity, cavitation, frequency domain analysis and leak detection. During her stay in Lausanne, Mrs. Covas will give also a scientific conference entitled: "Effect of the pipe wall viscoelasticity and of unsteady friction on transient pressures: time-domain and frequency-domain analyses".

11. Publications

Demande de subside à l'OFEN (2008). *Projet de recherche, Dimensionnement des galeries et puits blindés*. Laboratoire de Constructions Hydrauliques (LCH).

Rapport d'avancement à l'OFEN (2009). *Projet de recherche, Dimensionnement des galeries et puits blindés*. Laboratoire de Constructions Hydrauliques (LCH).

Hachem, F. and Schleiss, A. (2009). The design of steel-lined pressure tunnels and shafts. *International Journal on Hydropower & Dams*, 16(3):142-151.

Hachem, F. and Schleiss, A. (2010). A review of wave celerity in frictionless and axisymmetrical steel-lined pressure tunnels. The *Journal of Fluids and Structures*, accepted for publication, 2010.

Hachem, F. and Schleiss, A. (2010). Detection of local wall stiffness drops in pipes using steep pressure wave excitation and wavelet decomposition. Under reviewing process in the Journal of Hydraulic Engineering, ASCE.

Hachem, F. and Schleiss, A. (2010). Physical tests estimating the water-hammer wave speed in pipes and tunnels with local weak wall stiffness. Under reviewing for the 2011 World Environmental & Water Resources Congress (*EWRI*), Palm Springs, California, May 22 – 26, 2011.

Hachem, F. and Schleiss, A. (2010). Monitoring of steel-lined pressure shafts using water-hammer records and wavelet filtering and decomposition. Under reviewing for the 34th IAHR Congress 2011, Brisbane, Australia, 26 June to 1 July, 2011.

Hachem, F. and Schleiss, A. (2010). Influence of local stiffness of conduits on water-hammer propagation signal. Proceedings of the First European IAHR Congress, Edinburgh, 2010.

12. Appendices

A.1 The construction drawings of the physical scaled model.

A.2 Publications 2010.

A.1

The construction drawings of the physical scaled model

ELEVATION VIEW

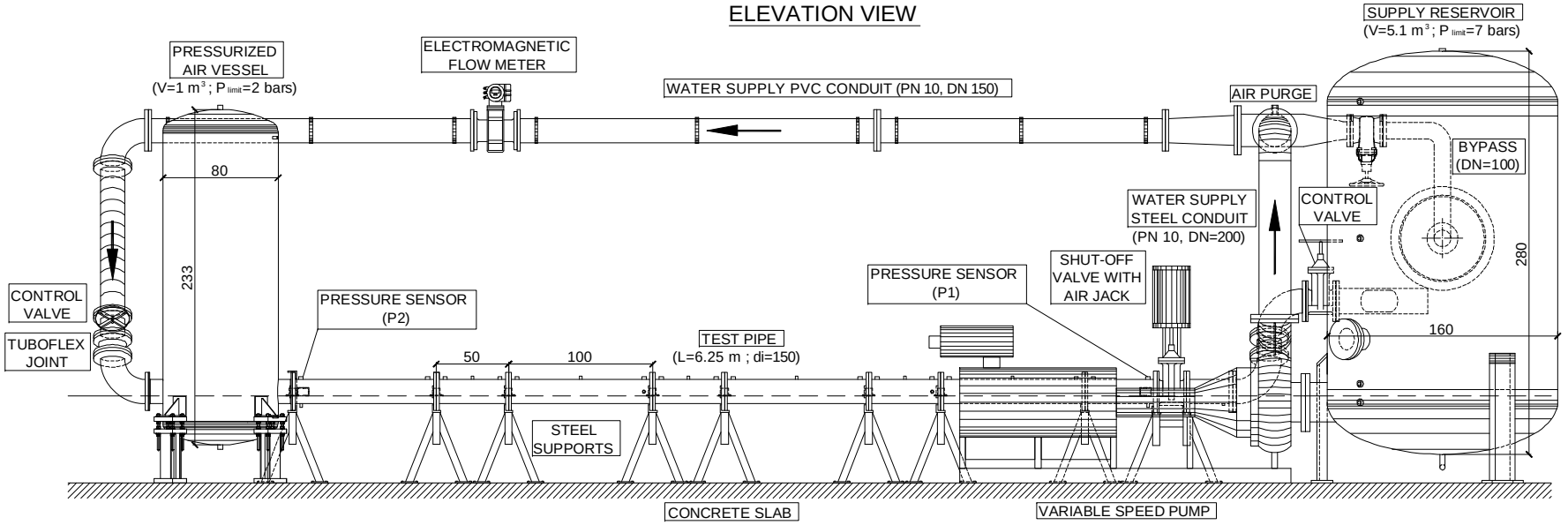

PLAN VIEW

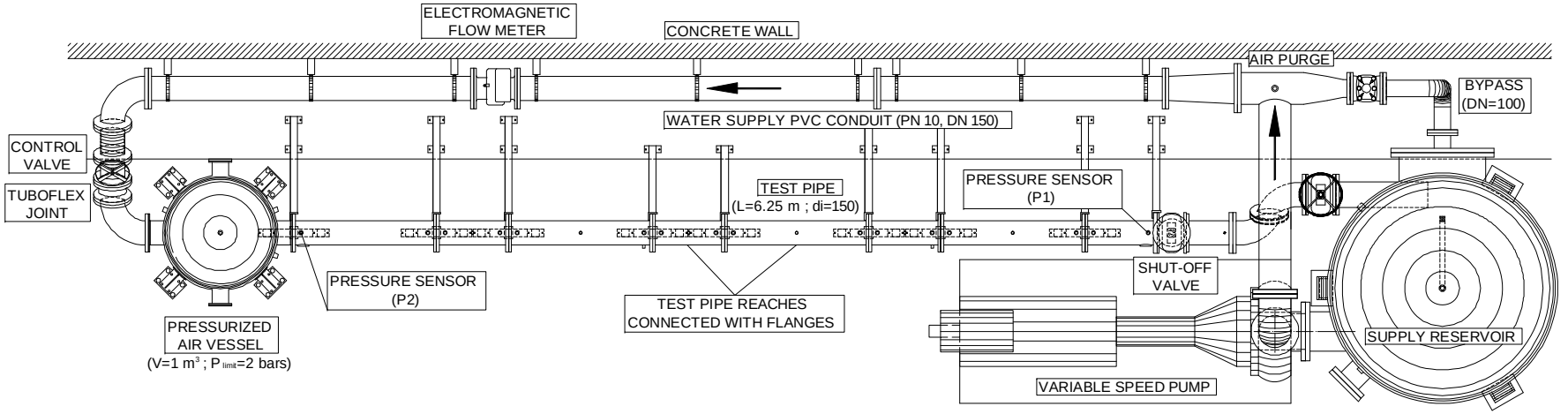

A.2

Publications 2010

A review of wave celerity in frictionless and axisymmetrical steel-lined pressure tunnels

F.E. Hachem*, A.J. Schleiss

Laboratory of Hydraulic Constructions, Ecole Polytechnique Fédérale de Lausanne, Station 18, 1015 Lausanne, Switzerland

Abstract

Generally applicable approaches for estimating the "quasi-static", that means without fluid-structure interaction, and frequency-dependent water-hammer-wave speed in steel-lined pressure tunnels are analyzed. The external constraints and assumptions of these approaches are discussed in detail. The reformulated formulas are then compared to commonly used expressions. Some special cases of wave speed calculation such as unlined pressure tunnels and open-air penstocks are investigated. The quasi-static wave speed is significantly influenced by the state of the backfill concrete and the near-field rock zone (cracked or uncracked). In the case when these two layers are cracked, the quasi-static wave speed is overestimated in between 1% and 8% compared to uncracked concrete and near-field rock layers. Depending on the stiffness of steel liner and penstock, the Fluid-Structure Interaction leads to significant difference in wave speeds values. Compared to the quasi-static case, the Fluid-Structure Interaction approach, applied to steel-lined tunnels, results in up to 13% higher wave speed values in the high frequency range (higher than 600 Hz) and up to 150% lower values for frequencies between 150 and 300 Hz in the considered test case.

Keywords: Water hammer; Steel-lined pressure tunnels; Quasi-static wave speed; Frequency-dependent wave speed; Fluid-Structure Interaction

1. Introduction

The quasi-static and frequency dependent wave speed of flow disturbances in pipes have been treated extensively for rigid, elastic and visco-elastic tube walls. Without considering Fluid-Structure Interaction (FSI), Halliwell (1963), Streeter (1963), Rieutord (1982), Wylie et al. (1993) and Ghidaoui et al. (2005) give, among others, good overviews on the different methods for wave speed estimation. FSI can be found in Rubinov and Keller (1971, 1978), Lavooij and Tijsseling (1991), and Tijsseling (1996). Unlike the case of open-air and thin-walled pipes, most formulae predicting the wave speed of flow disturbances in rock-bored tunnels and shafts (lined or unlined) have not been explicitly derived using clear definition of the external constraints. The most consistent approaches, without considering the FSI problem, can be found in Jaeger (1933), Halliwell (1963), Fanelli (1973), Bürmann (1975), and Suo (1990a). Considering FSI, references from the biomechanical domain such as Atabeck (1968) and Kuiken (1984, 1988) provide a rather complete 2-D calculation model. A 1-D mathematical model was also presented by Tijsseling (2007) describing the behaviour of thick-walled and liquid-filled pipes.

This paper focuses on the analysis of the wave speed propagation in rock-bored steel-lined tunnels and shafts. The purpose of it is to give: (a) a review of relevant contributions in deriving the wave speed formulae with clear definition of hypothesis and constraints, and (b) to extend the use of the FSI model, derived by Kuiken (1984), to the field of steel-

*Corresponding author.
E-mail address: fadi.hachem@a3.epfl.ch (F.E. Hachem).

lined tunnels and shafts. Some examples with a sensitivity analysis of the main parameters are also provided in order to compare the results obtained in the frequency domain with the classical approaches.

Nomenclature

a	quasi-static wave speed of water hammer (m/s)	f_y	yield strength of steel (MPa)
A	internal cross-sectional area of the steel liner (m^2)	i	the complex number $(-1)^{0.5}$
A_1 , A_2	factors defined in Eq. (3.3)	k	ratio of the reference wave speed (c_0) to the complex wave speed (c) (-)
A_3 , A_4	factors defined in Eq. (3.4)	K_r	parameter defined in Eq. (4.4) (N/m)
A_5 , A_6	factors defined in Eq. (3.5)	$Ks_{r,l}$	radial (resp. longitudinal) spring stiffness coefficient per unit area of the Kelvin model ($N/m/m^2$)
b	ratio of the internal radius of the pressure tunnel and the steel-liner thickness ($=p_i/t_s$) (-)	K_w	bulk modulus of water (MPa)
c	complex wave speed (m/s)	$M_{r,l}$	radial (resp. longitudinal) additional mass per unit area of the Kelvin model (kg/m^2)
c_{0eq}	equivalent reference wave speed defined in Eq. (4.6) (m/s)	p	water pressure in excess of the steady-state pressure p_0 used in the FSI case (MPa)
c_i	phase or group velocities of the i-th mode (m/s)	p_0	water pressure in the steady-state conditions used in the FSI case (MPa)
c_{gi}	group velocity of the i-th mode (m/s)	p_c	uniform pressure transmitted to backfill concrete at radius r_c (MPa)
c_{pi}	phase velocity of the i-th mode (m/s)	p_i	water pressure inside shafts and tunnels used in the quasi-static case (MPa)
c_0	reference wave speed (m/s)	p_{r1}	uniform pressure transmitted to the rock zone at radius r_a (MPa)
c_T	Speed of sound in unconfined water (m/s)	p_{r2}	uniform pressure transmitted to the rock zone at radius r_f (MPa)
$C_{r,l}$	radial (resp. longitudinal) frictional coefficient per unit area of the Kelvin model ($N.s/m/m^2$)	r	radius measured from tunnel axis (m)
D	complex integration constant (-)	r_c	internal radius of backfill concrete (m)
D_1 , D_2	undetermined complex constants of solution (-)	r_f	internal radius of the far-field rock zone (m)
D'	mode-dependent factor defined in Eq. (2.19)	r_a	internal radius of the near-field rock zone (m)
E_{app}	apparent elasticity modulus of rock mass (MPa)	r_i	internal radius of the steel liner (m)
E_c	elasticity modulus of the backfill concrete (MPa)	t	time (s)
E_s	elasticity modulus of steel liner (MPa)	t_s	steel liner or penstock wall thickness (m)
		u	water velocity in the axial direction of the tunnel (m/s)

E_{crm}	elasticity modulus of the near-field loosened rock zone (MPa)	u_f^s	axial displacement of the steel liner (m)
E_{rm}	elasticity modulus of the far-field rock zone (MPa)	u_r^s	radial displacement of the steel liner (m)
F_x	resultant of axial forces applied on the liner per unit area (MN/m^2)	v	water velocity in the radial direction of the tunnel (m/s)
F_r	resultant of radial forces applied on the liner per unit area (MN/m^2)	x	longitudinal coordinate according to the tunnel axis (m)
f	excitation frequency (Hz)	Λ_i	logarithmic decrement of the i-th propagating mode (-)
Δr_0	initial thermal gap between steel liner and backfill concrete (m)	ω	angular frequency of transient excitations ($=2\pi f$) (rd/s)
ρ_w	unit mass of water used in the quasi-static case (kg/m^3)	ζ	damping ratio for the Kelvin model (-)
σ_r	radial stress in the theory of thick-walled cylinder (MPa/m)	λ_i	wave length of the i-th propagating mode ($=c_1/f$) (m)
σ_t	tensile stress in the theory of thick-walled cylinder (MPa/m)	μ	dynamic viscosity of water (kg/m/s)
σ_l^0	initial longitudinal stress in the liner per unit length (MPa/m)	v_c	Poisson's ratio of backfill concrete (-)
σ_r^0	initial circumferential stress in the liner per unit length (MPa/m)	v_s	Poisson's ratio of steel (-)
σ_l^+	perturbation of longitudinal stress in the liner per unit length (MPa/m)	v_{rm}	Poisson's ratio of the near- and far-fields of the rock mass (-)
σ_r^+	perturbation of circumferential stress in the liner per unit length (MPa/m)		

2. Radial deformation of steel-lined pressure tunnels

2.1. *Compatibility equations of deformation at interfaces of radial symmetrical multilayer systems*

2.1.1. *Quasi-static case*

In general, the deformation of radial symmetrical multilayer systems is derived from compatibility conditions at the interfaces (Talobre, 1967; Schleiss, 1988). In the case of steel-lined pressure tunnels, three layer interfaces of radius r_c, r_a and r_f, as shown in Fig. 1(a), exist. The compatibility of radial deformation u_r at these three interfaces can be written as follows:

$$\begin{cases} u_r^s(r=r_c) - \Delta r_0 = u_r^c(r=r_c) \quad \text{with} \quad \Delta r_0 \geq 0, \\ u_r^c(r=r_a) = u_r^{\text{crm}}(r=r_a), \\ u_r^{\text{crm}}(r=r_f) = u_r^{\text{rm}}(r=r_f), \end{cases} \tag{2.1}$$

where, respectively, superscript s is related to steel liner, c to the backfill concrete, and crm and rm to the near- and far-field zones of the rock mass. The subscript r indicates deformations in the radial direction. In contact with colder water, the steel liner shrinks and an initial gap Δr_0 may occur between steel and backfill concrete. A typical value of Δr_0 equal to 0.25‰ of r_i is often used (Schleiss, 1988). In this paper, when the kinematic and dynamic effects of water and steel liner are considered (Fluid-Structure Interaction

phenomenon) under internal pressure, the steel liner is assumed to be in permanent contact with the backfill concrete and the gap can be thus ignored.

For any layer j, considered as a thick circular cylinder in axisymmetrical behaviour and with elasticity modulus E_j, interior radius r_{j-1}, and exterior radius r_j, the two general equations governing the deformation of this layer under internal p_{j-1} and external pressures p_j subject to uniform longitudinal strain ε_l, or uniform longitudinal stress σ_l, are (Halliwell, 1963; Timoshenko and Goodie, 1970):

$$u_r^j(r) = \frac{1}{E_j}\frac{r_j^2 \cdot r_{j-1}^2}{r_j^2 - r_{j-1}^2}\left[\frac{(1+\nu_j)}{r}\left(p_{j-1} - p_j\right) + (1-\nu_j)\cdot r \cdot \left(\frac{p_{j-1}}{r_j^2} - \frac{p_j}{r_{j-1}^2}\right)\right] - \frac{\nu_j \cdot \sigma_l \cdot r}{E_j}, \tag{2.2}$$

$$\varepsilon_l = \frac{\sigma_l}{E_j} - \frac{2\ \nu_j \cdot r_j^2 \cdot r_{j-1}^2}{E_j \cdot (r_j^2 - r_{j-1}^2)}\left(\frac{p_{j-1}}{r_j^2} - \frac{p_j}{r_{j-1}^2}\right), \tag{2.3}$$

In plane strain conditions ($\varepsilon_l = 0$), Eq. (2.3) becomes:

$$\sigma_l = \frac{2\ \nu_j \cdot r_j^2 \cdot r_{j-1}^2}{r_j^2 - r_{j-1}^2}\left(\frac{p_{j-1}}{r_j^2} - \frac{p_j}{r_{j-1}^2}\right), \tag{2.4}$$

In the following discussion, uncracked materials or layers are homogenous, elastic with axisymmetrical behaviour modeled according to thick-walled cylinder theory (Timoshenko and Goodie, 1970) while cracked layers cannot transfer tensile stresses (layers with radial cracks).

The displacements $u^j_r(r)$, of the different layers shown in the 2-D calculation model of Fig. 1(a), can be written as (Hachem and Schleiss, 2009):

- Steel liner

$$u_r^s(r = r_c) = \frac{1+\nu_s}{E_s}\frac{r_c}{r_c^2 - r_i^2}\left[(1-2\nu_s)\left(p_i \cdot r_i^2 - p_c \cdot r_c^2\right) + \left(p_i - p_c\right)\cdot r_i^2\right], \tag{2.5}$$

- Uncracked backfill concrete

$$u_r^c(r = r_a \text{ or } r_c) = \frac{1+\nu_c}{E_c}\frac{r}{r_a^2 - r_c^2}\left[(1-2\nu_c)\left(p_c \cdot r_c^2 - p_{r1} \cdot r_a^2\right) + \left(p_c - p_{r1}\right)\cdot r^2\right], \tag{2.6}$$

- Cracked backfill concrete

$$u_r^c(r = r_a) = u_r^c(r = r_c) + \frac{(1-\nu_c^2)\cdot p_c \cdot r_c}{E_c}\ln\left(\frac{r_c}{r_a}\right), \tag{2.7}$$

with, $p_c \cdot r_c = p_{r1} \cdot r_a$, (2.8)

- Uncracked near-field rock zone

  In this case, the entire rock mass (near- and far-field) is treated as an infinite uncracked layer ($r_f \to \infty$). The displacements u^{rm}_r at the interior face of the rock mass layer is:

$$u_r^{rm}(r = r_a) = \frac{(1+\nu_{rm})}{E_{rm}} \cdot p_{r1} \cdot r_a, \tag{2.9}$$

- Cracked near-field rock zone

$$u_r^{crm}(r = r_f) = u_r^{crm}(r = r_a) + \frac{(1-\nu_{rm}^2)\cdot p_{r1} \cdot r_a}{E_{crm}}\ln\left(\frac{r_a}{r_f}\right), \tag{2.10}$$

with, $p_{r1} \cdot r_a = p_{r2} \cdot r_f$, (2.11)

- Uncracked infinite far-field rock zone when the near-field rock is considered as cracked

$$u_r^{rm}(r = r_f) = \frac{(1+\nu_{rm})}{E_{rm}} \cdot p_{r2} \cdot r_f, \tag{2.12}$$

Note that Eq. (2.8) assuming cracked backfill concrete is derived from the theory of thick-walled cylinder by putting the tensile stress σ_t equal to zero in the general equation: $\sigma_t - \sigma_r - r\,\mathrm{d}\sigma_r / \mathrm{d}r = 0$ and then by integrating it between the two layer's borders where $\sigma_r = p_c$

at $r = r_c$ and $\sigma_r = p_{r1}$ at $r = r_a$. Variables σ_t and σ_r stand respectively for the tensile and radial stresses in the cylinder wall and $d\sigma_r / dr$ for the first derivative of σ_r relative to the radius r measured from the tunnel axis. The same procedure is used to obtain Eq. (2.11) for cracked near-field rock zone. The far-field rock zone was assumed as homogeneous, isotropic and elastic with a mean elastic deformation modulus E_{rm}.

The near field rock zone corresponds to the rock mass disturbed (loosened) as a result of the excavation method and the change in the near stress field around the tunnel. Schleiss (1988) suggested values for the disturbed rock zone between 0.5 to 1.0 m for tunnels excavated by Tunnel Boring Machine (TBM) and 1.0 to 2.0 m for drill and blast excavation. In the paper, r_f has been taken equal to 1.25 times r_a.

2.1.2. General case considering kinematic and dynamic effects of water and steel liner

Depending on the system stiffness of steel-lined pressure tunnels and penstocks, deviation from the quasi-static case may occur. Pressure waves in water produce dynamic forces on the steel liner and trigger vibrations. Such liner vibrations cause additional water pressure waves in return. This phenomenon is called "Fluid-Structure Interaction or FSI". Compared to the conventional uncoupled water hammer analyses, FSI may lead to: higher or lower extreme dynamic pressures and steel wall stresses, change in the natural frequencies of the system, and more damping and dispersion in the pressure and stress histories (Kuiken, 1988). The dispersion results from a frequency-dependent wave speed built from different frequencies travelling at different speeds. This makes it difficult to identify the exact location of the wave front.

Denoting the axial displacement of the steel liner by u_l^s, the linearized boundary conditions at the water-liner interface using the no-slip condition are:

$$\begin{cases} u = \dfrac{\partial u_l^s}{\partial t}, \\ v = \dfrac{\partial u_r^s}{\partial t}, \end{cases} \tag{2.13}$$

where, u and v are respectively the water velocities in the axial x and radial r directions and t is the time. The first boundary condition concerning the velocity u is not needed in non-viscous fluid approximation (Rubinov and Keller, 1971).

The effect of the backfill concrete and the surrounding rock mass is mechanically modeled by a spring, a dashpot, and a lumped additional mass (Kelvin model). This conceptual model is represented in Fig. 1(b). The model input coefficients are Ks_r, C_r and M_r representing respectively (per unit area) the spring stiffness coefficient, the frictional coefficient of the dashpot, and an additional mass. The same mechanical model is used to represent longitudinal liner-rock interaction with Ks_l, C_l, and M_l as coefficients.

The six-equation (3-mode) model of the FSI problem was established first by Atabek (1968) and generalized by Kuiken (1984). These equations are:

- For the fluid without body forces in the axial x and radial r directions, the linearized equations of motions (Eqs. (2.14) and (2.15)), of continuity (Eq. (2.16)) and the thermodynamic constitutive equation for the density (Eq. (2.17)) are respectively:

$$\rho_0 \frac{\partial u}{\partial t} = -\frac{\partial p}{\partial x} + \mu\left(\frac{\partial^2 u}{\partial r^2} + \frac{1}{r}\frac{\partial u}{\partial r} + \frac{\partial^2 u}{\partial x^2}\right) + \left(\kappa + \frac{1}{3}\mu\right)\left(\frac{\partial^2 v}{\partial r \partial x} + \frac{1}{r}\frac{\partial v}{\partial x} + \frac{\partial^2 u}{\partial x^2}\right), \tag{2.14}$$

$$\rho_0 \frac{\partial v}{\partial t} = -\frac{\partial p}{\partial r} + \mu\left(\frac{\partial^2 v}{\partial r^2} + \frac{1}{r}\frac{\partial v}{\partial r} + \frac{\partial^2 v}{\partial x^2} - \frac{v}{r^2}\right) + \left(\kappa + \frac{1}{3}\mu\right)\left(\frac{\partial^2 v}{\partial r^2} + \frac{1}{r}\frac{\partial v}{\partial r} - \frac{v}{r^2} + \frac{\partial^2 u}{\partial x \partial r}\right), \tag{2.15}$$

$$\frac{\partial \rho}{\partial t} + \rho_0\left(\frac{\partial v}{\partial r} + \frac{v}{r} + \frac{\partial u}{\partial x}\right) = 0, \tag{2.16}$$

$$dp = c_T^2 \cdot d\rho, \tag{2.17}$$

- For the steel liner, the equations of motion in an initially stressed field are (Flügge, 1973):

$$\rho_s \cdot t_s \frac{\partial^2 u_l^s}{\partial t^2} = \frac{\partial \sigma_l^+}{\partial x} + F_x + \sigma_l^0 \frac{\partial^2 u_l^s}{\partial x^2} - \frac{\sigma_r^0}{r_i} \frac{\partial u_r^s}{\partial x}, \tag{2.18}$$

$$\rho_s \cdot t_s \frac{\partial^2 u_r^s}{\partial t^2} = -\frac{\sigma_r^+}{r_i} + F_r + \sigma_l^0 \frac{\partial^2 u_r^s}{\partial x^2} + \frac{\sigma_r^0}{r_i} \frac{\partial u_l^s}{\partial x}, \tag{2.19}$$

where, ρ is the unit mass of water in excess of the steady-state unit mass ρ_0, p is the water pressure in excess of the steady-state pressure p_0, μ and κ are respectively the dynamic and the bulk viscosities of water, ρ_s the unit mass of steel, t_s the thickness of the liner, σ_r^+ and σ_l^+ are respectively the perturbation stresses in the circumferential and axial directions, σ_r^0 and σ_l^0 are the initial radial and longitudinal stresses in the liner evaluated per unit length, and c_T is the speed of sound in unconfined water equal to $(K_w/\rho_w)^{0.5}$, where K_w is the bulk modulus of water and ρ_w is the unit mass of water when the FSI is not considered. The forces F_x and F_r represent the resultant of hydrodynamic forces and forces applied by the surrounding backfill concrete on the liner respectively in the axial and radial directions. According to the Kelvin model, these forces are specified by:

$$F_x = -\mu \left[\frac{\partial u}{\partial r} + \frac{\partial v}{\partial r} \right]_{r=r_i} - M_l \frac{\partial^2 u_l^s}{\partial t^2} - C_l \frac{\partial u_l^s}{\partial t} - Ks_l \cdot u_l^s, \tag{2.20}$$

$$F_r = \left[p - 2\mu \frac{\partial v}{\partial r} - \left(\kappa - \frac{2}{3}\mu \right) \left(\frac{1}{r} \frac{\partial r v}{\partial r} + \frac{\partial u}{\partial x} \right) \right]_{r=r_i} - M_r \frac{\partial^2 u_r^s}{\partial t^2} - C_r \frac{\partial u_r^s}{\partial t} - Ks_r \cdot u_r^s, \tag{2.21}$$

Finally, the linear stress-strain relations for membranes are:

$$\sigma_r^+ = B \cdot \frac{u_r^s}{r_i} + B_{(12)} \cdot \frac{\partial u_l^s}{\partial x}, \tag{2.22}$$

$$\sigma_l^+ = B_{(12)} \cdot \frac{u_r^s}{r_i} + B \cdot \frac{\partial u_l^s}{\partial x}, \tag{2.23}$$

where, B and $B_{(12)}$ are defined in Eq. (2.30).

The unknowns to be solved are u, v, p, u_l^s, and u_r^s. They are assumed to vary harmonically in x and t with a real constant angular frequency ω according to the following expressions in which the superscript ^ indicate the amplitude of the periodic quantities and c denotes the complex propagation velocity:

$$[u, v, p] = [\hat{u}(r), \hat{v}(r), \hat{p}(r)] \cdot e^{i \cdot \omega \cdot (t - x/c)}, \tag{2.24}$$

$$[u_l^s, u_r^s] = [\hat{u}_l^s, \hat{u}_r^s] \cdot e^{i \cdot \omega \cdot (t - x/c)}, \tag{2.25}$$

Any non-sinusoidal variable can be treated as the combination of an infinite number of harmonic components using Fourier transformation. In linear theory, small sinusoidal amplitude motions of the liner wall are considered.

By substituting Eq. (2.24) into Eqs. (2.14)-(2.16), and using Eq. (2.17), the following expressions for $\hat{u}(r)$, $\hat{v}(r)$ and $\hat{p}(r)$ can be written:

$$\begin{cases} \hat{u}(r) = \dfrac{\Phi_1 \cdot \hat{p}_0}{\rho \cdot c_0} \cdot \left[k \cdot J_0\left(i \cdot \beta \cdot \zeta \cdot k \cdot r / r_i \right) + D \cdot F_0\left(\left(i^3 \alpha^2 - k^2 \beta^2 \right)^{0.5} \cdot \dfrac{r}{r_i} \right) \right], \\ \hat{v}(r) = \dfrac{\Phi_1 \cdot \hat{p}_0}{\rho \cdot c_0} \cdot \left[\xi \cdot k \cdot J_1\left(i \cdot \beta \cdot \zeta \cdot k \cdot r / r_i \right) + 0.5 \cdot i \ \beta \ k \cdot D \cdot F_1\left(\left(i^3 \alpha^2 - k^2 \beta^2 \right)^{0.5} \cdot \dfrac{r}{r_i} \right) \right], \\ \hat{p}(r) = \hat{p}_0 \cdot J_0\left(i \cdot \beta \cdot \zeta \cdot k \cdot r / r_i \right), \end{cases} \tag{2.26}$$

where $\hat{p}_0$ is the reference pressure amplitude of water at $r = 0$, $i = (-1)^{0.5}$, D an integration constant, and c_0 is the reference wave speed (defined in Eq. (4.2)), and the functions $F_n(\lambda \cdot r/r_i)$ are defined by:

$$F_n(\lambda \cdot r/r_i) = 2^n \cdot n! \frac{J_n(\lambda \cdot r/r_i)}{\lambda^n . J_0(\lambda)}, \tag{2.27}$$

where, $J_0(y)$ and $J_1(y)$ are respectively the zero and first order first-kind Bessel functions. In Eq. (2.26), the various dimensionless parameters are:

$$\begin{cases} k=\dfrac{c_0}{c}, \quad \alpha=r_i\cdot\left(\dfrac{\omega\cdot\rho_0}{\mu}\right)^{0.5}, \quad \alpha'=\alpha\cdot\left(\dfrac{\omega\cdot\rho_0}{\kappa}\right)^{0.5}, \quad \beta=\dfrac{\omega\cdot r_i}{c_0}, \quad \beta'=\dfrac{\omega\cdot r_i}{c_T}, \\ \beta_{0T}=\dfrac{c_0}{c_T}, \quad \zeta^2=1-\dfrac{\beta_{0T}^2}{k^2\cdot\Phi_1}, \quad \Phi_1=1+\dfrac{i\cdot\beta'^2}{\alpha'^2}+\dfrac{4\cdot i\cdot\beta'^2}{3\alpha^2}, \end{cases} \tag{2.28}$$

The first two homogeneous equations needed to solve the problem are derived from the substitution of Eqs. (2.26) into Eqs. (2.20) and (2.21). These latter equations with Eqs. (2.22) and (2.23) are then injected into Eqs. (2.18) and (2.19). The other two equations are derived from the substitution of Eqs. (2.25) and (2.26) into the kinematic boundary condition (2.13). A non-trivial solution for the five unknowns plus the constant of integration D is possible if the determinant is equal to zero. The following dispersion equation for an isotropic and elastic steel liner is thus obtained:

$$\begin{aligned} &k^6\cdot\left(\zeta^2\cdot F_{1\beta}(1)-F_{1\alpha}(1)\right)\cdot\beta^2\cdot B'_{22}\cdot\sigma'^0_l \\ &+k^4\cdot\left[\left(\zeta^2\cdot F_{1\beta}(1)-F_{1\alpha}(1)\right)\left(B'_{22}\cdot B^0_{11}-B^{0\,2}_{12}+K'_l\cdot\sigma'^0_l\right)-0.5\cdot\zeta^2\cdot F_{1\beta}(1)\cdot F_{1\alpha}(1)\cdot\beta^2\cdot\sigma'^0_l\right] \\ &+k^2\cdot\left[F_{1\alpha}(1)\cdot\left(B^0_{12}+\Phi_4\cdot B^0_{21}-0.5\cdot B^0_{11}\cdot\zeta^2\cdot F_{1\beta}(1)\right)-2\cdot\Phi_4\cdot B'_{22}+\left(K'_l/\beta^2\right)\cdot B^0_{11}\cdot\left(\zeta^2\cdot F_{1\beta}(1)-F_{1\alpha}(1)\right)\right] \\ &+\Phi_4\cdot\left[F_{1\alpha}(1)-2\cdot\left(K'_l/\beta^2\right)\right]=0, \end{aligned} \tag{2.29}$$

where,

$$\begin{cases} B'_{22}=\dfrac{B+\sigma^0_l}{\rho\cdot r_i\cdot c_0^2}, \quad B=\dfrac{E_s\cdot t_s}{\left(1-\nu_s^2\right)}, \quad \sigma'^0_l=\dfrac{\sigma^0_l}{\rho\cdot r_i\cdot c_0^2}, \\ B^0_{11}=B'_{11}+K'_r-\dfrac{2\cdot i\cdot\beta^2}{\alpha}, \quad B'_{11}=\dfrac{B}{\rho\cdot r_i\cdot c_0^2}, \\ K'_{r,l}=\dfrac{r_i}{\rho\cdot c_0^2}\cdot\left[Ks_{r,l}+i\cdot\omega\cdot C_{r,l}-\omega^2\left(M_{r,l}+\rho_s\cdot t_s\right)\right], \quad B^0_{21}=B^0_{12}=B'_{12}-\dfrac{2\cdot i\cdot\beta^2}{\alpha^2}, \\ B'_{12}=\dfrac{B_{(12)}-\sigma^0_r}{\rho\cdot r_i\cdot c_0^2}, \quad B_{(12)}=\dfrac{E_s\cdot t_s\cdot\nu_s}{\left(1-\nu_s^2\right)}, \quad \Phi_4=\dfrac{\Phi_2+\dfrac{2\cdot i\cdot\beta'^2}{\alpha^2}}{\Phi_1}, \quad \Phi_2=1-\dfrac{i\cdot\beta'^2}{\alpha'^2}+\dfrac{2\cdot i\cdot\beta'^2}{3\alpha^2}, \end{cases} \tag{2.30}$$

and $F_{1\alpha}\left(\dfrac{r}{r_i}\right)$ and $F_{1\beta}\left(\dfrac{r}{r_i}\right)$ stand respectively for the first members of:

$$\begin{cases} F_{n\alpha}\left(\dfrac{r}{r_i}\right)\equiv F_n\left(\left(i^3\alpha^2-k^2\beta^2\right)^{0.5}\cdot\dfrac{r}{r_i}\right) \quad ;n=0,1 \\ F_{n\beta}\left(\dfrac{r}{r_i}\right)\equiv F_n\left(i\cdot\beta\cdot\zeta\cdot k\cdot\dfrac{r}{r_i}\right) \quad ;n=0,1 \end{cases} \tag{2.31}$$

The complete solution is finally obtained for a linear combination of the forward and backward propagation mode for infinitely long tunnels and shafts. Using Eqs. (2.26), the linear combination of the solution (2.24) for each mode gives:

$$\begin{cases} u(r) = \dfrac{\Phi_1 \cdot \hat{p}(r_i)}{\rho \cdot c_0} \cdot k \cdot \left[F_{0\beta}\left(\dfrac{r}{r_i}\right) + D' \cdot F_{0\alpha}\left(\dfrac{r}{r_i}\right) \right] \cdot \left[D_1 \cdot \cos\left(\dfrac{\omega \cdot x}{c}\right) + D_2 \cdot \sin\left(\dfrac{\omega \cdot x}{c}\right) \right] \cdot e^{i\omega t}, \\ v(r) = \dfrac{\Phi_1 \cdot \hat{p}(r_i)}{\rho \cdot c_0} \cdot 0.5 \cdot \beta \cdot k^2 \cdot \left[\zeta^2 \cdot F_{1\beta}\left(\dfrac{r}{r_i}\right) - D' \cdot F_{1\alpha}\left(\dfrac{r}{r_i}\right) \right] \cdot \left[-D_1 \cdot \sin\left(\dfrac{\omega \cdot x}{c}\right) + D_2 \cdot \cos\left(\dfrac{\omega \cdot x}{c}\right) \right] \cdot e^{i\omega t}, \\ p(r) = \hat{p}(r_i) \cdot F_{0\beta}\left(\dfrac{r}{r_i}\right) \cdot \left[-D_1 \cdot \sin\left(\dfrac{\omega \cdot x}{c}\right) + D_2 \cdot \cos\left(\dfrac{\omega \cdot x}{c}\right) \right] \cdot e^{i\omega t}, \end{cases} \tag{2.32}$$

where, the complex constants D_1 and D_2 are determined, for each mode, by boundary conditions at two different sections of the steel lined tunnel, and the mode-dependent factor D' is defined by:

$$D' = -\frac{D}{k \cdot j_0\left(i\ \beta\ \zeta\ k\right)} = \frac{\left[\left(B_{11}^0 + k^2 \cdot \beta^2 \cdot \sigma_l'^0 \right) \cdot \zeta^2 \cdot F_{1\beta} - 2 \cdot B_{12}^0 \right] \cdot \mathrm{k}^2 - 2 \cdot \Phi_4}{\left[\left(B_{11}^0 + k^2 \cdot \beta^2 \cdot \sigma_l'^0 \right) \cdot F_{1\alpha} - 2 \cdot B_{12}^0 \right] \cdot \mathrm{k}^2}, \tag{2.33}$$

The radial and longitudinal displacements of the steel liner or penstock wall result from the summation of the mode solutions. For each mode, the solution is:

$$\begin{cases} u_r^s(x,t) = 0.5 \cdot r_i \cdot k^2 \cdot \left(\zeta^2 \cdot F_{1\beta}(1) - D' \cdot F_{1\alpha}(1) \right) \left(\dfrac{\Phi_1 \cdot p(r_i)}{\rho \cdot c_0^2} \right), \\ u_l^s(x,t) = -i \cdot r_i \cdot \dfrac{k}{\beta} \cdot \left(1 - D'\right) \left(\dfrac{\Phi_1 \cdot p(r_i)}{\rho \cdot c_0^2} \right), \end{cases} \tag{2.34}$$

3. Water-hammer-wave speed expressions without Fluid-Structure Interaction

The classical theory of water hammer predicts pressure wave propagation inside a frictionless closed cylinder with uniform cross section at a wave speed given by the following general formula (Wylie et al., 1993):

$$a = \sqrt{\frac{1}{\rho_w \left(\dfrac{1}{K_w} + \dfrac{1}{A} \cdot \dfrac{\mathrm{d}A}{\mathrm{d}p_i} \right)}}, \tag{3.1}$$

where, dA is the variation of the cross-sectional area A of the cylinder caused by the variation of the internal water pressure dp_i.

For multiphase (vapor cavities are present) and multicomponent (suspended sediment is present) flow, the bulk modulus K_w and the unit mass ρ_w are substituted in Eq. (3.1) with an effective bulk modulus K_e and an effective unit mass ρ_e (Wylie et al., 1993).

Without considering the FSI and by ignoring the dynamic effect of the tunnel wall, dA/dp_i is a constant value. This results in a constant, or quasi-static, wave speed.

In plain strain conditions and considering the hypothesis of linear elasticity and small deformations with $r_i \approx r_c$ (thin-walled liners are considered), Eq. (3.1) can be written, according to Fig. 1(a), as follows:

$$a = \sqrt{\frac{1}{\rho_w \left(\dfrac{1}{K_w} + \dfrac{2}{r_i} \cdot \dfrac{\mathrm{d}u_r^s(r_i)}{\mathrm{d}p_i} \right)}}, \tag{3.2}$$

in which $\dfrac{\mathrm{d}u_r^s(r_i)}{\mathrm{d}p_i}$ is the first derivative of u_r^s relative to the internal pressure p_i at the layer interface of radius r_i.

3.1. *Case 1: Backfill concrete and near-rock mass zone are uncracked*

For this case, the transmitted load to the rock is first determined as a function of p_i, Δr_0, and the materials characteristics by solving the system of the compatibility of deformation (2.1) using Eqs. (2.5), (2.6) and (2.9). The radial deformation of the steel liner, $u_r^s(r_c)$ and its derivative according to p_i are then computed from Eq. (2.5).

The complete expression of water-hammer-wave speed is obtained by replacing the following expression of $\frac{\mathrm{d}u_r^s(r_c)}{\mathrm{d}p_i}$ in Eq. (3.2).

$$\begin{cases} \dfrac{\mathrm{d}u_r^s(r_c)}{\mathrm{d}p_i} = \dfrac{2(1+\nu_c)(1-\nu_s^2)\cdot r_c\cdot r_i^2\cdot\left[E_c\cdot(1+\nu_{rm})\left((1-2\nu_c)\cdot r_c^2+r_a^2\right)-E_{rm}\cdot(1+\nu_c)(1-2\nu_c)\left(r_c^2-r_a^2\right)\right]}{A_1+A_2}, \\ \text{where ;} \\ A_1 = E_s\cdot\left(r_c^2-r_i^2\right)\left(E_{rm}\cdot(1+\nu_s)^2(2\nu_c-1)\left(r_c^2-r_a^2\right)-E_c\cdot(1+\nu_c)(1+\nu_{rm})\left((2\nu_c-1)\cdot r_c^2-r_i^2\right)\right), \\ A_2 = E_c\cdot(1+\nu_s)\left((2\nu_s-1)\cdot r_c^2-r_i^2\right)\left((1+\nu_{rm})\left(r_c^2-r_a^2\right)-E_{rm}\cdot(1+\nu_c)\left(r_c^2-(2\nu_c-1)\cdot r_a^2\right)\right), \end{cases} \tag{3.3}$$

3.2. *Case 2: Backfill concrete is cracked while rock mass is not*

Eqs (2.5), (2.7), (2.8) and (2.9) are used to solve the system of Eqs (2.1) for p_c , p_{r1} and $u_r^s(r_c)$. The following expression of $\frac{\mathrm{d}u_r^s(r_c)}{\mathrm{d}p_i}$ is then replaced in Eq. (3.2).

$$\begin{cases} \dfrac{\mathrm{d}u_r^s(r_c)}{\mathrm{d}p_i} = \dfrac{2\left(\nu_s^2-1\right)\cdot r_c\cdot r_i^2\cdot\left[E_c\cdot(1+\nu_{rm})-\left(1-\nu_c^2\right)\cdot E_{rm}\cdot\ln\left(\dfrac{r_c}{r_a}\right)\right]}{A_3+A_4}, \\ \text{where ;} \\ A_3 = E_c\cdot\left[E_{rm}\cdot(1+\nu_s)\cdot\left((2\nu_s-1)\cdot r_c^2-r_i^2\right)-E_s\cdot(1+\nu_{rm})\cdot\left(r_c^2-r_i^2\right)\right], \\ A_4 = \left(1-\nu_c^2\right)\cdot E_{rm}\cdot E_s\cdot\left(r_c^2-r_i^2\right)\cdot\ln\left(\dfrac{r_c}{r_a}\right), \end{cases} \tag{3.4}$$

3.3. *Case 3: Backfill concrete and near-rock zone are cracked*

For this case, the expression of $\frac{\mathrm{d}u_r^s(r_c)}{\mathrm{d}p_i}$ is obtained by replacing E_c by $(E_c\ E_{crm})$ and $(1-\nu^2_c)\cdot\ln(r_c/r_a)$ by $[(1-\nu^2_c)\cdot E_{crm}\cdot\ln(r_c/r_a)+(1-\nu^2_{rm})\cdot E_c\cdot\ln(r_a/r_c)]$ in Eq. (3.4). This yields to the following expression for $\frac{\mathrm{d}u_r^s(r_c)}{\mathrm{d}p_i}$:

$$\begin{cases} \dfrac{du_r^s(r_c)}{dp_i} = \dfrac{2\left(\nu_s^2 - 1\right)\cdot r_c \cdot r_i^2 \left[E_c \cdot E_{crm}\left(1+\nu_{\mathrm{rm}}\right) - E_{\mathrm{rm}}\left(\left(1-\nu_c^2\right)\cdot E_{\mathrm{crm}} \cdot \ln\left(\dfrac{r_c}{r_a}\right) + \left(1-\nu_{rm}^2\right)\cdot E_{\mathrm{c}} \cdot \ln\left(\dfrac{r_a}{r_f}\right)\right)\right]}{A_5 + A_6}, \\ \text{where ;} \\ A_5 = E_c \cdot E_{crm} \cdot \left[E_{\mathrm{rm}} \cdot \left(1+\nu_s\right)\cdot\left(\left(2\nu_s - 1\right)\cdot r_c^2 - r_i^2\right) - E_s \cdot \left(1+\nu_{\mathrm{rm}}\right)\cdot\left(r_c^2 - r_i^2\right)\right], \\ A_6 = E_{\mathrm{rm}} \cdot E_s \cdot \left(r_c^2 - r_i^2\right)\left(\left(1-\nu_c^2\right)\cdot E_{\mathrm{crm}} \cdot \ln\left(\dfrac{r_c}{r_a}\right) + \left(1-\nu_{rm}^2\right)\cdot E_{\mathrm{c}} \cdot \ln\left(\dfrac{r_a}{r_f}\right)\right), \end{cases} \tag{3.5}$$

This case of the calculation scheme can be considered as the most realistic case. In fact, the backfill concrete with low tensile strength is normally cracked, and the close rock field is disturbed and cracked as a result of excavation and the change in the stress field around the tunnel. Only radial compressive stresses can be transmitted in these cracked zones. The water-wave-velocity expression for this case is referred in this paper as the "complete quasi-static expression" which is valid for wave-speed calculation in frictionless circular steel-lined tunnel with axisymmetrical behaviour. The complete quasi-static expression neglects the Fluid-Structure Interaction.

3.4. Comparison of calculated wave speeds for Cases 1, 2, and 3

For comparison of Cases 1, 2 and 3, three configurations with different elasticity modulus for the far-field rock zone (E_{rm} = 5, 10 and 20% of E_s) were analyzed by using the following input values:

E_s = 210'000 MPa ; E_c = 21'000 MPa ; $E_{\mathrm{crm}} = 0.5 \cdot E_{\mathrm{rm}}$

ν_s = 0.30 ; ν_c = 0.20 ; ν_{rm} = 0.25

$r_a = 1.2 \cdot r_i$; $r_f = 1.25 \cdot r_a$; K_w =2'200 MPa ; ρ_w =1'000 kg/m^3

In Fig. 2, the quasi-static wave speeds for the three cases are given. The relative differences of Cases 1 and 2 compared to Case 3 are indicated as a function of (r_i/t_s) for the three (E_{rm}/E_s) ratios. If the near-rock mass zone is considered as uncracked with cracked backfill concrete (Case 2), it can be seen that the wave speed is higher, compared to the cracked layers case (Case 3). This augmentation of wave speed is 1 to 1.5% for thick steel liners and 1.5 to 4% for thin steel liners. If the backfill concrete and the near-rock field are both considered as uncracked (Case 1), the overestimation of the wave speed, compared to Case 3, is between 2 and 8% for thin steel liners. For thick liners, the overestimation is between 1 and 2.5%. The highest differences in the computed values of the wave speed are observed for relatively weak rock-mass moduli.

3.5. Comparison with other simplified expressions

3.5.1. Jaeger's formula

Jaeger (1972, 1977) published the following formula to estimate the pressure wave velocity in steel-lined pressure tunnels:

$$a = \sqrt{\frac{1}{\rho_w\left(\dfrac{1}{K_w} + \dfrac{2\cdot r_c \cdot (1-\lambda_1)}{E_s \cdot (r_c - r_i)}\right)}}, \tag{3.6}$$

where,

$$\lambda_1 = \frac{\dfrac{r_c^2}{E_s \cdot t_s}}{\dfrac{r_c^2}{E_s \cdot t_s} + \dfrac{r_a^2 - r_c^2}{2 \cdot E_c \cdot r_a} + \dfrac{\nu_{\mathrm{rm}} \cdot (1 + 1/\nu_{\mathrm{rm}}) \cdot r_c}{E_{\mathrm{rm}}}}, \tag{3.7}$$

This formula was derived from the same hypothesis as Case 2 model. The steel liner is treated as a thin circular cylinder and the mean radial deformation of the backfill concrete is taken into account. However, the steel and concrete Poisson's ratios are ignored.

The quasi-static wave speeds calculated according to Jaeger's formula for different (E_{rm}/E_s) ratios and their relative differences compared to Case 3 are shown on Fig. 3(a). Jaeger's relation overestimates the water hammer velocity relative to the complete quasi-static expression. The maximum relative difference reaches 3.5% for $r_i/t_s \approx 130$ and $E_{rm}/E_s = 0.05$.

3.5.2. *Parmakian's formula*

Parmakian (1963) proposed a formula considering a steel liner surrounded by uncracked and infinite rock mass. The influence of the backfill concrete and the steel Poisson's ratio are ignored. The same relation has also been used by Chaudhry (1987). It is given as follows:

$$a = \sqrt{\frac{1}{\rho_w \cdot \left(\frac{1}{K_w} + \frac{2 \cdot r_i \cdot (1+\nu_{rm})}{E_{rm} \cdot r_i + E_s \cdot t_s \cdot (1+\nu_{rm})} \right)}}, \tag{3.8}$$

Fig. 3(b) shows that the wave speed values computed by Parmakian's relation are higher than values obtained from the complete quasi-static expression. For $E_{rm}/E_s = 0.05$, the wave speed is overestimated by 3 to 4.6% for $r_i/t_s \approx 150$.

3.5.3. *Halliwell's formula*

Halliwell (1963) derived a formula for the wave speed assuming an uncracked concrete and rock mass surrounding the steel liner. The same Poisson's ratios for steel, concrete and rock are considered. Salah et al. (2001) generalized Halliwell's formula using different Poisson's ratios for each material.

Halliwell's wave speed equation is written as follows:

$$a = \sqrt{\frac{1}{\rho_w \cdot \left(\frac{1}{K_w} + \frac{2 \cdot r_c \cdot (1-\nu^2) \cdot (1-\lambda_2)}{E_s \cdot (r_c - r_i)} \right)}}, \tag{3.9}$$

where, $$\lambda_2 = \frac{(1-\nu) \cdot r_c}{(1-\nu) \cdot r_c + \frac{E_s \cdot (r_c - r_i)}{E_c} \cdot \frac{E_c \cdot \left(r_a^2 + r_c^2 \cdot (1-2\nu)\right) + E_{rm} \cdot (1-2\nu) \cdot \left(r_a^2 - r_c^2\right)}{E_c \cdot \left(r_a^2 - r_c^2\right) + E_{rm} \cdot \left(r_c^2 + r_a^2 \cdot (1-2\nu)\right)}}, \tag{3.10}$$

and, $\nu_s = \nu_c = \nu_{rm} = \nu$.

The wave speed and relative differences computed from Halliwell's formula are shown on Fig. 3(c). This formula gives wave speed values of approximately 7.5% higher than the complete quasi-static expression for $r_i/t_s = 150$ and $E_{rm}/E_s = 0.05$ assuming $\nu = 0.3$.

3.5.4. *Special case of open-air penstocks and unlined pressure tunnels*

Open-air penstocks

The pressure wave speed relation for a longitudinally blocked penstock can be derived from Eq. (3.3) of Case 1 by putting $r_a = r_c$ and by replacing ν_c, ν_{rm}, E_c and E_{rm} by zeros and (r_c+r_i) by $2r_i$. Considering the longitudinal boundary conditions of the penstock, Halliwell (1963) generalized the formula and Streeter (1963) corrected it in the case of penstocks that can freely slip in the longitudinal direction as follows:

$$a = \sqrt{\frac{1}{\rho_w \cdot \left(\frac{1}{K_w} + \frac{2 \cdot r_i \cdot \lambda_3}{E_s \cdot t_s} \right)}}, \tag{3.11}$$

where, $\lambda_3 = \begin{cases} 1 - 0.5 \cdot \nu_s & \text{if the penstock can freely slip in the longitudinal direction,} \\ 1 & \text{if the penstock has expansion joints over its entire length,} \\ 1 - \nu_s^2 & \text{if the penstock is blocked in the longitudinal direction.} \end{cases}$

Unlined pressure tunnels

The wave speed in an unlined pressure tunnel can be deduced from Case 1 by putting $r_a = r_c = r_i$ and by setting ν_s, ν_c, E_s and E_c equal to zero. Then, the wave speed can be written as:

$$a = \sqrt{\frac{1}{\rho_w \cdot \left(\frac{1}{K_w} + \frac{2 \cdot (1 + \nu_{rm})}{E_{rm}} \right)}}, \tag{3.12}$$

The same relation has been proposed by Parmakian (1963) while in Jaeger (1977), ν_{rm} has also been set equal to zero. Jaeger's approximation leads to a wave speed overestimation of 3.5% for E_{rm}= 10'000 MPa and ν_{rm}= 0.25.

3.6. *Definition of an apparent rock mass modulus*

The purpose of the definition of such apparent rock mass modulus is to simplify the complicated expression of the quasi-static wave speed of the complete quasi-static expression (Case 3). The backfill concrete and the near- and far-rock masses are replaced by an equivalent homogeneous rock mass with an apparent elasticity modulus, E_{app} .This latter is defined such that the transmitting load ratio from steel to the equivalent rock mass is the same as in Case 3. The apparent rock mass modulus can be obtained by equating the wave velocity expressions in Cases 1 or 2 (with $r_a \rightarrow r_c$ and E_{rm} replaced by E_{app}) with wave velocity in Case 3 (with $r_a \rightarrow r_c$):

$$a\ (\textit{Case 1 or 2}) = a\ (\textit{Case 3}), \tag{3.13}$$

Eq. (3.13) leads to two expressions defining respectively E_{app} and a as follows:

$$E_{app} = \frac{E_{rm} \cdot E_{crm}}{E_{crm} - E_{rm} \cdot (1 - \nu_{rm}) \cdot \ln\left(\frac{r_c}{r_f} \right)}, \tag{3.14}$$

$$a = \sqrt{\frac{1}{\rho_W \left[\frac{1}{K_W} + \frac{4 \cdot (\nu_s^2 - 1)(1 + \nu_{rm}) \cdot r_c \cdot r_i}{E_{app} \cdot (1 + \nu_s) \left[(2\nu_s - 1) \cdot r_c^2 - r_i^2 \right] - E_s \cdot (1 + \nu_{rm})(r_c^2 - r_i^2)} \right]}}, \tag{3.15}$$

4. Water-hammer-wave speed expressions considering the Fluid-Structure Interaction

By considering the water as a compressible non-viscous fluid (μ=κ=0) and by neglecting the initial longitudinal stress in the steel liner (σ^0=0), the dispersion Eq. (2.29) can be simplified as follows:

$$\begin{aligned} &\left[\left(B'_{22} + K'_r \right) \cdot K'_l + k^2 \cdot \beta^2 \left(B'^2_{22} + B'_{22} \cdot K'_r - B'^2_{12} \right) \right] \cdot \left(k^2 \cdot \beta^2 - \beta'^2 \right) \cdot F_1 \left(i \cdot \left(k^2 \cdot \beta^2 - \beta'^2 \right)^{0.5} \right) \\ &= 2 \cdot \beta^2 \left(K'_l + k^2 \cdot B'_{22} \cdot \beta^2 \right), \end{aligned} \tag{4.1}$$

The reference velocity a_0 can be written, according to Kuiken (1984), as:

$$c_0 = \sqrt{\frac{1}{\rho_w\left(\frac{1}{K_w} + C\cdot\frac{2\cdot r_i}{E_s\cdot t_s}\right)}}, \tag{4.2}$$

where

$$C = \frac{1-\nu_s^2}{1+\frac{K_r}{B}}, \tag{4.3}$$

and

$$K_r = r_i^2\cdot\left[Ks_r + i\cdot\omega\cdot C_r - \omega^2\left(M_r + \rho_s\cdot t_s\right)\right], \tag{4.4}$$

ω is the real angular frequency (=2πf) of the continuous excitation of frequency f.

If Ks_r is taken equal to ($p_c/u_r^s(r_c)$), calculated according to Case 3, and if ω is very small, c_0 is equal to the complete quasi-static wave speed. When ω approaches infinity, c_0 becomes the speed of sound in unconfined water $(K_w/\rho_w)^{0.5}$.

The solutions of the quadratic dispersion Eq. (4.1) occur in pairs ($\pm k$) where each $\pm k$ solution is associated to a particular mode of oscillation with waves propagating in positive and negative directions along x. The modes with small values of the imaginary part of k are the propagating modes, whereas the modes with high values of the imaginary part of k decay rapidly according to the following expression:

$$[u, v, p] = [\hat{u}(r), \hat{v}(r), \hat{p}_i(r)]\cdot e^{i\cdot\omega\cdot(t-x/c)} = [\hat{u}(r), \hat{v}(r), \hat{p}_i(r)]\cdot e^{-\Delta_i\cdot x/\lambda_i}\cdot e^{i\cdot\omega\cdot(t-x/c_i)}, \tag{4.5}$$

λ_i is the wave length of the i-th wave mode, c_i is the phase velocity, c_{pi} or the group velocity, c_{gi}, and Δ_i the logarithmic decrement of the i-th wave mode. The phase velocity of a travelling wave form may or may not correspond to a particular physical entity and does not necessarily correspond to the speed at which energy or information is propagating. That's why the phase velocity might go to infinity and be higher than the speed of sound in unconfined water. Hence, the energy of the wave propagates with the group velocity when this later is smaller than the phase velocity. The parameters of Eq. (4.5) with the equivalent reference wave speed are defined by:

$$\begin{cases} \lambda_i = 2\cdot\pi\cdot\dfrac{c_i}{\omega}, \\ \text{Phase velocity,}\quad c_{pi} = \dfrac{1}{\mathrm{Re}\left[k/c_0\right]}, \\ \text{Group velocity,}\quad c_{gi} = \dfrac{\mathrm{d}\omega}{\mathrm{d}\left(\omega\cdot\mathrm{Re}\left[k/c_0\right]\right)}, \\ \Delta_i = -2\cdot\pi\cdot\dfrac{\mathrm{Im}\left[k/c_0\right]}{\mathrm{Re}\left[k/c_0\right]}, \\ c_{0eq} = \dfrac{\mathrm{Re}[c_0]^2 + \mathrm{Im}[c_0]^2}{\mathrm{Re}[c_0]}, \end{cases} \tag{4.6}$$

where, Re[ ] and Im[ ] are respectively the real and imaginary parts of the complex numbers.

Rubinov and Keller (1971, 1978) showed that, for the non-viscous fluid approximation, two modes (called tube modes) can only propagate at low frequencies (with or without cut-off bands) and an infinite number of acoustic modes propagate at high frequencies. For open-air penstocks, the first acoustic mode begins to propagate at an angular frequency of ($\beta_{01}.c_f/r_i$), where β_{01} is the first positive root of the Bessel function J_0 (=2.40483). For example, the lower cut-off frequency of the first acoustic mode of a penstock of radius r_i =1.75 m is equal to 2'038.25 rd/s (or 324.4 Hz).

In the low-frequency range solution of Eq. (4.1), the tube mode with the lowest propagation velocity at low frequencies is the longitudinal compression mode in water (called water hammer or Young mode) while the higher propagation velocity corresponds to the axial stress wave mode in the steel walls of liners and penstocks (called precursor or Lamb mode). The axial stress waves result from the coupling of the radial expansion and contraction of the liner or penstock walls and the Poisson's ratio of the steel. The stress waves in return generate pressure fluctuations in the enclosed water. This coupling is known as the "Poisson coupling" (Skalak, 1956). Tijsseling et al. (2008) re-calculated the solution of Skalak's four-equation model and gave an analytical expression for water hammer and precursor quasi-static wave speeds in open-air penstocks. The general solution of the Poisson coupling problem has been solved exactly by Li et al. (2003) and by Tijsseling (2003).

Tijsseling (1996) has classified the one-dimensional FSI models according to their basic equations and physical variables involved to derive their dispersion equations. According to this classification and by ignoring the radial movement of water, the Kuiken model can be considered as a six-equation model (3-mode solutions) where the unknown variables are: the pressure and axial velocity of water, axial stress, axial velocity, hoop stress and radial velocity in the steel liner or penstock wall.

The wave speed results of the two tube modes (water-hammer and precursor modes) and the first acoustic mode, evaluated according to Eqs. (4.1) & (4.6), are shown in Fig. 4 for steel-lined pressure tunnels with the following parameters: r_i =1.75 m, b=100, ρ_s=7'850 kg/m^3, $\rho=\rho_0=\rho_w$=1'000 kg/m^3, E_s=210'000 MPa, f_y=580 MPa, ρ_r=2'200 kg/m^3, $E_c=E_{rm}$=21'000 MPa, E_{crm}=10'500 MPa, ζ=10%, $\mu=\kappa$=0, σ_l^0=0, and σ_r^0=0.5$\cdot f_y \cdot t_s$. It can be seen (Fig. 5(b)) that the motion of the liner wall is primarily radial for the water hammer mode and primarily longitudinal for the precursor mode. The logarithmic decrement coefficients plotted versus ω are shown in Fig. 5(a). The radial and longitudinal mechanical coefficients of the surrounding rock mass are taken as follows:

$$\begin{cases} M_r = M_l = \rho_r \cdot \left(r_f - r_c\right), \\ Ks_r = Ks_l = \dfrac{p_c}{u_r^s(r=r_c)} \ \textit{of the Case 3}, \\ C_r = C_l = 2 \cdot \zeta \cdot M_r \cdot \sqrt{Ks_r / M_r}, \end{cases} \tag{4.7}$$

where, ζ is the damping ratio of the mechanical model, ρ_r the unit mass of the rock mass, and where the inactive rock zone is considered at radius $r=r_f$.

For the water hammer mode, the group velocity is below the phase velocity for all ω values except in the narrow frequency band 1'700 - 1'900 rd/s. The group velocity represents then the wave speed of the propagating energy and can be compared to quasi-static wave speed, a, and to the speed of sound in unconfined water, c_T. For frequencies lower than 800 rd/s, the relative difference, $(c_{g1}-c_{0eq})/c_{g1}$, between the group velocity, c_{g1} and a is less than 5%. This difference increases considerably and reaches 150% for ω=1'700 rd/s. A cut-off frequency band exists around 2'000 rd/s. The water hammer mode starts to propagate again in the high-frequency range (higher than 2'250 rd/s) with a group velocity that goes up from 500 m/s to reach asymptotically c_T. Near 1'700 rd/s, the maximum attenuation coefficient is reached.

For the precursor mode, the low cut-off frequency is around 1'600 rd/s and the wave speed (equal to the group velocity) decreases rapidly when ω increases in the intermediate frequency range (between 1'600 and 2'000 rd/s) and reaches, for large ω, a rather constant value between the quasi-static and c_T wave speeds. Fig. 6(a) shows the variation of the precursor wave speed mode (phase and group velocities) as a function of ω for C_l=0 and Ks_l=0.001$\cdot Ks_r$, 0.1$\cdot Ks_r$ and Ks_r. The cut-off frequency depends on the longitudinal stiffness constraint of the liner and can be used as an indicator to detect the presence and intensity of such constraint.

The first acoustic mode begins to propagate at an angular frequency near 3'300 rd/s. This frequency is 1.7 times higher than in open-air penstocks. This cut-off frequency

depends on the radial constraint of the steel liner (Fig. 6(b)) and varies close to the second mode of rigid tubes ($\beta_{11}.c_T/r_i$=3'247.6 rd/s). β_{11} is the first positive root of the Bessel function (J_1) (β_{11}=3.83171). The phase and group velocities of this mode approach c_T when ω becomes very high.

4.1. *FSI problem in the case of open-air penstocks*

For open-air penstocks (K_r=0), Eq. (4.2) becomes equal to (3.10) when λ_3 is equal to ($1-\nu_s^2$). The solutions of Eq. (4.1) for the two tube modes and the first acoustic mode are given in Fig. 7. The water hammer mode has a cut-off frequency equal to $1/r_i \cdot (E_s/\rho_s)^{0.5}$. The precursor mode propagates for all values of ω and is very well estimated by Skalak's formula for frequencies lower than 1'200 rd/s and higher than 7'500 rd/s. In the intermediate frequency range the maximum relative difference, $(c_{g2} - a_{Skalak})/c_{g2}$, can reach 20%. The first acoustic mode presents a lower cut-off frequency equal to 2'038.25 rd/s ($=\beta_{01}.c_T/r_i$).

The classical expression (3.10) of the quasi-static wave speed has been also modified by Stuckenbruck et al. (1985). Stuckenbruck ignores radial inertia and considers only the axial inertial forces in the pipe wall. This approach leads to a constant real wave velocity and causes a reduction of the classical wave speed of about 7% for high values of $(2r_i/t_s)$.

For thin-walled viscoelastic pipes, a complex-valued and frequency-dependent wave speed has been formulated by Suo and Wylie (1990b). The classical expression (3.10) was extended by replacing E_s by a complex frequency-dependent Young's modulus, $E_s(w)$, of the viscoelastic material.

4.2. *FSI problem in the case of unlined pressure tunnels*

As can be seen from Eq. (2.30), the properties of the surrounding materials are included in K'_r and K'_l expressions. For unlined pressure tunnels in rigid rock mass, K'_r and K'_l goes to infinity (similar to a strongly constrained liner) resulting in the rigid dispersion approximation written as follows:

$$\left(\beta^2 \cdot k^2 - \beta'^2/\Phi_1\right) \cdot F_1\left(i \cdot \left(\beta^2 \cdot k^2 - \beta'^2/\Phi_1\right)^{0.5} \cdot 1\right) - \beta^2 \cdot k^2 \cdot F_1\left(i \cdot \left(\beta^2 \cdot k^2 - i^3 \cdot \alpha^2\right)^{0.5} \cdot 1\right) = 0, \tag{4.8}$$

In this case, the propagation modes are only acoustic and occur because the fluid is compressible. The roots of Eq. (4.8) are:

$$c_j = \omega \cdot r_i \cdot \left(\left(\omega \cdot r_i/c_T\right)^2 - \beta_{1j}^2\right)^{-0.5} \quad j = 0,1,2,... \tag{4.9}$$

where β_{1j} is the j-th positive root of the Bessel function (J_1). The reference velocity c_0 given in (4.2) becomes equal to the wave speed c_T which is the first root (j=0) of Eq. (4.9).

The hydraulic transients in unlined pressure tunnels have been studied by Fanelli (1973) and Suo and Wylie (1990a) without considering the complete FSI problem. The rock mass has been treated as an infinite homogeneous and isotropic cylinder and only the dynamic effect of the rock mass has been taken into account. This leads to a complex-valued and frequency-dependent wave speed. Fig. 8(a) and Fig. 8(b) show respectively the variation of the equivalent wave speed and the logarithmic decrement coefficient (Eq (4.6)) versus the radial frequency in an unlined pressure tunnel with the following input parameters: r_i =1.75m, ρ_r =2'200 kg/m^3 and E_{rm}=7'000, 10'000, 15'000 and 21'000 MPa. The equivalent wave speeds are bounded between the quasi-static (Eq. (3.12)) and the c_T wave speeds and have no cut-off frequencies. They decrease slightly at low frequencies, increase rapidly when ω increases with abrupt change of value at intermediate frequencies, and approach asymptotically c_T when the frequency goes to infinity. The decrement coefficient increases rapidly for ω between 50 and 100 rd/s and reaches its maximum value for ω around 300 and 400 rd/s for hard rock. For relatively weak rock, the coefficient continues increasing with increasing ω, and reaches a constant value at high frequency.

5. Conclusion

General expressions for computing wave speeds in steel-lined pressure tunnels have been reformulated, analyzed, and compared for cracked or uncracked concrete and rock layers and for three different moduli of the far-field rock zone. The following assumptions have been considered: (i) frictionless and axisymmetrical waterways, (ii) linearization of equations of water motion, (iii) linear elastic behaviour of the steel-liner and pipe's wall, and (iv) infinitely long waterways.

Compared to the "complete quasi-static expression" (Eqs. (3.2) & (3.5)), the wave speed in steel-lined pressure tunnels with cracked backfill concrete and uncracked near-rock zone (Eqs. (3.2) & (3.4)) is overestimated by 4% for thin steel liners and by 1.5% for thick steel liners. If all layers are uncracked (Eqs. (3.2) & (3.3)), the wave speed is overestimated up to 8% for thin steel liners and up to 2.5% for thick steel liners. The highest differences are observed for relatively weak rock mass moduli. The "complete quasi-static expression" was also compared to other formulas in literature. For thin steel liners and weak rock mass modulus, Jaeger's and Parmakian's relationships (Eqs.(3.6) & (3.8) resp.) overestimate the water hammer velocity (Eqs. (3.2) & (3.5)) by approximately 3 to 4.5%, while in Halliwell's formula (Eq. (3.9)) this overestimation reaches 7.5%. For practical applications, this can be tolerated because of the uncertainty in the estimation of the rock mass characteristics and/or the presence of air in the water. Nevertheless, the dynamic pressures obtained from classical water hammer theory are not overly affected by such differences in wave speed. Depending on the system stiffness, the FSI may lead to higher extreme dynamic pressures with higher frequencies. Then an enhanced calculation model is required.

Based on Kuiken's (1984) work, the FSI problem with the phase, group and reference wave velocities (Eqs. (4.2) & (4.6)) has been analyzed. The dispersion equation was also solved through a numerical example. The phase and group velocities of the water-hammer mode, precursor mode, and first acoustic mode were evaluated in function of the angular frequency of the transient excitation.

For the water-hammer mode inside steel-lined pressure tunnels and open-air penstocks, FSI results show that the equivalent reference velocity is a good approximation of the phase and group velocities in low- (80 Hz) and high- (800 Hz) frequency ranges with no significant wave attenuations. In the intermediate-frequency range, the maximum relative difference of the wave velocities in steel-lined tunnels relative to the quasi-static case reaches 150%, and the maximum attenuation coefficient is reached. In the intermediate frequency range, the precursor mode has a cut-off frequency and decreases rapidly when ω increases from 255 to 320 Hz. This mode reaches, for large ω, a constant value between the quasi-static wave speed and speed of sound in unconfined water, c_T. The cut-off frequency is dependent on the longitudinal distribution of the stiffness of the liner. It can be used as an indicator to detect the presence and intensity of such local weak stiffness. In the case of open-air penstocks, the water-hammer mode presents a high cut-off frequency around 150 Hz, while the precursor mode propagates for all values of the angular frequency (ω) and can be well estimated by Skalak's formula.

In steel-lined pressure tunnels, the first acoustic mode begins to propagate at an angular frequency near 3'300 rd/s (525 Hz). This cut-off frequency depends on the radial constraint of the steel liner and varies closely with the second mode of rigid tubes. The wave velocity of this mode approaches the speed of sound, c_T, when the angular frequency becomes very large.

For the special case of unlined pressure tunnels with constant wave speed, Jaeger's equation overestimates the wave speed by 3.5% compared to the "complete quasi-static expression". Another approach was adopted by Suo and Wylie (1990a) considering the rock mass as an infinite homogeneous and isotropic cylinder and taking only the dynamic effect of the rock mass into account. Using the FSI formulations, this paper shows that the equivalent wave speed is bounded between the quasi-static wave speed and the speed of sound in unconfined water and has no cut-off frequencies. It decreases slightly at low frequencies, increases rapidly when ω increases with abrupt change of value at

intermediate frequencies, and approaches asymptotically c_T when the frequency goes to infinity. For the numerical cases studied, the decrement coefficient, in the case of hard rock, increases rapidly for small ω, reaches a maximum value, and then decreases. For relatively weak rock, the coefficient continues increasing with increasing ω, approaching a constant value at high frequencies.

In an ongoing research project, laboratory experiments as well as in-situ measurements are carried out. These experiments will allow the validation of some cases presented herein and the comparison of a calculated transient event in the time and frequency domains respectively as suggested in this paper.

Acknowledgments

The study is part of the research project *HydroNet* (Modern methodologies for the design, manufacture and operation of pumped storage plants) funded by the *Swiss Competence Center Energy and Mobility* (CCEM-CH), the *Swiss Electric Research* and the *Swiss Office for Energy*.

References

Atabeck, H.B., 1968. Wave propagation through a viscous fluid contained in a tethered initially stressed, orthotropic elastic tube. Biophysics Journal 8, 626-649.

Bürmann, W., 1975. Water hammer in coaxial pipe systems. ASCE Journal of the Hydraulics Division, Vol. 101, No. HY6, 699-715.

Chaudhry, M.H., 1987. Applied hydraulics transients, 2nd edition. Van Nostrand Reinhold Company, New York.

Fanelli, M., 1973. Hydraulic resonance in rock-bored penstocks. Water Power, September 1973, 342-346.

Flügge, W., 1973. Stresses in Shells, 2nd edition. Springer-Verlag, Berlin, Heidelberg and New York.

Ghidaoui, M.S., Zhao, M., Mclnnis, D.A., Axworthy, D.H., 2005. A review of Water Hammer Theory and Practice. Applied Mechanics Reviews 58, 49-76.

Hachem, F., Schleiss, A., 2009. The design of steel-lined pressure tunnels and shafts. The International Journal on Hydropower & Dams 16(3), 142-151.

Halliwell, A.R., 1963. Velocity of a Waterhammer Wave in an Elastic Pipe. Journal of the Hydraulics Division, ASCE, Vol. 89, No. HY4, 1-21.

Jaeger, C., 1933. Théorie générale du coup de belier: application au calcul des conduites à caractéristiques multiples et des chambers d'équilibre. Paris, Dunod.

Jaeger, C., 1972. Rock mechanics and engineering. Cambridge University Press.

Jaeger, C., 1977. Fluid Transients in Hydro-Electric Engineering Practice. Blackie & Son Limited, Glasgow and London.

Kuiken, G.D.C., 1984. Wave propagation in fluid lines. Applied Scientific Research 41, 69-91.

Kuiken, G.D.C., 1988. Amplification of pressure fluctuations due to fluid-structure interaction. Journal of Fluids and Structures 2, 425-435.

Lavooij, C.S.W, Tijsseling, A.S., 1991. Fluid-Structure Interaction in liquid-filled piping systems. Journal of Fluids and Structures 5, 573-595.

Li, Q.S., Yang, K., Zhang, L., 2003. Analytical solution for fluid-structure interaction in liquid-filled pipes subjected to impact-induced water hammer. ASCE Journal of Engineering Mechanics 129, 1408-1417.

Parmakian, J., 1963. Waterhammer analysis. Dover Publications, Inc., New York.

Rieutord, E., 1982. Transient Response of Fluid Viscoelastic Lines. Journal of Fluids Engineering 104, 335-341.

Rubinov, S.I., Keller, J.B., 1971. Wave propagation in a fluid-filled tube. Journal of the Acoustical Society of America 50, 198-223.

Rubinov, S.I., Keller, J.B., 1978. Wave propagation in viscoelastic tube containing a viscous fluid. Journal of Fluid Mechanics 88, 181-203.

Salah, B., Massouh, F., Kettab, A., Mbangangoye, B., 2001. Célérité de l'onde de coup de bélier dans les conduites enterrées. La Houille Blanche 3/4, 3-17.

Schleiss, A., 1988. Design criteria applied for the Lower Pressure Tunnel of the North Fork Stanislaus River Hydroelectric Project in California. Rock Mechanics and Rock Engineering 21(3), 161-181.

Skalak, R., 1956. An extension of the theory of waterhammer. Transactions of the ASME 78, 195-116.

Streeter, V.L., 1963. Discussion of Halliwell A.R. 1963 Velocity of a water-hammer wave in an elastic pipe. ASCE Journal of the Hydraulics Division, Vol. 89, No. HY6, 295-296.

Stuckenbruck, S., Wiggert, D.C., Otwell, R.S., 1985. The influence of pipe motion on acoustic wave propagation. Transactions ASME, Journal of Fluids Engineering 107, 518-522.

Suo, L., Wylie, E.B., 1990a. Hydraulic transients in rock-bored tunnels. Journal of Hydraulic Engineering, Vol. 116, No. 2, 196-210.

Suo, L., Wylie, E.B., 1990b. Complex wavespeed and hydraulic transients in viscoelastic pipes. Transactions ASME, 112, 496-500.

Talobre, J.A., 1967. La mécanique des roches et ses applications. Edition Dunod, Paris.

Tijsseling, A.S., 1996. Fluid-Structure Interaction in Liquid-Filled Pipe Systems: A Review. Journal of Fluids and Structures 10, 109-146.

Tijsseling, A.S., 2003. Exact solution of linear hyperbolic four-equation system in axial liquid-pipe vibration. Journal of Fluids and Structures 18, 179-196.

Tijsseling, A.S., 2007. Water hammer with fluid-structure interaction in thick-walled pipes. Computers and Structures, Vol. 85, No. 11-14, 844-851.

Tijsseling, A.S., Lambert, M.F., Simpson, A.R., Stephens, M.L., Vitkovsky, J.P., Bergant, A., 2008. Skalak's extended theory of water hammer. Journal of Sound and Vibration 310, 718-728.

Timoshenko, S.P., Goodie, J.N., 1970. Theory of elasticity. McGraw-Hill Book Co., New York, N.Y.

Wylie, E.B., Suo, L., Streeter, V.L., 1993. Fluid Transients in Systems. Prentice Hall, Fascimile Edition.

List of Figures

Fig. 1. Calculation models for steel liners with axisymmetrical behaviour
(a) Used for the quasi-static wave speed calculation.
(b) Used for the frequency-dependent wave speed calculation.

Fig. 2. Quasi-static wave speeds and relative differences (curves with arrows) calculated by the formulae of the three studied Cases (Cases 1, 2 and 3) as a function of the ratio of internal tunnel radius to steel-liner thickness for different values of E_{rm}/E_s ratio.
(a) Case 1: Backfill concrete and the near-rock mass zone are uncracked (Eqs. (3.2) & (3.3)). The relative difference compared to Case 3 (c) is indicated with the right scale.
(b) Case 2: Backfill concrete is cracked while the rock mass is not (Eqs. (3.2) & (3.4)). The relative difference compared to Case 3 (c) is indicated with the right scale.
(c) Case 3: Backfill concrete and the near-rock zone are cracked (Eqs. (3.2) & (3.5)).

Fig. 3. Quasi-static wave speeds and relative differences (curves with arrows) calculated by Jaeger's, Parmakian's and Halliwell's formulae as a function of the ratio of internal tunnel radius to steel-liner thickness for different values of E_{rm}/E_s ratio.
(a) Jaeger's formula (Eqs. (3.6) & (3.7)) and relative difference compared to Case 3 (the backfill concrete and the near-rock zone are cracked).
(b) Parmakian's formula (Eq. (3.8)) and relative difference compared to Case 3.
(c) Halliwell's formula (Eqs. (3.9) & (3.10)) and relative difference compared to Case 3.

Fig. 4. Three modes' phase and group wave speeds as a function of the angular frequency ω for an isotropic steel lined tunnel having the following input parameters: r_i=1.75 m, b=100, ρ_s=7'850 kg/m^3, E_s=210'000 MPa, f_y=580 MPa, ρ_l=2'200 kg/m^3, E_c=E_{rm}=21'000 MPa, E_{crm}=10'500 MPa, ζ=10%, μ=κ=0, σ_l^0=0, and σ_r^0=0.5·f_y·t_s. Comparison of wave speeds according to quasi-static, speed of sound in unconfined water, and equivalent reference approaches.

Fig. 5. (a) The logarithmic decrement coefficients (Eq. (4.6)) of the three propagation modes shown on Fig. 4.
(b) The amplitude ratios of the longitudinal to radial displacements ($\hat{u}_l^s/\hat{u}_r^s$) of the liner wall for the two tube modes shown on Fig. 4.

Fig. 6. (a) The variation of the precursor phase and group wave speeds (Eq. (4.1)&(4.6)) versus ω for different longitudinal stiffness constraints of a steel liner with C_l=0 and with the other input parameters similar to those shown on Fig. 4.

(b) The variation of the first acoustic phase and velocity wave speeds (Eq. (4.1)&(4.6)) versus ω for different radial stiffness constraints characterized by two different values of the internal radius of the crack rock zone (r_f) and with the other input parameters similar to those shown on Fig. 4.

Fig. 7. Comparison between the variation of the quasi-static wave speed, the speed of sound in unconfined water, the equivalent reference wave speed, and the phase and group wave speeds of the three propagation modes versus the angular frequency for an open-air penstock having the following input parameters: r_i=1.75 m, b=100, ρ_s=7'850 kg/m^3, E_s=210'000 MPa, f_y=580 MPa, μ=κ=0, σ_l^0=0 and σ_r^0=0.5·f_y·t_s.

Fig. 8. The variation of:
(a) The water-hammer-wave speed (Eqs.(4.1)&(4.6)).
(b) The logarithmic decrement coefficient (Eq.(4.6)) versus the radial frequency in an unlined pressure tunnel having the following input parameters: r_i=1.75 m, ρ_r=2'200 kg/m^3, E_{rm}=7'000, 10'000, 15'000, and 21'000 MPa.

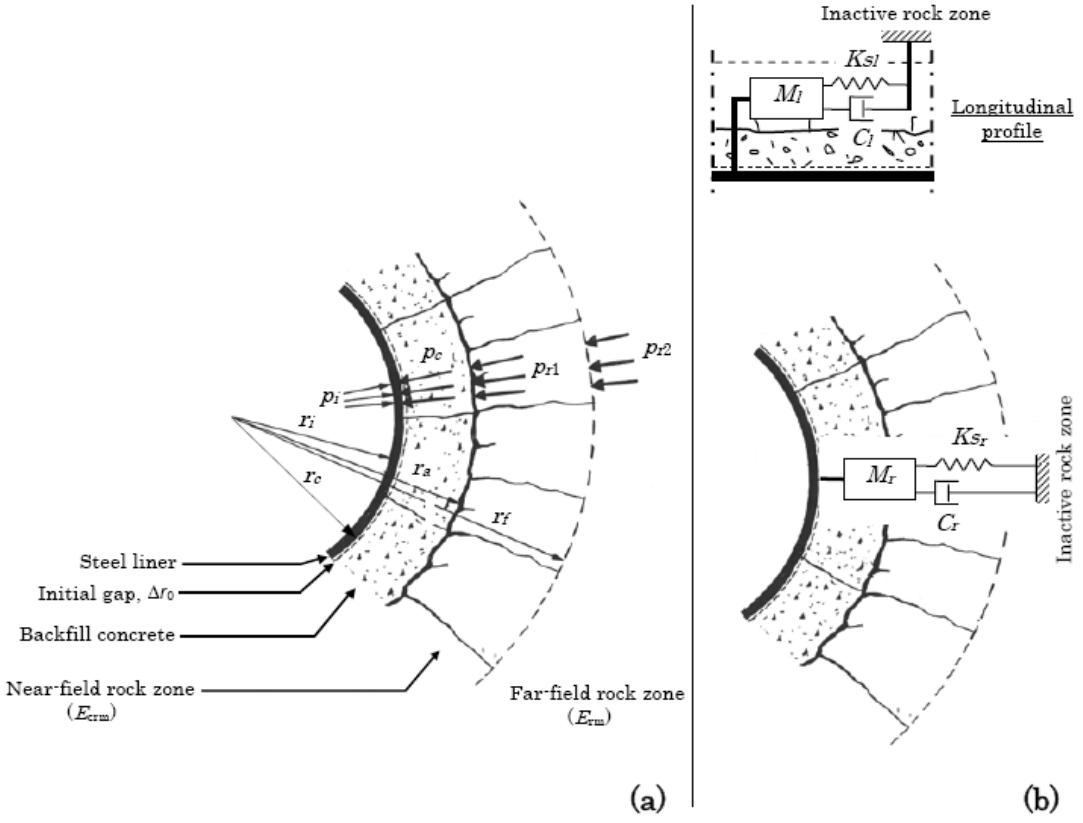

Figure 1

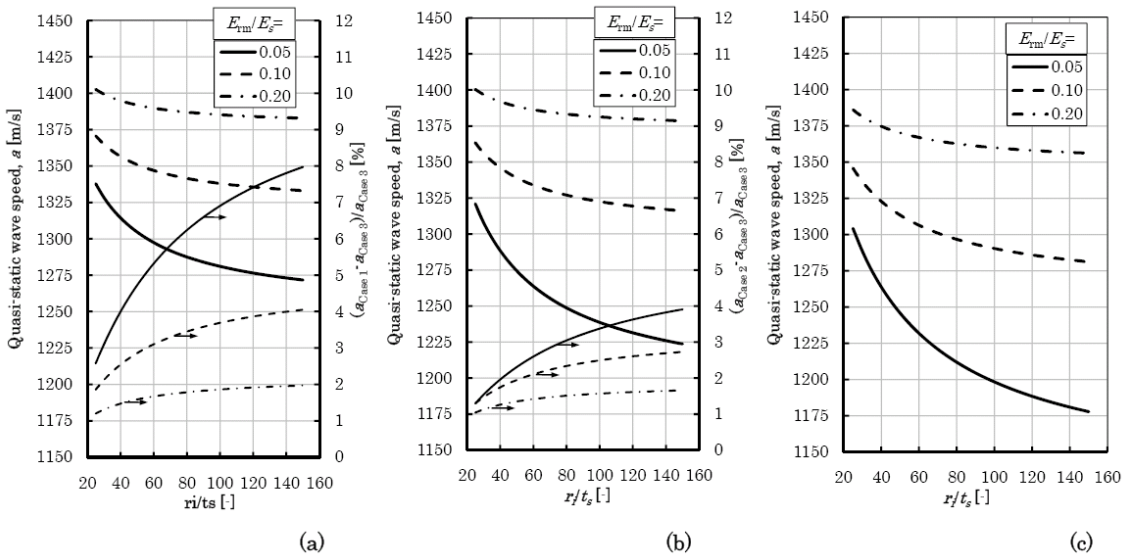

Figure 2

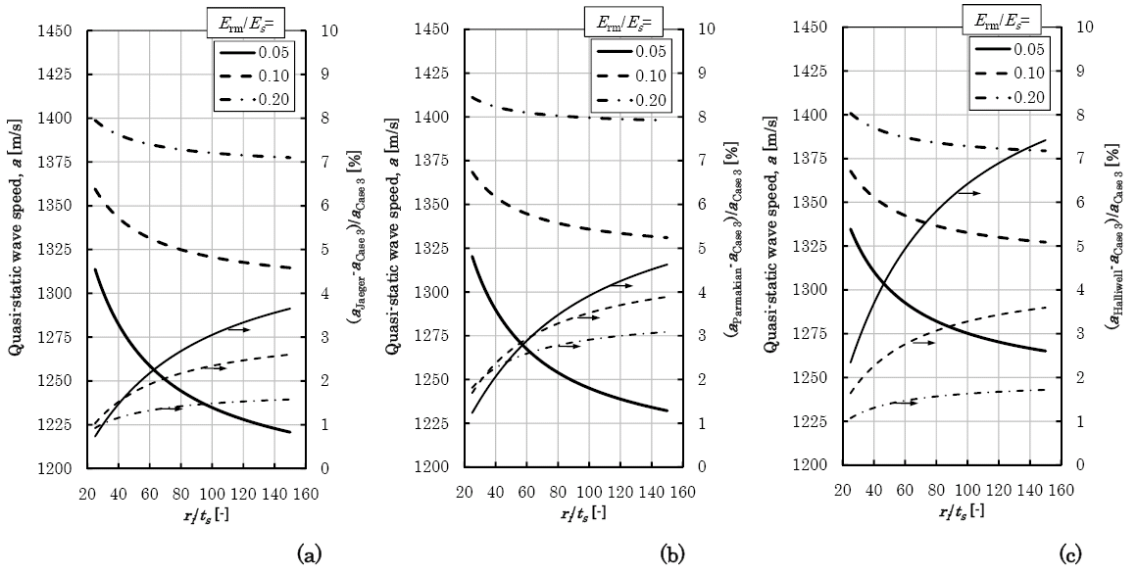

Figure 3

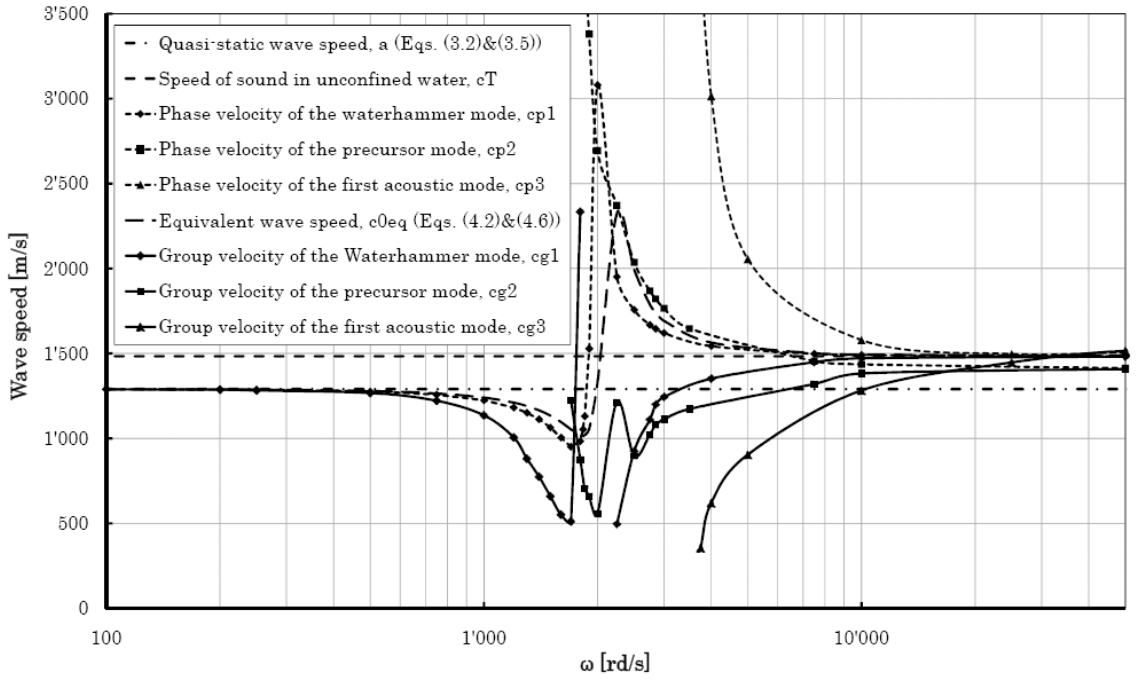

Figure 4

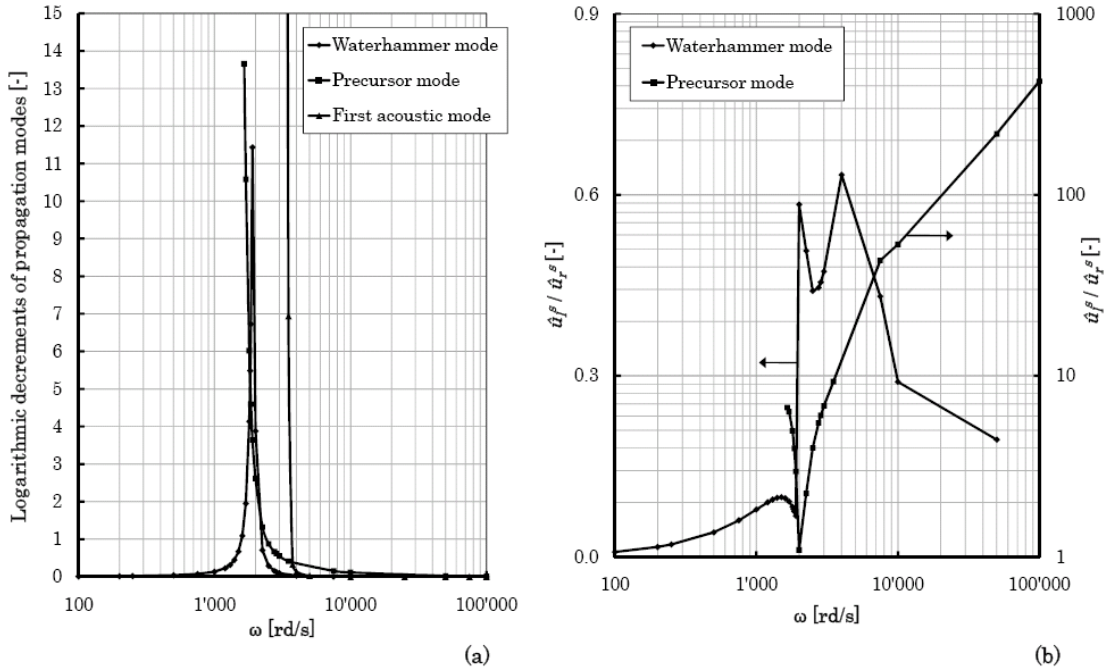

Figure 5

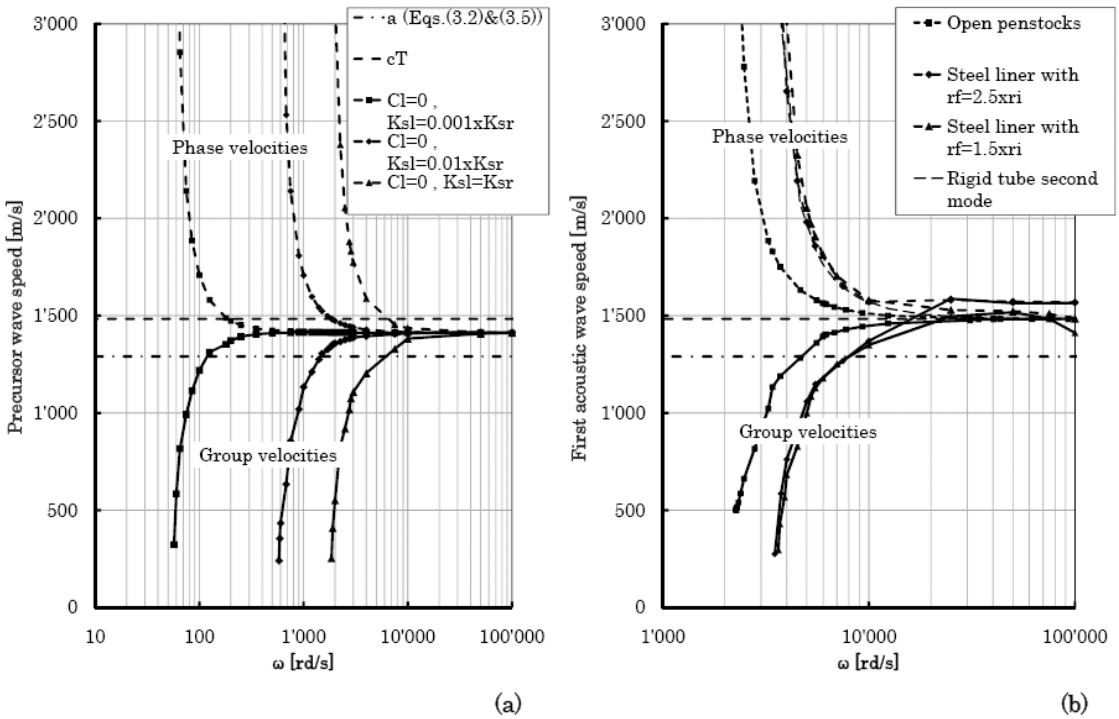

Figure 6

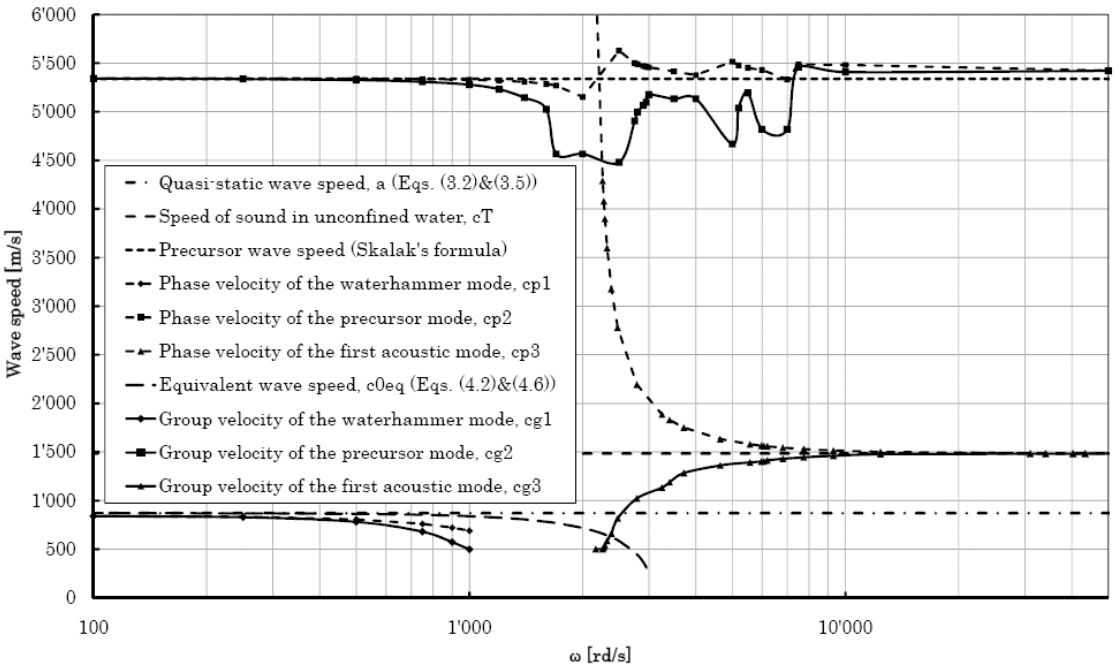

Figure 7

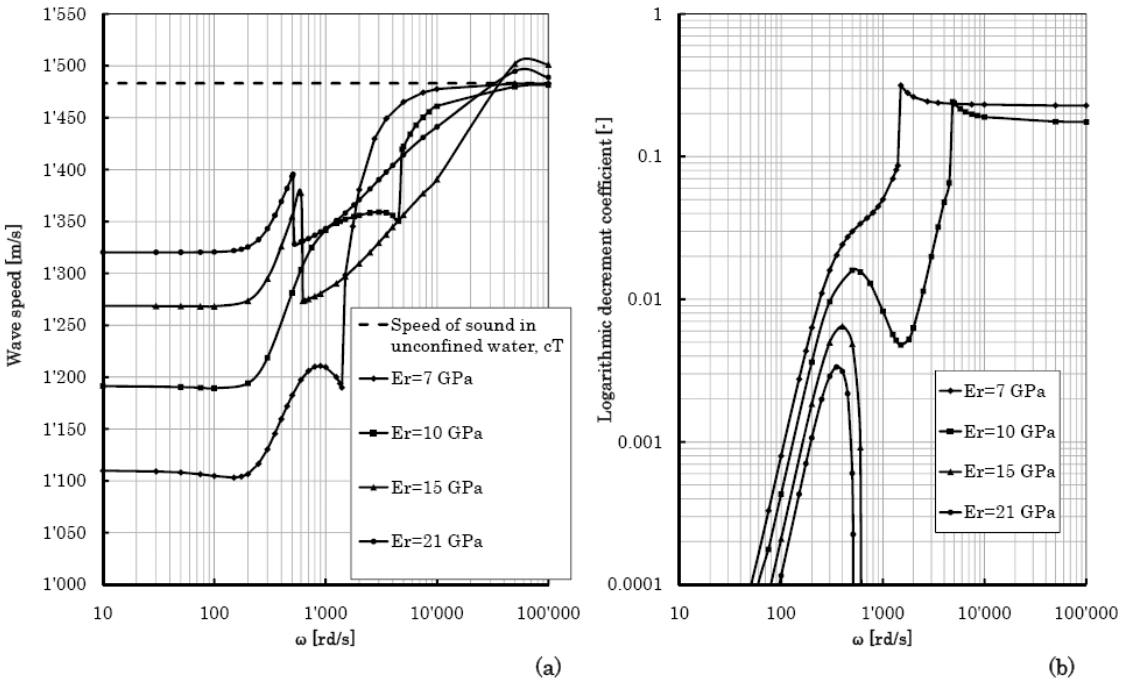

Figure 8

Detection of local wall stiffness drop in pipes using steep pressure wave excitation and wavelet decomposition

F.E. Hachem, M.ASCE[1] and A.J. Schleiss[2]

[1]Research assistant and [2]Professor and Director, Laboratory of Hydraulic Constructions (LCH), Ecole Polytechnique Fédérale de Lausanne (EPFL), Station 18, 1015 Lausanne, Switzerland.

fadi.hachem@a3.epfl.ch, anton.schleiss@epfl.ch

Abstract

A new monitoring approach for detecting, locating and quantifying structurally weak reaches of steel-lined pressure tunnels and shafts is presented. These reaches arise from local deterioration of the backfill concrete and the rock mass surrounding the liner. The change of wave speed generated by the weakening of the radial liner supports creates reflection boundaries for the incident pressure waves. The monitoring approach is based on the generation of transient pressure with a steep wave front and the analysis of the reflected pressure signals using the Fast Fourier Transform and wavelet decomposition methods. Laboratory experiments have been carried out to validate the monitoring technique. The multilayer system (steel-–concrete–rock) of the pressurized shafts and tunnels is modeled by a one layer system of the test pipe. This latter was divided into several reaches having different wall stiffnesses. Many geometric configurations were investigated by changing systematically the position of a steel, aluminum, and PVC pipe reach.

Keywords: Front wave speed; Steel-lined pressure tunnels; Pipes; Wave reflections; Transient pressure signals; Wavelet decomposition; Monitoring.

Introduction

In the past, the safety margin for dynamic water pressure loads in steel-lined pressure tunnels and shafts was considered as acceptable by using conventional design safety factors. Due to high peak energy demands, existing plants are operating nowadays under rough conditions with relatively fast and numerous valve maneuvers to regulate the turbine discharge and power. The economic and social costs due to production losses, when these water conveying structures are emptied for investigations and repairs, are considerable. On the other hand, the failure of such structures produces catastrophic landslides and debris flows and generates a need for repairs with the loss of many years of energy production income.

Traditionally, well equipped steel-lined shafts and tunnels are monitored by a set of pressure sensors, water level measurements and downstream–upstream flow meters. Pressure sensing devices are normally used to check the magnitude of the dynamic pressures relative to a predefined serviceability value. No further pressure signal processing is done since the sensors and the acquiring system are normally not fast enough to accurately collect high-frequency dynamic signals. If the water flow velocity exceeds a certain threshold, indicating a possible failure, a security shut-off valve closes automatically. This limits the volume of water leaking out from the failure by avoiding the emptying of the tunnel and reservoir upstream of the security valve. Nevertheless, and even in this case, catastrophic failure consequences can occur since the volume of leaking water between the valve and the failure location may still be very high. Any additional investigation of the steel-liner regarding excessive local deformations and steel yielding requires a dewatering of the conveying system for visual checking. Such inspection is often awkward due to the hostile conditions. Furthermore, no information can be obtained easily about the stiffness of the rock mass surrounding the steel-liner.

Besides these rather rudimentary monitoring systems, a number of more sophisticated techniques for pipeline failure and leak detection have been applied in water, gas and oil networks. This has begun with a development of a sensitivity analysis for leak location processes by Liggett and Pudar (1992). Ferrante and Brunone (2003) used the wavelet transform and its local maxima lines to retain pressure information coming from a time domain

analysis. Al-Shidhani *et al*. (2003) introduced the identification of pressure wave reflections using the wavelet decomposition. Covas *et al*. (2005) focused on leakage detection in pipe systems by means of the standing wave difference method. Beck *et al*. (2005) described a method to detect pipeline features and leaks using the cross-correlation techniques of pressure wave measurements. Misiunas *et al*. (2005) proposed a continuous monitoring approach based on the timing of the initial and reflected pressure transient waves induced by the break. Fuentes *et al*. (2006) used the inverse transient analysis approach with genetic algorithms to find the optimal location of the leak. The same approach was adopted by Shamloo and Haghighi (2009) to determine numerically the leak parameters including their number, location, and size. Taghvaei *et al*. (2010) analyzed experimentally the pressure reflections from the leak using wavelet filtering followed by Cepstrum analysis.

From the above overview, it can be concluded that there is a large number of techniques that can deal with leak detection in pipelines. They all assume that the pressure wave speed is a constant value throughout the pipeline length. Nevertheless, no references were found for investigating the wave reflections coming from weak reaches with different hydro-acoustic parameters such as wave speed.

Therefore, a monitoring method for steel-lined pressure shafts and tunnels is proposed in this paper. It is based on processing the reflection records of steep transient pressure waves in an experimental test pipe. Under an axi-symmetrical behavior, the multilayer system (steel–concrete–rock) of the pressurized shaft can be modeled by one layer system. The local deterioration of the backfill concrete and/or the rock zone surrounding the liner results in a so called “weak reach” which reduces the overall wave speed and produces reflection boundaries for the incident pressure waves. Thus, the test pipe was divided into several reaches having different wall stiffnesses. For the detection for longitudinal stiffness heterogeneity, different geometric configurations of the steel test pipe were examined by changing systematically the position of an aluminum and PVC pipe reach of 50 cm length. For the analysis of the pressure signals, three approaches were used to estimate the wave front speed inside the test pipe. For prediction of the incident–reflection travel time between the weak reach boundaries and the pressure sensor, the Fast Fourier Transform and wavelet decomposition methods were applied.

Theoretical background

Basic equation of acoustic plane waves

The propagation of sound waves in confined water inside pipes and tunnels is modeled by an equation of motion (conservation of momentum) and an equation of continuity (conservation of mass). Assuming a constant water density, slightly compressible water, low Mach number and one spatial propagation dimension (along the pipe's longitudinal dimension x), these equations can be written as follows:

$$\begin{cases} \dfrac{\partial v}{\partial t} + g\dfrac{\partial h}{\partial x} + f\dfrac{|v|v}{2D} = 0 \\ \dfrac{\partial h}{\partial t} + \dfrac{a^2}{g}\dfrac{\partial v}{\partial x} = 0 \end{cases} \tag{1}$$

where, $h(x,t)$ is the piezometric head, $v(x,t)$ is the water flow velocity, t is the time, g is the acceleration due to gravity, a is the speed of sound in water or the pressure wave velocity, f is the Darcy–Weisbach friction factor and D is the internal diameter of the tunnel. The differentiation and combination of these two conservation equations leads to the acoustic plane wave equation expressed as (Bergant et al., 2008):

$$g\frac{\partial^2 h}{\partial x^2} - \frac{g}{a^2}\frac{\partial^2 h}{\partial t^2} = -f\frac{|v|}{D}\frac{\partial v}{\partial x} \tag{2}$$

For a pipe with uniform cross section, the pressure wave velocity can be estimated by the following general formula (Wylie et al., 1993),

$$a = \sqrt{\frac{1}{\rho_0\left(\dfrac{1}{K_w} + \dfrac{1}{A}\cdot\dfrac{\mathrm{d}A}{\mathrm{d}p}\right)}} \tag{3}$$

where dA is the variation of the cross-sectional area A of the pipe caused by the variation of the internal water pressure dp and K_w is the bulk modulus of water. In steel-lined pressure tunnels and shafts considering neither the fluid–structure interaction (FSI) nor the dynamic effect of the tunnel wall, the ratio dA/dp is a constant value which depends on the geometrical and mechanical characteristics of the steel liner and on the state (cracked or uncracked) of the surrounding backfill concrete and rock mass (Hachem and Schleiss, 2010).

In plain strain conditions and considering the hypothesis of linear elasticity and small deformations, Eq. 3 can be written as follows (Halliwell, 1963; Streeter, 1963;Timoshenko and Goodie, 1970):

$$a = \sqrt{\frac{1}{\rho_w \left(\frac{1}{K_w} + \frac{2}{r_i} \cdot \frac{\mathrm{d}u_r^s(r)}{\mathrm{d}p} \right)}} \tag{4}$$

in which $\frac{\mathrm{d}u_r^s(r)}{\mathrm{d}p}$ is the first derivative of the radial displacement of the steel liner u_r^s relative to the internal pressure p at the water–liner interface of radius r_i. The $\frac{\mathrm{d}u_r^s(r)}{\mathrm{d}p}$ ratio is nothing else than the inverse of the radial stiffness of the tunnel wall. By ignoring the presence of air in water, which can drastically change the pressure wave speed, the velocity of a pressure wave travelling between two cross-sections of a tunnel will be affected by every change of the radial stiffness of its wall. In laboratory tests, the change of the wall stiffness can be modeled by using pipe reaches having different ($E \cdot th$) values than the rest of the test pipe. E is the Young modulus and th is the thickness of the pipe wall.

The general solution of Eq. 2 is the summation of a progressive and a retrograde wave propagating at the wave speed a in opposite directions along the tunnel's longitudinal axis. These waves are generated at any time t by local excitation that moves variables h and v away from their steady-state values.

At tunnel junctions characterized by a change of the hydro-acoustic parameters (the flow area A and/or the wave speed a), an incident wave is reflected and transmitted. Fig. 1 shows the time behavior of a theoretical rectangular wave front propagating in water and crossing two junctions that limit a pipe reach having a wave speed value a_2 lower than the rest of the pipe (a_1). For steel-lined pressure tunnels, such a decrease of the wave speed can be the consequence of partial or total loss of the stiffness of the exterior support of the steel liner which is provided by the surrounding backfill concrete and rock mass. This reach is called ''weak reach'' throughout this paper.

According to Fig. 1, an incident pressure wave of magnitude (h_i-h_0) is divided into transmitted and reflected waves when crossing junction 1. For a uniform cross-section flow area, the magnitude of the transmitted wave (h_{t1}-h_0) is given by (Wylie et al., 1993)

$$h_{t1} - h_0 = \frac{2}{1+\frac{a_1}{a_2}}\left(h_i - h_0\right) \tag{5}$$

where, h_0, h_i and h_{t1} are the steady-state, incident and transmitted piezometric heads, respectively. The same phenomenon is reproduced when the pressure wave crosses the downstream end of the weak reach (junction 2). According to the direction of the first incident wave h_i, junctions 1 and 2 are called the upstream and downstream ends of the weak reach.

Pressure excitations

The transient pressure excitations inside the water must have enough energy in the wave front to interact with the surrounding walls of the structure even after dissipation during longitudinal propagation. In a hydropower plant, such excitations are generated by the change of the flow rate at the turbines. Consequently, a water-hammer propagating along the conveying system occurs (Parmakian, 1963; Chaudhry, 1987). These excitations are repeated many times a day when synchronizing the energy production to the grid demand. Therefore, with a monitoring method based on processing of this type of water transient pressure, a large data base can be acquired. This allows a close follow up of the tunnel and shaft radial deformation. Depending on the flow rate change, a water-hammer with steep front can be generated. Nevertheless, the localization of weak zones becomes difficult for rather slow changes of flow rate. The front of the incident pressure wave becomes soft as well as the slopes of the negative pressure drift induced by the reflected waves from the weak reach boundaries

Another artificial type of water pressure excitation could be produced by an explosive shock wave generated in water near the reservoir's intake structure or near the tunnel–shaft junction inside the surge tank. This type of excitation is more risky and complicated to produce than the water-hammer phenomenon resulting from normal operation. Furthermore, the monitoring of shafts and tunnels would have only a limited number of in-situ data measurements. The main advantage of such artificial excitation, in comparison to water-hammers, is the possibility of

generating an incident wave with a steep front, allowing more accurate localization of the weak zones. In this paper, the processing of the transient pressure of laboratory experimental data produced by a steep wave excitation is analyzed.

Localization of the weak reach based on wave timing

The location of a weak reach of steel-lined pressure tunnel can be determined on the basis of the timing of pressure wave reflections that occur at the boundaries of this reach. The travel times of these transient waves can be found by using pressure measurement sampled at high frequency at two points of the waterway. For steel-lined pressure tunnels and shafts, these points are restricted to the accessible reaches of the steel liner. They are normally located inside the valves chambers situated downstream of the reservoir intake, downstream of the surge tank, and at the entrance of the power house. The travel times are then transformed to distances or wave path lengths using the simple formula:

$$l = \frac{a \cdot t}{2} \tag{6}$$

where, l is the distance between the pressure sensor and the boundary of the weak reach, a is the front wave speed in water and t is the travel time that an incident wave needs to travel from the pressure sensor towards the boundary of the weak reach and to come back, after reflection, to the same sensor's position. In order to localize the weak reach, a good estimation of the front wave speed and of the incidence–reflection travel time are required.

Estimation of the front wave speed, a

Three time-based approaches are used to estimate the time needed by the water wave front to travel from the upstream pressure position (*P1*) to the downstream one (*P2*). The upstream and downstream nomenclatures for pressure positions or data, *P1* and *P2*, are defined according to the direction of the first incident wave h_i. The values of the front wave speed are then extracted by dividing the known distance separating the two sensors by the predicted travel time.

The first approach extracts the time that separates the maximum values of the front pressure measurements. The second approach determines, for each pressure record, the time at the intersection point of two regression lines correlating the steady-state and the first front pressure

data, respectively. The third approach uses the cross-correlation technique to calculate the time-lag which separates the front wave lobes of *P1* and *P2* data. For discrete functions, the cross-correlation is defined as follows (Lange, 1987):

$$(P2 * P1)[n] = \sum_{m=-\infty}^{\infty} P2^{*}[m] \cdot P1\,[n+m] \tag{7}$$

where, *P2** is the complex conjugate of *P2* and *n* and *m* are positive integers.

A unique value of the front wave speed is finally retained for each test. It is the one of the three wave values obtained from the three approaches which is bounded by the two others.

Estimation of the incident–reflection travel time, t

A first approximation of the incident–reflection travel time is obtained by the Fast Fourier Transform (FFT) applied to the pressure records *P1* and *P2*. The FFT gives a global representation of the frequency content of these signals over the entire time domain. For the configurations with weak reach, peaks should occur at the fundamental and harmonic frequencies. They correspond to the wave reflection solicitations issuing from the weak reach boundaries.

In the second approach, the results of the FFT approximation and the wavelet transform and decomposition techniques are used to localize more accurately the boundaries of the weak reach. One pressure record is sufficient to estimate the incident–reflection travel time between the pressure sensor's position and these boundaries. Wavelets are mathematical functions that decompose a signal into its constituent parts using a set of wavelet basis functions. This decomposition is very similar to standard Fourier transforms (which are based on sinusoids). They can capture local rapid and large signal fluctuations rather than giving only averaged information over the entire time domain. The family of basis functions used for wavelet analysis is created both by dilations (scaling) and translations (in time) of a mother wavelet (Mallat, 1990). The continuous wavelet transform coefficients, *Wf*(*u*,*s*), are obtained by convolving the signal *f*(*t*) with the translations *u* and dilations *s* of the complex conjugate $\psi^{*}_{u,s}$ of the mother wavelets $\psi_{u,s}$, according to the following equation:

$$Wf(u,s) = \int_{-\infty}^{+\infty} f(t) \cdot \psi^*_{u,s} \; dt \tag{8}$$

where the mother wavelets $\psi_{u,s}$ are generated by

$$\psi_{u,s}(t) = \frac{1}{\sqrt{s}} \psi\left(\frac{t-u}{s}\right) \tag{9}$$

In discrete analysis and for discrete signals of finite energy, the reconstruction of the signal $f(t)$ is performed by using the inverse wavelet transform:

$$f(t) = \sum_{j\in\mathbb{Z}} \sum_{k\in\mathbb{Z}} Wf(k,j) \cdot \psi_{k,j}(t) \tag{10}$$

where j is the scale index or the decomposition level ($s = 2^j$) and k is the time index ($u = k \cdot 2^j$). By fixing j and summing over k, the detail coefficient at level j, D_j, is defined by:

$$D_j(t) = \sum_{k\in\mathbb{Z}} Wf(k,j) \cdot \psi_{k,j}(t) \tag{11}$$

The signal $f(t)$ is thus the sum of its wavelet details at different levels j. By considering a reference decomposition level J, the approximation coefficient at level J is:

$$A_J(t) = \sum_{j>J} D_j(t) \tag{12}$$

So, the wavelet decomposition technique is nothing other than the splitting of the original signal into approximation and detail coefficients by using wavelets. At each decomposition level the signal is passed through a pair of high-pass and low-pass filters. The former gives the high-frequency signal components, known as detail coefficients while the latter gives the low-frequency components or the approximation coefficients. A wavelet decomposition tree up to level 4 is shown in Fig. 2, where A_i and D_i are the i^{th}-level approximation and detail coefficients, respectively. After j levels of decomposition, the original signal $f(t)$ can be finally expressed as:

$$f(t) = A_j + \sum_{i=1}^{j} D_i \tag{13}$$

In this work, the *Daubechies* wavelet (db10), shown in Fig. 3, is used for the family of basis functions. The numerical index refers to the order or number of coefficients of the wavelet. The db10 doesn't have an explicit expression. Its central frequency is equal to 0.68421 Hz.

Experimental tests and data analysis

Experimental set-up

An experimental facility was assembled at the Laboratory of Hydraulic Machines of EPFL (Ecole Polytechnique Fédérale de Lausanne). This facility was specially designed for detecting the change of wall stiffness of a test pipe using recorded pressure data generated either by an external water pressure excitation source or by a rapid change of the flow rate's producing water-hammer phenomena inside the pipe. This paper deals with pressure measurements obtained from an external water pressure excitation.

The configuration of the experimental set-up is shown in Fig. 4**.** It consists of a test pipe with an internal diameter of 150 mm and a length of 6.25 m supplied with water by a reservoir and a variable speed pump. The pipe is divided into several reaches of 0.5 m and 1.0 m length fitted together with flanges having an external diameter of 285 mm and a thickness of 24 mm. The flanges are also used to rigidly fix the test pipe along its length in order to minimize any longitudinal and transversal movements during test events. On the 10 m supply conduit, an electromagnetic flow meter is placed to measure the steady state flow. On the highest point of this conduit, an air purge valve is installed to evacuate the captured air inside the test rig. A first control and security valve followed by an elastic deformable joint (TUBOFLEX) are located at the downstream end of the supply conduit, which is protected against water-hammer by a pressurized air vessel. The downstream end of the test pipe is equipped with a shut-off valve operated by an air jack. It is followed by a purge valve, an elastic TUBOFLEX joint and a second control valve located at the entrance of the supply reservoir. The external pressure excitation, transmitted to the water through the jack axis, and the closure of the shut-off valve are carried out automatically by the air jack with input and output electro-valves. The volume of air needed to activate the jack is provided by an air compressor with a constant pressure of 10 bars. The opened and closed states of the shut-off valve are detected by two diffuse sensors with an infrared beam. The data acquisition system comprises: (i) two pressure transducers (HKM-375M-7-BAR-A, Kulite) with a pressure range from 0 to 7 bars and an accuracy of 0.5%, (ii) a NI-USB-6259 acquisition card M series with 32 analogue input channels and 2 analogue output

channels to activate the two electro-valves of the shut-off valve, and (iii) a notebook computer connected to the acquisition card through a USB cable. The sampling frequency was fixed to f_s=15 KHz. LabView 8.6, MATLAB 2008b and Diadem 11.0 software were used for acquiring, controlling and processing the experimental data.

Test pipe configurations

Five pipe configurations were tested with approximately the same initial steady flow conditions, the same air pressure in the compressor, and the same mean pressure at the entrance of the test pipe. The basic configuration of the test pipe, named "Steel," corresponds to steel pipe reaches of 100 and 50 cm length with 4.5 mm wall thickness arranged in a basic configuration according to Fig. 5. In the configuration "Steel+Alu1," the first 50 cm pipe reach (the first pipe reach is that nearest the air vessel) is replaced by an aluminum pipe with 5 mm wall thickness. In the configurations "Steel+PVC1, 2 or 3" the first, second or third 50 cm long pipe reach is replaced by a 5 mm thick PVC pipe. For each test pipe configuration, many repetitive tests were carried out giving a total number of 67 tests (19 for "Steel," 6 for "Steel+Alu1," 18 for "Steel+PVC1," 12 for "Steel+PVC2" and 12 for "Steel+PVC3"). The theoretical radial stiffness ($E \cdot th$) of steel, aluminum and PVC reaches are 945, 345 and 15 MN/m, respectively.

Weak reach localization

In Fig. 6(a) five records of the normalized transient water pressure, *P1,* for the five different configurations of the test pipe are shown. The normalization is done by dividing the pressure values by the maximum pressure at the wave front. These transient pressures are caused by the impact of the pressurized air on the jack piston. This excitation is transmitted to water inside the test pipe by means of the jack axis. Fig. 6(b) depicts the five pressure signals, *P2* for the same tests.

The front wave speeds *a* of all 67 tests have been computed using the three approaches presented in 2.3.1. In Fig. 7, the mean and the standard deviation of *a* for each pipe configuration are shown. Based on the low values of the standard deviation (below 11.7 m/s) and the clear differences observed between the mean wave speed of "Steel" and "Steel+PVC"

configurations, it may be concluded that the wave speed computed according to the three approaches using the dynamic pressure records at both ends of the test pipe can be considered as a global indicator of large changes in the stiffness of the pipe wall (relative changes $[(E{\cdot}th)_{PVC}-(E{\cdot}th)_{Steel}]/(E{\cdot}th)_{Steel}$ near 98%). For the test pipe configurations with a 50 cm aluminum reach having a ($E{\cdot}th$) value equal to 345 MN/m, the drop of the wave speed values relative to the "Steel" configurations is small.

A first approximation of the incident–reflection travel time t, is performed using the Fast Fourier Transform with Hanning windowing. The normalized FFT density spectrums of all the tests signals *P1* and *P2* are computed. The normalization is obtained by dividing all the FFT magnitudes by the magnitude computed at 100 Hz. Fig. 8 shows an example of the normalized FFT for the *P1* (Fig. 8(a)) and *P2* (Fig. 8(b)) signals shown in Figs. 6(a) and 6(b). The detection of frequencies that correspond to the reflected wave from the boundaries of the weak reach is done by a trial and error procedure. For each test configuration, a couple of peak frequencies composed by one FFT *P1* and one FFT *P2* peaks, is chosen. The frequency $f_{P1,P2}$ of the propagating wave between sensors *P1* and *P2* is then estimated according to the following equation:

$$f_{P1,P2} = \frac{f_{\max,P1} \cdot f_{\max,P2}}{f_{\max,P1} + f_{\max,P2}} \tag{14}$$

where $f_{\max,P1}$ and $f_{\max,P2}$ are the frequencies at the FFT maximum peak of *P1* and *P2,* respectively. The frequencies $f_{P1,P2}$ are then compared to the theoretical value obtained from the ratio $a/\left(2 \cdot d_{P1,P2}\right)$ where a is the front wave speed of the test pipe configuration and $d_{P1,P2}$ is the distance separating the two sensors positions. The pair of frequencies which gives the nearest $f_{P1,P2}$ frequency relative to the theoretical value is retained. These values are also shown on Figs. 8(a) and 8(b). The corresponding predicted travel distances (computed according to Eq. 6) and the error relative to the real path length are presented in Table 1. The FFT approach can roughly predict the position of the weak reach with one path length relative to each pressure sensor. The error in predicting the position of the weak reach relative to the real position of its middle varies from 1.4% to 33.7%.

To localize more accurately the weak reach, the wavelet transform and decomposition techniques are applied to pressure signal *P1*. The decomposition at level *j* is related to the wavelet scale factor, *s*, by $s = 2^j$. For a sampling time step of $1/f_s$, the scale is associated to a pseudo-frequency, f_a by

$$f_a = \frac{f_c \cdot f_s}{s} \tag{15}$$

where f_c is the central frequency of the db10 wavelet (=0.68421 Hz). In low dispersion media, the shifts in the water pressure signals caused by reflections have a slope value close to the front slope of the incident wave. To capture accurately these shifts in the time domain, an appropriate decomposition level with a pseudo-frequency near but higher than the quarter-frequency of the wave front should be used. The latter frequency is estimated according to the following equation:

$$f_{\frac{1}{4}front} = \frac{1}{4\left(t_{\max} - t_{\text{int}}\right)} \tag{16}$$

where t_{max} is the time of the maximum front pressure and t_{int} is the time of the intersection point of two regression lines correlating respectively the steady-state and the first front pressure signal. The mean quarter-frequency of the incident waves generated during laboratory tests is equal to 357 Hz. From Eq. 2 it can be concluded that level 4 (with a pseudo-frequency of 641.4 Hz) should be used. The detail D_4 associated with the approximation A_4 is then investigated in order to find the incident–reflection travel time, *t*.

In Fig. 9, an example of the normalized graphs (normalization relative to their maximum values) of A_4 and D_4 for the four pipe configurations is given. A window between times 0.02 and 0.05 second of the wavelet decomposition-level 4 is shown for the pressure records *P1* presented in Fig. 6(a). The two slopes that limit the negative pressure shifts caused by reflections from the weak reach boundaries are time-located by two positive peaks of D_4. The shifts themselves mark A_4 with minimum peaks. Therefore, the incident–reflection travel time of each weak reach boundary corresponds to the difference between the maximum peak time of D_4 that bounds a minimum peak of A_4 and the time when the pressure wave front passes through *P1*. The time t_{int} of the front wave pressure *P1* is taken as the time origin to locate the upstream boundary. The time t_{max} at the maximum pressure of the wave front is considered as

the origin of time to locate the downstream boundary. For each test configuration, the first adequate maximum peak in D_4 is the one that has the closest time to the value obtained by inversing the frequency $f_{max,P1}$. The second D_4 maximum peak is the one that bounds the A_4 minimum peak. These peaks are marked by vertical lines on Fig. 9. The corresponding estimated values of the incident–reflection times, the predicted position of the weak reach boundaries, and the relative error are given in Table 2. The transformation of the incident–reflection time to distance for the upstream boundary is performed with the mean front wave speed of the "Steel" configuration. The downstream boundary distance is predicted with the front speed of the tested configuration between the two boundaries and the front speed of the "Steel" configuration for the rest of the path length. The errors on distances relative to the real values vary between 0.73% and 8.17%. In Figs. 10(a) and 10(b), the means and the standard deviations of distances between the boundaries of the weak reach and the position of the pressure sensor *P1* are given. These statistical parameters are computed using the data of the 48 tests in which a weak reach of Aluminum or PVC is used. The highest relative error of about 7% occurs when localizing the weak reach in the middle of the test pipe. The relative mean error for the localization of the upstream and downstream boundaries of "Steel+Alu1," "Steel+PVC1," "Steel+PVC2" and "Steel+PVC3" configurations are significantly small and are equal to 3.5%, 1.1%, 5.7% and -1.5%, respectively.

Stiffness of the weak reach

The stiffness $(E \cdot th)_{WR}$ of the weak reach of the test pipe can be estimated using the wave speed relation for pipes and open penstocks. This relation is derived from Eq. 4 and can be written, after rearrangement, as follows:

$$(E \cdot th)_{WR} = \frac{2 \cdot r_i \cdot \lambda_3}{\frac{1}{\rho_w \cdot a_{WR}^2} - \frac{1}{K_w}} \tag{17}$$

where $$\lambda_3 = \begin{cases} 1 - 0.5 \cdot \nu_s & \text{if the penstock can freely slip in the longitudinal direction} \\ 1 & \text{if the penstock has expansion joints over its entire length} \\ 1 - \nu_s^2 & \text{if the penstock is blocked in the longitudinal direction} \end{cases}$$

and a_{WR} is the front wave speed in the confined water inside the weak reach and ν_s is Poisson's ratio for steel. The only unknown parameter in Eq. 4 is a_{WR}. It can be calculated by using the estimated value of the wave speed between sensors *P1* and *P2* and the estimated length of the weak reach. This is done according to the following equation:

$$a_{WR} = \frac{l_{WR}}{\frac{d_{P1,P2}}{a_{P1,P2}} - \frac{\left(d_{P1,P2} - l_{WR}\right)}{a_{basic}}} \tag{18}$$

where l_{WR} is the estimated length of the weak reach, $a_{P1,P2}$ is the estimated front wave speed of the test pipe configuration with weak reach, and a_{basic} is the mean front wave speed of the basic test pipe configuration. The real and estimated stiffness of the weak reach for the tested pipe configurations are given in Fig. 11 for the pressure records of Figs. 6(a) and 6(b). Also the estimated mean stiffness of the "Steel" configuration is shown. It is determined by averaging the values obtained from Eq. 4 in which a_{WR} is replaced by the steel front wave speed between *P1* and *P2*. The real stiffness for this configuration is the product of the steel Young's modulus of 210,000 MPa and the thickness of the steel pipe wall of 4.5 mm. In Fig. 11, the following input values have been used:

r_i =75 mm ; K_w =2,200 MPa ; ρ_w =1,000 kg/m^3

ν_s = 0.30 ; ν_{Alu} = ν_{PVC} = 0.40 ; λ_3 = 1- $\nu_{s,Alu,PVC}{}^2$

In Fig. 12, the mean and the standard deviation of the stiffness of the weak reach is shown for each test pipe configuration. A maximum relative mean error of about 33.5% is observed for the "Steel+Alu1" test pipe configuration. For the "Steel+PVC1, 2 and 3" configurations, these relative mean errors are 22.6%, -9.7% and 29.2%, respectively.

Conclusions

A new technique to detect the position and severity of a stiffness change in pipe walls is suggested and validated with experiments. It combines the FFT and the wavelet decomposition techniques of water pressure records at two measurement sections of the test pipe. The signal

processing procedure was applied successively on 67 tests by using a pressure excitation source with steep wave front. The following points may be concluded:

1. The measured water transient pressures at two end positions of the test pipe can be used to predict the front wave speed of an excitation travelling between them. Three different methods were applied to estimate this crucial parameter required in the time–distance transformation process. They are based on: (i) the determination of the time separating the maximum front peaks of the signals, (ii) the time separating the intersection point of the regression line for the steady-state pressure and the regression line for the first pressure front, and (iii) the cross-correlation method. It is shown that this parameter could be a global indicator of large changes in stiffness (stiffness decreases down to 98%) of the pipe wall.
2. It is possible to extract useful information from the reflected pressure signals induced by the boundaries of a weak reach of the test pipe. The localization routine of the weak reach begins with an FFT analysis of the two measured pressure signals. This allows a rough approximation (between 1.4% and 33.7%) of the middle position of the weak reach. The time obtained by this approach is used to choose the appropriate peaks in the details and approximations of the wavelet decomposition of one measured signal. This latter analysis predicts very well the position of the weak reach boundaries with a maximum relative mean error of 5.7%.
3. Once the length of the weak reach is found, the severity of the local stiffness change of the pipe wall can also be estimated by using the standard wave speed equation inside the weak reach. This wave speed is determined from the predicted length of the weak reach and the estimated front wave speed of the test pipe configuration. The relative mean errors reach a maximum of 33.5% for all the tested configurations.

In an ongoing research, more laboratory experiments as well as in-situ measurements will be carried out. The experiments will allow the validation of the localization procedure for different weak reach lengths and for more than one weak reach in the test pipe. It is also very interesting to examine the capabilities of such a procedure for localizing weak reaches on the basis of water-hammer signals. The in-situ measurements using dynamic pressure sensors at both ends

of a pressure shaft of a pumped-storage power plant will give additional information about the steepness, energy and dissipation of wave fronts generated during start-up and shut-down of pumps and turbines. The influence of the captured air inside the shaft on the estimation of the front wave speed will be also investigated.

Acknowledgments

The study is part of the research project *HydroNet* for the design, manufacture and operation of pumped storage plants funded by the *Swiss Competence Center Energy and Mobility* (CCEM-CH), the *Swiss Electrical Research* and the *Swiss Office for Energy*.

Notation

The following symbols are used in this paper:

a = speed of sound in water or pressure front wave velocity;

a_{basic} = estimated mean front wave speed of the basic test pipe;

$a_{P1,P2}$ = estimated front wave speed of the test pipe configuration;

a_{WR} = front wave speed in water inside the weak reach of pipes, penstocks or steel-lined pressure tunnels;

A = internal cross-sectional area of the pipe or the steel liner;

A_i = i^{th}-level approximation coefficient in wavelet decomposition;

D = internal diameter of the tunnel;

D_i = ith-level detail coefficient in wavelet decomposition;

$d_{P1,P2}$ = distance between sensors *P1* and *P2*;

E = elasticity modulus;

E_{app} = apparent elasticity modulus of rock mass;

E_s = elasticity modulus of steel liner;

f = Darcy–Weisbach friction factor;

f_a = wavelet pseudo-frequency;

f_c = central frequency of the db10 wavelet;

$f_{P1,P2}$ = frequency of the propagating wave between sensors *P1* and *P2*;

$f_{max,P1}$ = frequency at the FFT maximum peak of *P1*;

$f_{max,P2}$ = frequency at the FFT maximum peak of *P2*;

f_s = sampling frequency;

$f_{1/4front}$ = quarter-frequency of the wave front;

g = acceleration due to gravity;

h = piezometric head;

h_0 = steady-state piezometric head;

h_i = piezometric head of the incident pressure wave;

h_{t1} = piezometric head of the transmitted pressure wave;

j = level of wavelet decomposition;

K_w = bulk modulus of water;

l = path length of the pressure wave;

l_{WR} = estimated length of the weak reach;

m,n = positive integers;

p = internal water pressure;

$P1$ = transient pressure records at the sensor position *P1*;

$P2$ = transient pressure records at the sensor position *P2*;

r_c = external radius of the pipe, penstock or steel liner;

r_i = internal radius of the pipe or the steel liner;

s = wavelet dilation;

t = time;

th = pipe, penstock or steel liner wall thickness;

t_{int} = time separating the intersection point of the regression line for the steady-state pressure and the regression line for the first pressure front;

t_{max} = time of the maximum front pressure;

u = wavelet translation;

u_r^s = radial displacement of the steel liner;

v = water flow velocity;

Wf = continuous wavelet transform coefficients;

x = longitudinal coordinate according to the tunnel axis;

ν_{Alu} = Poisson's ratio for aluminum;

ν_{PVC} = Poisson's ratio for PVC;

ν_{rm} = Poisson's ratio for the rock mass;

ν_s = Poisson's ratio for steel;

ρ_w = unit mass of water;

$\Psi_{u,s}$ = mother wavelet of translation u and dilation s;

References

Al-Shidhani, L., Beck, S. B. M., and Staszewski, W. J. (2003). “Leak monitoring in pipeline networks using wavelet analysis.” *Key Engineering Materials*, Vols. 245–246, 51–58.

Beck, S. B. M., Curren, M. D., Sims, N. D., and Stanway, R. (2005). “Pipeline network features and leak detection by cross-correlation analysis of reflected waves.” *Journal of Hydraulic Engineering*, 131(8), 715–723.

Bergant, A., Tijsseling, A., Vitkovsky, J., Covas, D., Simpson, A., and Lambert, M. (2008). “Parameters affecting water-hammer wave attenuation, shape and timing—Part 1: Mathematical tools.” *Journal of Hydraulic Research*, 46(3), 373–381.

Chaudhry, M. H. (1987). *Applied hydraulics transients*, 2nd edition. Van Nostrand Reinhold, New York.

Covas, D., Ramos, H., and Betâmio de Almeida, A. (2005). “Standing wave difference method for leak detection in pipeline systems.” *Journal of Hydraulic Engineering*, 131(12), 1106–1116.

Ferrante, M., and Brunone, B. (2002). “Pipe system diagnosis and leak detection by unsteady-state tests. 2. Wavelet analysis.” *Advances in Water Resources*, 26, 107–116.

Fuentes, D.A.A., Galvis, L.F.C., and Valderrama, J.G.S. (2006). “Hydraulic transients with genetic algorithms used for leakage detection in real water distribution networks.” *Proceedings of the 2006 Pipeline Division Specialty Conference—Pipelines 2006: Service to the Owner Fuentes*, Vol. 211 40854, 15.

Hachem, F., and Schleiss, A. (2010). “A review of wave celerity in frictionless and axisymmetrical steel-lined pressure tunnels.” *Journal of Fluids and Structures*, accepted for publication, 2010.

Halliwell, A.R. (1963). “Velocity of a Waterhammer Wave in an Elastic Pipe.” *Journal of the Hydraulics Division*, ASCE, 89, No. HY4, 1–21.

Lang, F.H. (1987). *Correlation Techniques*. D. Van Nostrand, N J.

Liggett, J.A., and Pudar, R.S. (1992). “Leaks in pipe networks.” *Journal of Hydraulic Engineering*, 118(7), 1031–1046.

Mallat, S.G. (1990). *A Wavelet Tour of Signal Processing*. Academic Press, San Diego, CA.

Misiunas, D., Vitkovsky, J., Olsson, G., Simpson, A., and Lambert, M. (2005). “Pipeline break detection using pressure transient monitoring.” *Journal of Water Resources Planning and Management*, 131(4), 316–325.

Parmakian, J. (1963). *Waterhammer analysis*. Dover, New York.

Streeter, V.L. (1963). “Discussion of Halliwell A.R. 1963 Velocity of a water-hammer wave in an elastic pipe”. *Journal of the Hydraulics Division*, ASCE, 89, No. HY6, 295–296.

Timoshenko, S.P., and Goodie, J.N. (1970). *Theory of elasticity*. McGraw-Hill, New York.

Wylie, E.B., Suo, L., and Streeter, V.L. (1993). *Fluid Transients in Systems*, facsimile edition. Prentice Hall, Englewood Cliffs, NJ.

List of Figures

List of Tables

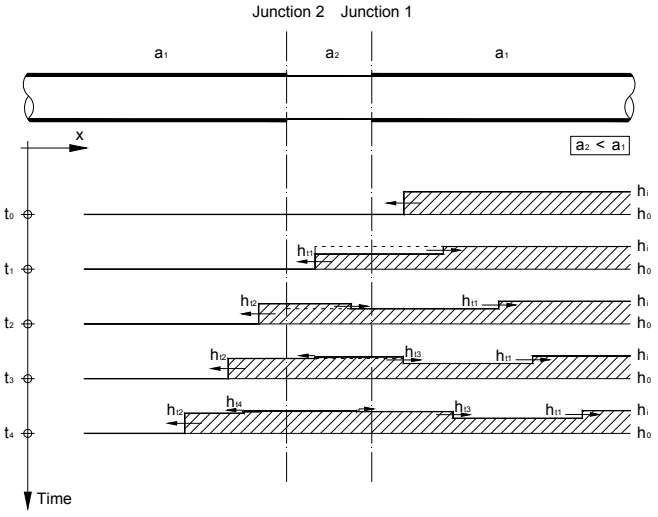

Fig. 1.

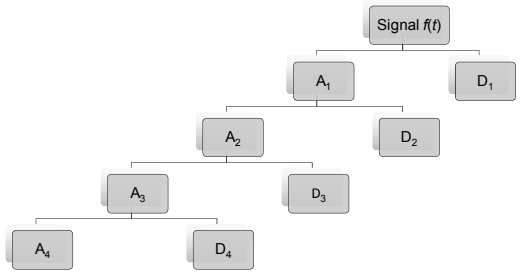

Fig. 2.

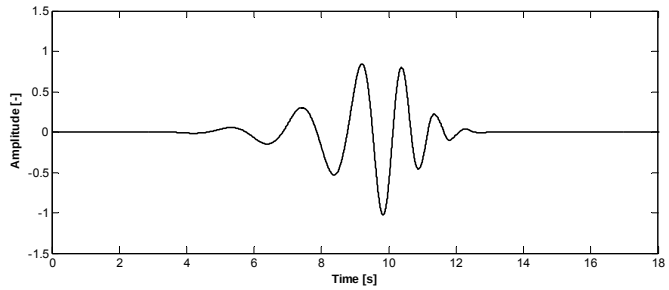

Fig. 3.

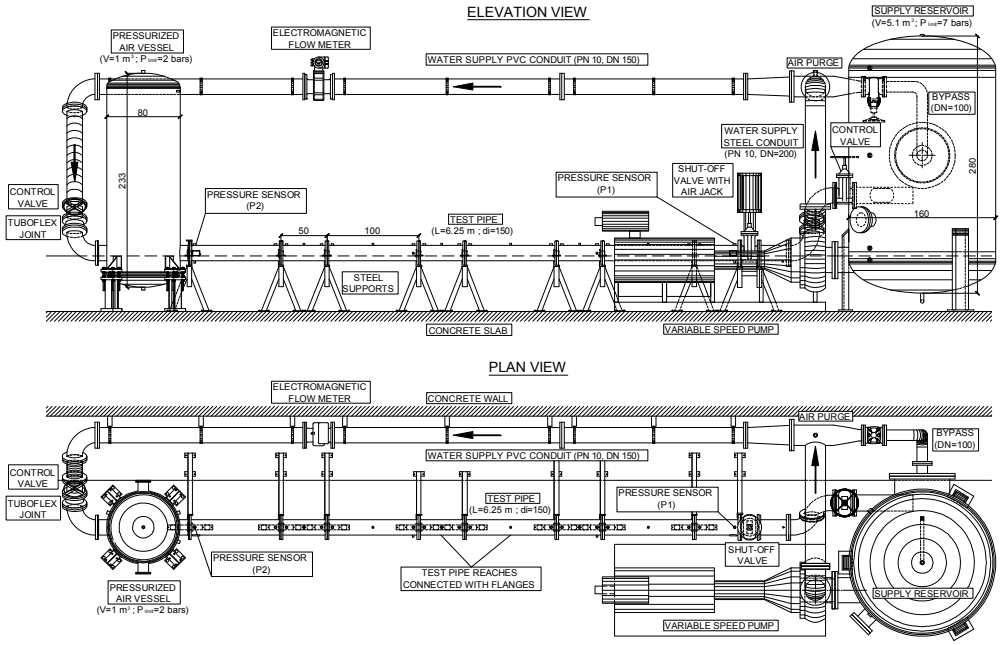
ELEVATION VIEW
PRESSURIZED AIR VESSEL (V=1 m³ ; P max=2 bars)
ELECTROMAGNETIC FLOW METER
WATER SUPPLY PVC CONDUIT (PN 10, DN 150)
SUPPLY RESERVOIR (V=5.1 m³ ; P max=7 bars)
AIR PURGE
BYPASS (DN=100)
WATER SUPPLY STEEL CONDUIT (PN 10, DN=200)
CONTROL VALVE
SHUT-OFF VALVE WITH AIR JACK
PRESSURE SENSOR (P1)
PRESSURE SENSOR (P2)
CONTROL VALVE
TUBOFLEX JOINT
TEST PIPE (L=6.25 m ; di=150)
STEEL SUPPORTS
CONCRETE SLAB
VARIABLE SPEED PUMP
80
233
50
100
160
280
PLAN VIEW
ELECTROMAGNETIC FLOW METER
CONCRETE WALL
AIR PURGE
BYPASS (DN=100)
WATER SUPPLY PVC CONDUIT (PN 10, DN 150)
CONTROL VALVE
TUBOFLEX JOINT
TEST PIPE (L=6.25 m ; di=150)
PRESSURE SENSOR (P1)
SHUT-OFF VALVE
PRESSURE SENSOR (P2)
TEST PIPE REACHES CONNECTED WITH FLANGES
PRESSURIZED AIR VESSEL (V=1 m³ ; P max=2 bars)
SUPPLY RESERVOIR
VARIABLE SPEED PUMP

Fig. 4.

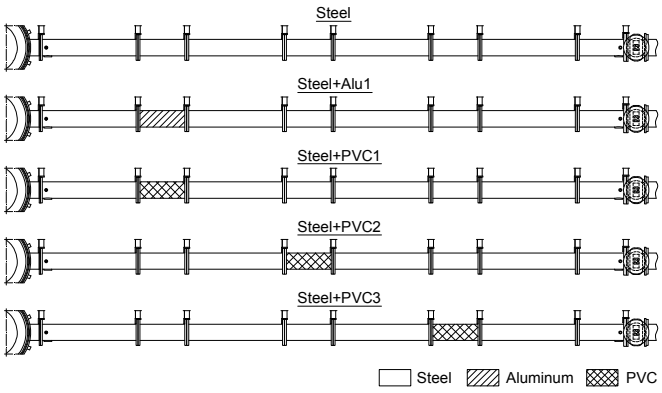
Steel
Steel+Alu1
Steel+PVC1
Steel+PVC2
Steel+PVC3
Steel
Aluminum
PVC

Fig. 5.

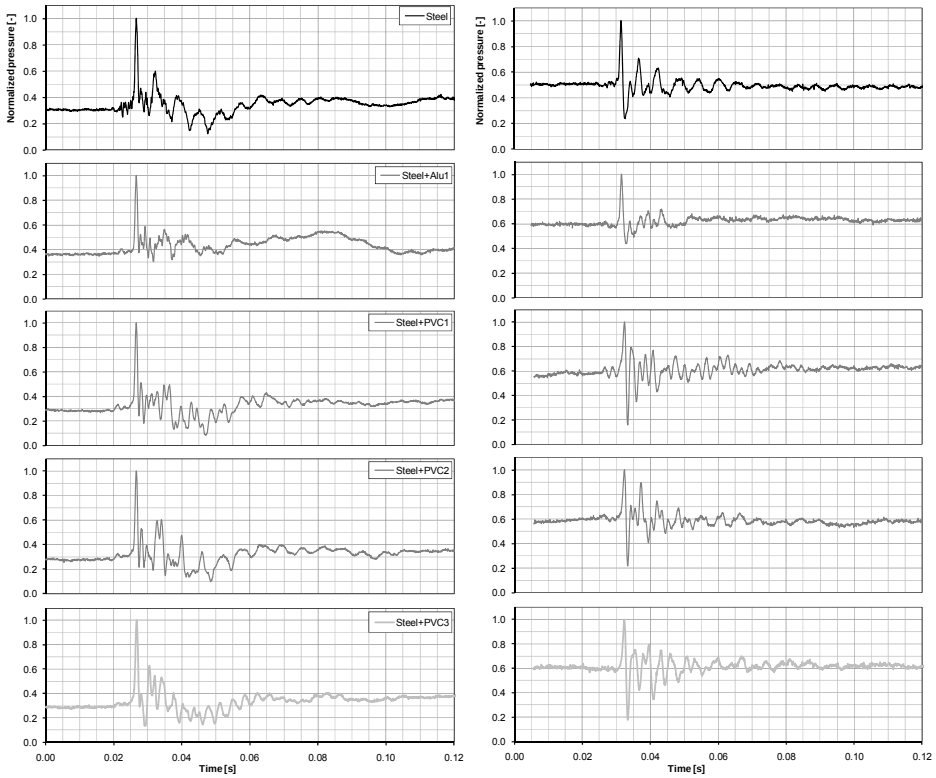
Steel
Steel+Alu1
Steel+PVC1
Steel+PVC2
Steel+PVC3
Normalized pressure [-]
Time [s]
(a)
(b)

Fig. 6.

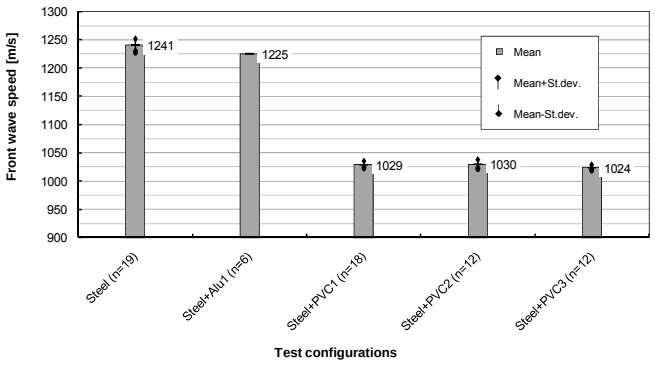
Front wave speed [m/s]
Mean
Mean+St.dev.
Mean-St.dev.
1241
1225
1029
1030
1024
Steel (n=19)
Steel+Alu1 (n=6)
Steel+PVC1 (n=18)
Steel+PVC2 (n=12)
Steel+PVC3 (n=12)
Test configurations

Fig. 7.

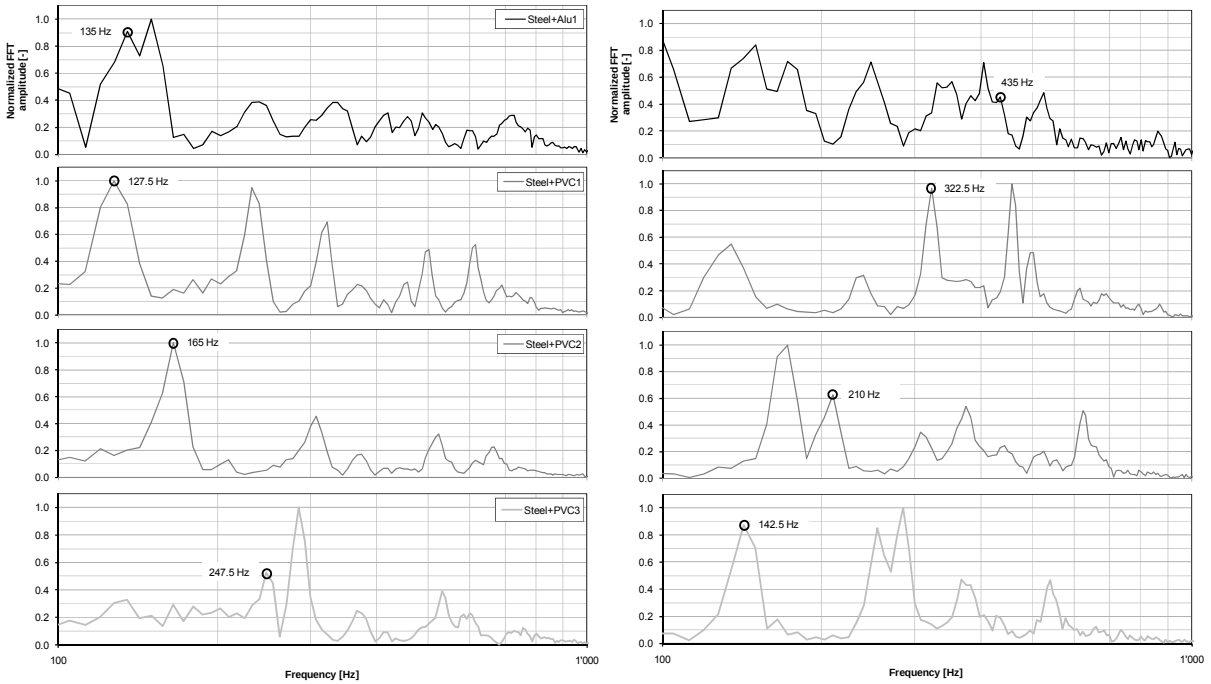
Steel+Alu1
135 Hz
Steel+PVC1
127.5 Hz
Steel+PVC2
165 Hz
Steel+PVC3
247.5 Hz
Normalized FFT amplitude [-]
Frequency [Hz]
100
1'000
435 Hz
322.5 Hz
210 Hz
142.5 Hz

(a) **(b)**

Fig. 8.

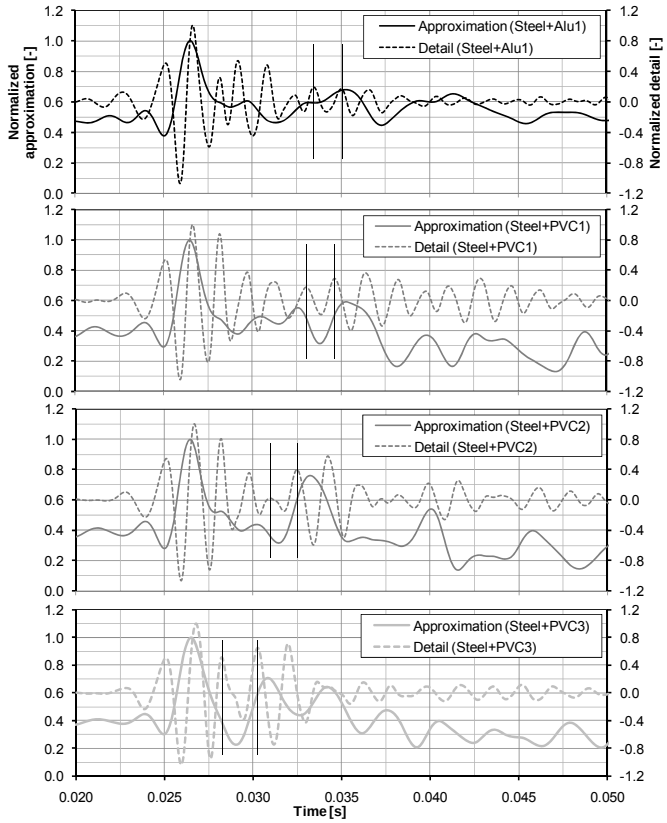
Approximation (Steel+Alu1)
Detail (Steel+Alu1)
Approximation (Steel+PVC1)
Detail (Steel+PVC1)
Approximation (Steel+PVC2)
Detail (Steel+PVC2)
Approximation (Steel+PVC3)
Detail (Steel+PVC3)
Normalized approximation [-]
Normalized detail [-]
Time [s]

Fig. 9.

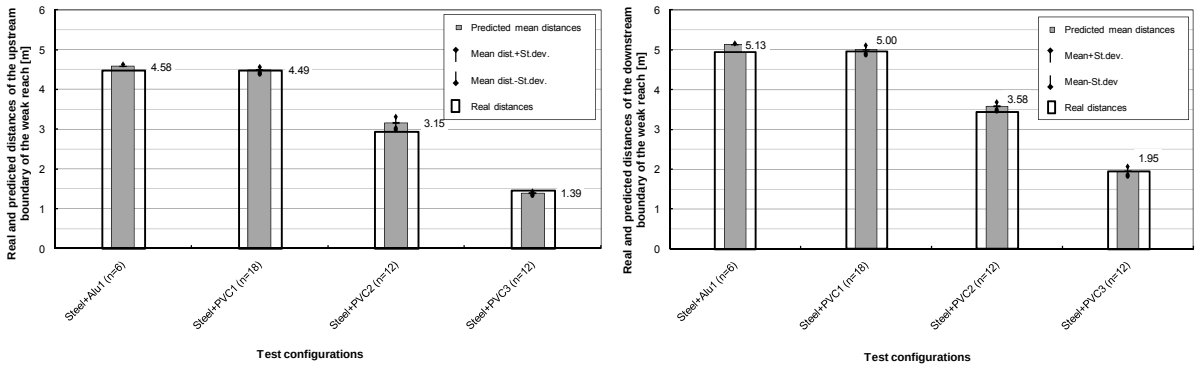

(a) **(b)**

Fig. 10.

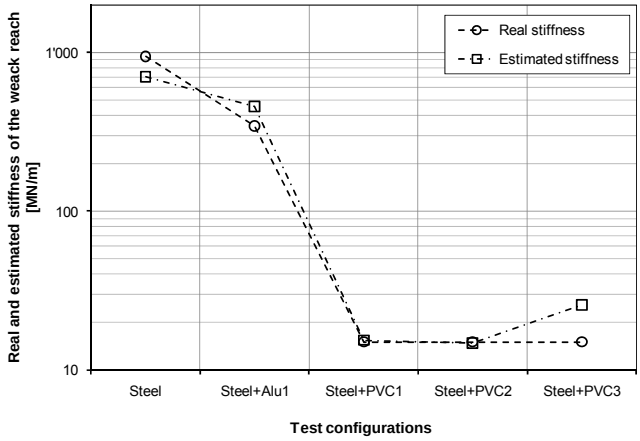

Fig. 11.

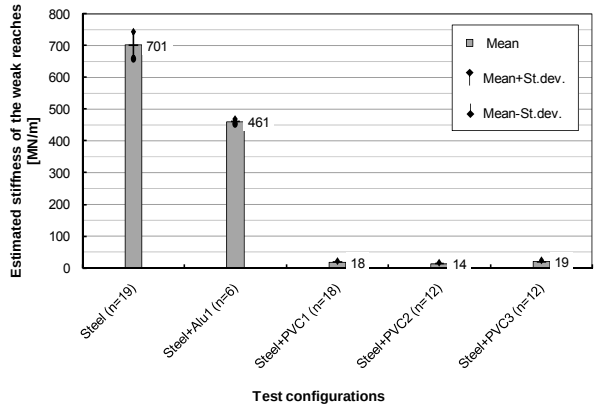

Fig. 12.

PHYSICAL TESTS FOR ESTIMATING THE WATER-HAMMER WAVE SPEED IN PIPES AND TUNNELS WITH LOCAL WEAK WALL STIFFNESS

F.E. Hachem, M.ASCE[1] and A.J. Schleiss[2]

[1]Research assistant and [2]Professor and Director, Laboratory of Hydraulic Constructions (LCH), Ecole Polytechnique Fédérale de Lausanne (EPFL), Station 18, 1015 Lausanne, Switzerland.

Phone: +41 (21) 693 24 01, Fax: +41 (21) 693 22 64.

fadi.hachem@epfl.ch, anton.schleiss@epfl.ch

ABSTRACT

A new non-intrusive monitoring technique to detect a local drop of wall stiffness of steel-lined pressure shafts and tunnels by processing the water-hammer wave measurements is presented. This technique is developed in the framework of a so called *HydroNet* project (Modern methodologies for the design, manufacturing and operation of pumped-storage plants). The complex multilayer structure of the pressure tunnels and shafts which is composed of steel, concrete, and rock, is studied experimentally by a steel pipe divided longitudinally into many reaches. The simulation of the local drop in the wall stiffness is produced by changing a steel reach with a more flexible material like Aluminum or PVC. The water-hammer waves are generated inside the test pipe by closing a valve located at its downstream end. The dynamic water pressure signals are acquired at two different locations at both end of the pipe. The experiments confirmed that the presence and severity of a weak reach can be detected by the analysis of these water-hammer pressure recordings. As signal processing procedure to estimate the water-hammer wave speed between the two pressure sensors, the wavelet decomposition method is used associated with the floating root mean square and the cross-correlation techniques. In the test pipe configuration with an Aluminum reach of 50 cm length, the mean wave speed is 3.5% lower than for the pipe configuration where all reaches are made of steel. When the Aluminum reach is replaced by PVC, the drop of the wave speed becomes about 18.5% compared to the steel reference case.

Keywords: Water-hammer wave speed; Pipe wall stiffness; Steel-lined pressure tunnels and shafts; Wavelet decomposition; Correlation technique; Transient pressure signals; Non-intrusive monitoring.

1 INTRODUCTION

The water-hammer phenomenon in pressurized waterways has been noticed and studied long time ago [1, 2 and 3]. In the past, the safety margin for water-hammer dynamic loads in steel-lined pressure tunnels and shafts of hydropower plants was considered as sufficient. Actually, the high peak energy demands have put these existing structures to crude test with relatively high water-hammer overpressures induced by fast valve opening and closing of the pumps and turbines. For this reason and for others related to the aging of steel liners and to the deterioration of the backfill concrete and the rock mass surrounding the liner, non-intrusive monitoring and control methods for existing steel-lined pressure shafts and tunnels need to be enhanced [4].

Due to the Fluid-Structure Interaction, the water-hammer propagation mode is influenced by the elastic properties and stiffness of the liner [5, 6]. This physical interaction is used to develop a new monitoring method to detect, in real time and without dewatering and service interruption, the presence and location of a drop of wall stiffness of these underground waterways. The monitoring method is based on processing water-hammer pressure recordings acquired at the both accessible ends of the liner.

In this paper, the multilayer system (steel-concrete-rock) of the pressurized shafts and tunnels is considered to behave axisymmetrically under internal loads. It is physically modeled in laboratory by one layer system of the test pipe wall. Thus, a steel pipe divided into several reaches is used where it is possible to switch a steel reach with another weaker one made of Aluminum or PVC materials. As long as the search for longitudinal stiffness heterogeneity is concerned, different geometric configurations of the test pipe are examined by changing systematically the position of the weak reaches.

2 EXPERIMENTAL SET-UP

2.1 Description

The experimental facility is a close hydraulic loop designed to produce water-hammer transients inside a multi-reach steel test pipe of 6 m length and 150 mm of internal diameter. It’s divided

longitudinally into several reaches of 0.5 m and 1.0 m length connected together with flanges (Figure 1a). These latter are used to fix rigidly the test pipe to the concrete slab and wall of the laboratory in order to minimize the axial and transversal movements during water-hammer events. The local change in the wall stiffness of the test pipe is produced by replacing one or several steel reaches by Aluminum or PVC materials (Figure 1b). To detect the presence of these ‘’weak reaches’’, water-hammer pressure recordings *P1* and *P2* at the both ends of the pipe are assessed.

The water supply is provided by a reservoir having a volume of 5 m^3, a variable speed pump and a conduit of 10 m length equipped with an electromagnetic flow meter to measure the steady state flow. A first control and security valve followed by an elastic deformable joint (TUBOFLEX) are located at the downstream end of the supply conduit. A pressurized air vessel protects the entire supply system from water-hammer overpressures.

The downstream end of the test pipe is equipped with a shut-off valve to generate the transient events. It is followed by a purge valve, an elastic TUBOFLEX joint and a second control valve located at the entrance of the supply reservoir. The closure of the shut-off valve is carried out automatically using an air jack with an input and output electro-valves. The volume and pressure of the needed air to activate the jack are provided by an air compressor with a constant pressure of 10 bars. The opened and closed positions of the shut-off valve are detected by two diffuse sensors with an infrared beam.

The data acquisition system is composed of: (i) two pressure transducers (HKM-375M-7-BAR-A, Kulite) with a maximum pressure of 7 bars and an accuracy of 0.5 %, (ii) a NI-USB-6259 acquisition card M series with a maximum of 32 analogue input channels and 2 analogue output channels, and (iii) a notebook computer connected to the acquisition card by a USB cable. The sampling frequency is fixed to 15 KHz. LabView 8.6, Diadem 11.0, and MATLAB 7.7 software are used for acquiring, controlling and processing the experimental data.

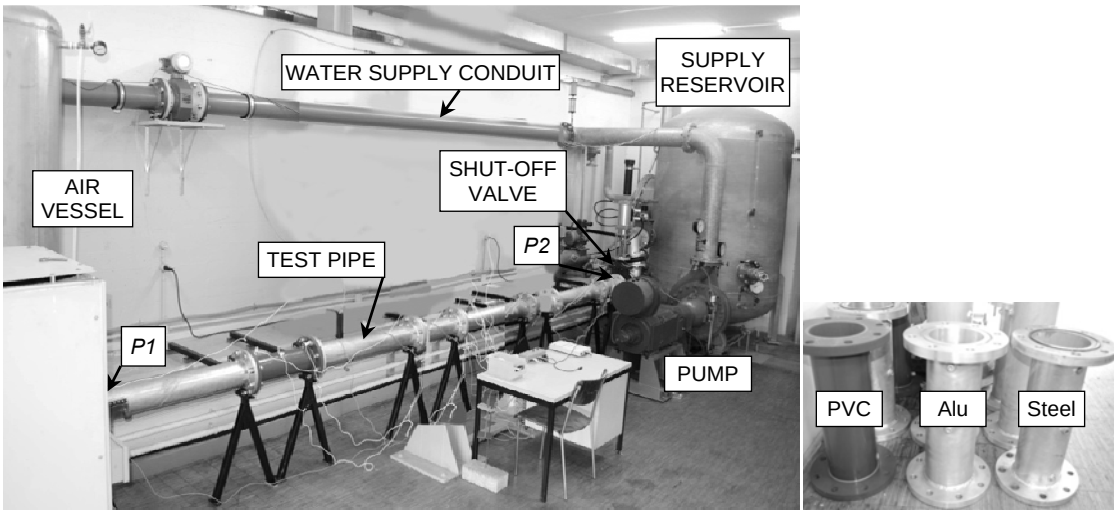

(a) (b)

Figure 1: a) Global view of the experimental facility, b) PVC, Aluminum, and steel pipe reaches of 0.5 m length each.

2.2 Test pipe configurations

The five pipe configurations noted *C1* to *C5*, shown schematically in Figure 2, have been examined. The same initial steady flow conditions around 58.2 l/s, the same mean water pressure at the entrance of the test pipe of 0.2 bars, and the same mean closure time of the shut-off valve of 0.235 second were all maintained during tests. A total of 54 tests have been carried out including 12 tests on each configuration from *C1* to *C4* and 6 tests on *C5*. In order to determine the signal-to-noise ratio, many tests involving the closure of the shut-off valve with no flow inside the test pipe have been done.

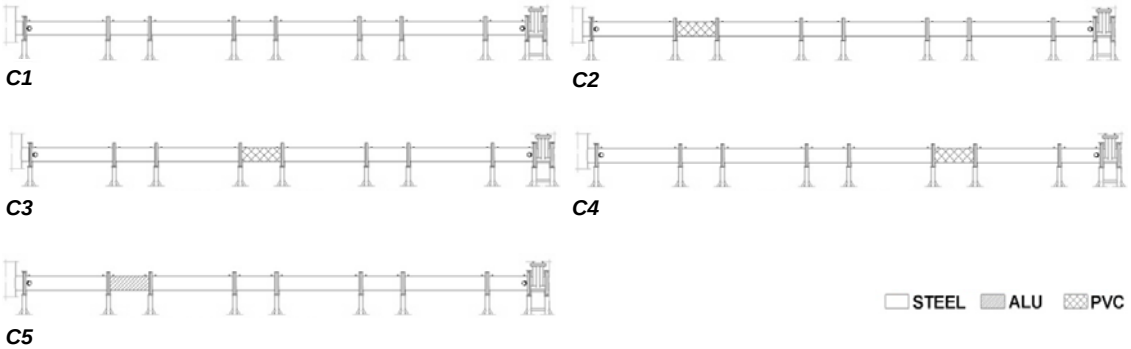

Figure 2: The different configurations of the test pipe using Steel, Aluminum, and PVC reaches of 0.5 m length.

3 DATA ANALYSIS

3.1 Pressure recordings

The water pressure signals *P1* and *P2* at both ends of the test pipe were collected. The data acquisition and storage procedure starts before 2.9 seconds from the beginning of the shut-off valve and ends 6 seconds after. Figure 3a shows a typical time history of the pressure signal *P2* between 2.8 and 3.4 seconds. The first part of the signal located at the beginning of the valve closure maneuver is affected by an external pressure excitation caused by the impact of the air inside the jack of the valve. This part of the signal, about 0.06 second long, has been processed to detect the existence, location, and severity of the local drop of the wall stiffness of the test pipe [7, 8]. The tests under no flow conditions reveal that the core of the valve induces noise around 0.08 second before the total closure of the valve. This leaves a signal window of about 0.08 second in which the progressive stoppage of the flow by the valve core creates water-hammer pulsations inside the test pipe. This part of the signal shown in Figure 3b is accessed in this paper. The same cutting window is used to extract the *P1* signal. The last part of the pressure recording located after the end of the valve closure maneuver, shows transients with low frequencies caused by the mass oscillation phenomenon between the air vessel and the supply reservoir.

The acquired signals during water-hammer episodes are disturbed by noises from the supply pump and from friction between the core and the cover of the shut-off valve.

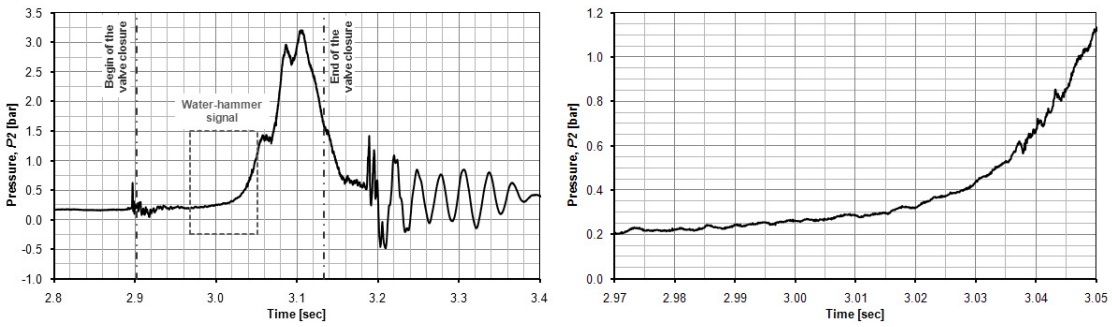

(a) (b)

Figure 3: a) Typical pressure transient history at sensor *P2*, b) Zoom on the water-hammer pressure signal inside the dashed square of Figure 3a.

3.2 Data analysis

3.2.1 Signal decomposition

The processing of pressure data *P1* and *P2* is done using the wavelet technique [9]. The main advantages afforded by wavelets are: (i) the ability to perform local analysis revealing some aspects of data that other signal analysis miss, and (ii) the de-noising of signal without appreciable degradation. A wavelet is nothing than a waveform of effectively limited duration that has average value of zero. Similar to the Fourier transform which uses sine waves of various frequencies as basis, wavelet analysis is the breaking up of the signal into shifted and scaled versions of the original (or mother) wavelet [10,11].

The wavelet transform provides coefficients, $\widehat{p}(\lambda,u)$, that represent a sort of correlation degree between the wavelet, scaled to λ, and the section of the signal at time u. The wavelet coefficient expression for a signal $p(t)$ is written as follows:

$$\widehat{p}(\lambda,u) = \frac{1}{\sqrt{\lambda}} \int p(t)\ \psi\left(\frac{t-u}{\lambda}\right) dt \qquad (1)$$

where, λ and u are the dilation or scale, and the translation parameter, respectively. $\Psi(\lambda,u)$ are the transform basis functions or wavelets.

The wavelet coefficients and basis functions are then used to decompose the signal into a hierarchical set of so called approximations and details. At each decomposition level j, the signal is passed through a pair of high-pass and low-pass filters. The details coefficients are the result of the former filter while the approximation coefficients are those obtained from the latter one. The detail coefficient D_j at level j is given by the following equation:

$$D_j(t) = \sum_{k\in\mathbb{Z}} \widehat{p}(j,k) \cdot \frac{1}{\sqrt{j}} \psi\left(\frac{t-k}{j}\right) \qquad (2)$$

where, $\lambda = 2^j$ and $u = k \cdot 2^j$. The parameter k is called the time index.

After J levels of decomposition, the original pressure signal $p(t)$ can be expressed as:

$$p(t) = A_J(t) + \sum_{j=1}^{J} D_j(t) \qquad (3)$$

where, the approximation coefficients A_J is given by:

$$A_J(t) = \sum_{j>J} D_j(t) \tag{4}$$

The wavelet decomposition up to level 7 of the water-hammer signals *P1* and *P2* was carried out using the *Daubechies* (*db10*) mother wavelet. A new pressure signal was constructed from each pressure record by adding its details from *D4* to *D7*. This construction preserves the pressure fluctuations caused by the water-hammer wave in a band-pass frequency of lower and higher limits of 72 and 486 Hz, respectively. The new constructed signal *S*(*P2*) of the pressure history shown in Figure 3b is given in Figure 4b. In Figure 4a, the constructed signal *S*(*P1*) in the same time interval and for the same pipe configuration is shown. The same signal decomposition and construction procedures were carried out for all the 54 water-hammer tests and for the shut-off valve tests with no flow condition. A sample of the steady-state pressure signal for each water-hammer test was also analyzed in order to determine the noise level caused by the pump. The signal-to-noise ratio is then calculated according to the following equation:

$$SNR = \left(\frac{A_{wh}}{A_{St-noise} + A_{Vc-noise}} \right)^2 \tag{5}$$

where, A_{wh}, $A_{St\text{-}noise}$, and $A_{Vc\text{-}noise}$ are the root mean squares of the water-hammer signal, the noise at the steady-state pressure, and the noise during the valve closure, respectively. The mean SNR values determined as the average of the SNRs of the constructed signals for each pipe configuration varies between 1.6 and 3.2.

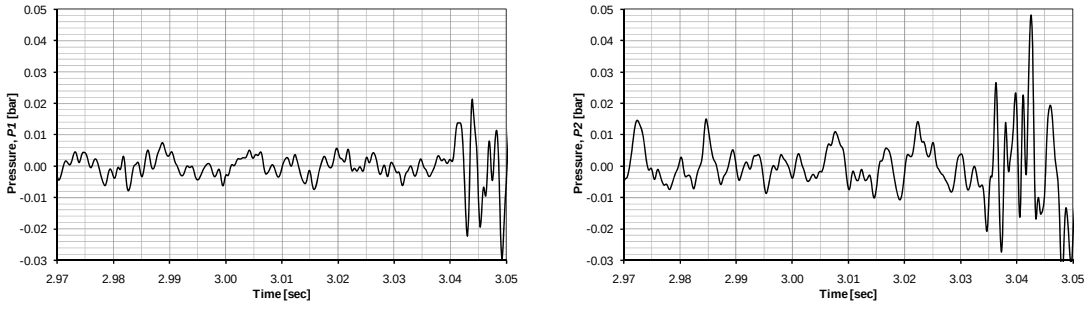

(a) (b)

Figure 4: Pressure signals constructed from the summation of details D4, D5, D6, and D7. a) The signal *S*(*P1*) obtained from the decomposition of *P1*, b) The signal *S*(*P2*) obtained from the decomposition of *P2*.

3.2.2 Estimation of the water-hammer wave speed

The estimation of the water-hammer wave speed inside the test pipe is done using the following formula:

$$a = \frac{2 \cdot l_{P1,P2}}{t_{P1,P2}} \tag{6}$$

where, $l_{p1,p2}$ is the known distance of 5.88 m separating the two pressure sensors *P1* and *P2* and $t_{p1,p2}$ is the unknown travel time of the first significant incident wave propagating from *P2* towards *P1*.

In [7], it was possible to follow the propagation of the first wave front generated by an exterior impulse near sensor *P2* and to determine the travel time between the two pressure sensors. In the case of water-hammer pulses induced by the closure of the valve, many pressure fluctuations are generated inside the test pipe. Therefore, there is no clear wave front that can be easily defined and followed. The energy approach has to be used to distinguish the significant part of the signal from others having low energy. The selected part is a sort of ''pressure signature'' that has an enough amount of energy to interact with the test pipe's wall. It is taken from the *S*(*P2*) and followed throughout the test pipe.

The floating root mean square (RMS) and the singular value decomposition (SVD) methods [12, 13] are two approaches that can be used to evaluate the energy content of the signal. The RMS method, used in this paper, is more simple and direct than the SVD method. The RMS uses the following simple formula to calculate the floating root mean square RMS_j, of the discrete signal pressure values p_i:

$$RMS_j = \sqrt{\frac{1}{N} \sum_{i=j}^{j+N-1} p_i^2} \tag{7}$$

where, N is a constant parameter equal to the number of pressure values inside a one period interval. It was taken equal to the following high-frequency value: $N = 1/486 \cdot 15000 \approx 30$. In Figure 5a, the *RMS* results of the signal *S*(*P2*) presented in Figure 4b are shown. A relative important positive shift in the *RMS* values is observed near 3.035 seconds indicating a significant input of energy inside the test pipe. By taking a threshold line around *RMS*=0.01bar,

a *S*(*P2*) signature is defined as being the signal portion bounded by the times of the two minimum peaks of the first RMS lobe that passes above the energy threshold line. The extracted *S*(*P2*) signature is shown in Figure 5b.

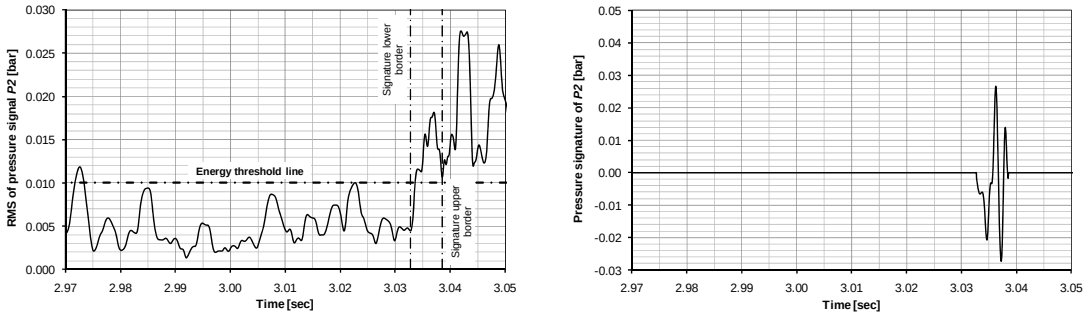

(a) (b)

Figure 5: a) The floating root mean square of the *S(P2*) signal shown in Figure 4b with the upper and lower signature time borders, b) The *S*(*P2*) pressure signature taken from pressure records of Figure 4b.

The procedure for estimating the water-hammer wave speed ends by cross-correlating the signature of *S*(*P2*) with the pressure signal *S*(*P1*). It is a measure of similarity of these signals as a function of a time-lag applied to one of them. For discrete functions, the cross-correlation is defined as follows [14]:

$$\big(S(P1) * S(P2)\big)[n] = \sum_{m=l}^{q} S(P1)^{*}[m] \cdot S(P2)\ [n+m] \tag{8}$$

where, *S*(*P1)** is the complex conjugate of *S*(*P1*), *l* and *q* are the lower and upper limits of the signal time interval, respectively, and *n* and *m* are two positive integers. The cross-correlation results of the signals shown in Figures 4a and 5b over a time interval of 0.01 second are presented in Figure 6. The estimating travel time of the water-hammer wave between the two pressure sensors corresponds to the time-lag at a positive peak of the cross-correlation curve. This positive peak has to be identified between two time borders defined as being the ratio of the distance seperating the pressure sensors and the two logical wave speed values of 1400 and 900 m/s, respectively. In all the pipe configurations, these time limits are 0.00420 and 0.00653 second. From Figure 6, the peak time taken inside this time interval is equal to 0.005732 second. Using Eq. (6), the wave speed velocity for the herein treated test involving the pipe configuration *C2* can be deduced. It is equal to 1025.8 m/s.

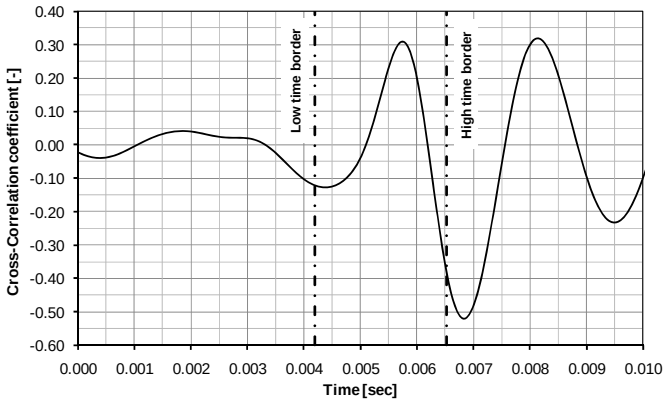

Figure 6: The normalized cross-correlation of the signature of the *S*(*P2*) and *S*(*P1*) signals.

The wave speed calculation procedure was applied to all the experimental tests of the five pipe configurations *C1* to *C5*. The estimated values of the water-hammer wave speed are shown in Figure 7 with their means and standard deviations evaluated for each pipe configuration. The change of the means of the wave speed indicates the presence of a local weak stiffness in the pipe wall. The relative differences between these means are proportional to the severity of the stiffness change.

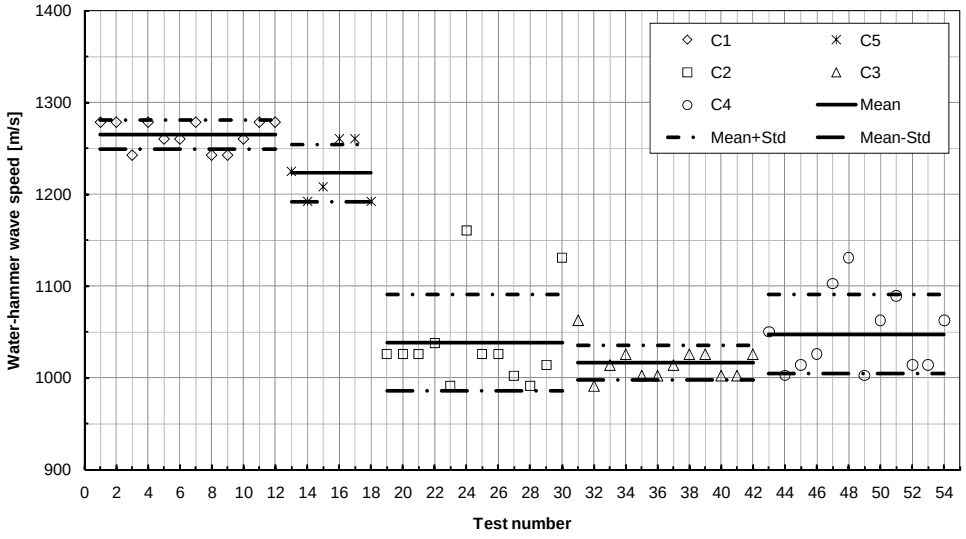

Figure 7: The water-hammer wave speed estimated by the new calculation procedure for all the 54 tests carried out on the five pipe configurations.

4 CONCLUSION

In this paper, an experimental physical facility generating water-hammer transients was described in detail. A series of physical experiments were carried out on five different pipe configurations built by replacing a steel pipe reach of 0.5 m length by Aluminum and PVC wall materials.

A new calculation procedure was presented to determine the water-hammer wave speed inside the test pipe using two pressure sensors at the both ends of the pipe. This procedure is based on filtering and decomposing of the pressure signals using wavelets analysis followed by energy and cross-correlation analyses. The results have shown that the computed wave speed is an indicator of the presence of local change of stiffness in the pipe's wall. This stiffness change was simulated in the test pipe by replacing a steel reach of 50 cm length with Aluminum and PVC materials. When an Aluminum reach is used, the wave speed is slower by 3.5% compared to the configuration where all reaches are in steel. The use of a PVC reach induces a wave speed drop of about 18.5% relative to the steel case.

In this ongoing research, more analyses and laboratory tests with other test pipe configurations still to be done. They will allow to validate the calculation procedure described in this paper and to create a method to estimate the position and severity of weak reaches. In-situ dynamic pressure measurements at both ends of a pressure shaft of a pumped-storage power plant will also be carried out. They will feed us with additional information about the steepness, energy and dissipation of water-hammer wave generated during start-up and shut-down of pumps and turbines. The influence of the water temperature, turbidity, and the captured air inside the shaft on the estimation of the wave speed will be also investigated.

ACKNOWLEDGMENTS

This study is part of the research project *HydroNet* (Modern methodologies for the design, manufacture and operation of pumped storage plants) funded by the *Swiss Competence Center Energy and Mobility* (CCEM-CH), the *Swiss Electric Research* and the *Swiss Office for Energy*.

REFERENCES

[1] Allievi, L., 1925. Theory of waterhammer. Translated by E.E. Halmos, printed by Riccardo Garoni, Rome, Italy.

[2] Parmakian, J., 1963. Waterhammer analysis. Dover Publications, Inc., New York.

[3] Wylie, E.B., Suo, L., Streeter, V.L., 1993. Fluid Transients in Systems. Prentice Hall, Fascimile Edition.

[4] Hachem, F.E., Schleiss, A.J., 2009. The design of steel-lined pressure tunnels and shafts. The International Journal on Hydropower & Dams 16(3), 142-151.

[5] Tijsseling, A.S., 1996. Fluid-Structure Interaction in Liquid-Filled Pipe Systems: A Review. Journal of Fluids and Structures 10, 109-146.

[6] Hachem, F.E., Schleiss, A.J., 2010. A review of wave celerity in frictionless and axisymmetrical steel-lined pressure tunnels. Journal of Fluids and Structures, accepted for publication, 2010.

[7] Hachem, F.E., Schleiss, A.J., 2010. Detection of local wall stiffness drops in pipes using steep pressure wave excitation and wavelet decomposition. Under reviewing process in the Journal of Hydraulic Engineering, ASCE.

[8] Hachem, F.E., Schleiss, A.J., 2010. Influence of local stiffness of conduits on water hammer propagation signal. Proceedings of the First European *IAHR* Congress, Edinburgh, 2010.

[9] Mallat S.G., 1992. Singularity detection and processing with wavelets. IEEE Trans Inf Theo (38), 617-43.

[10] Mallat, S.G., 1990. A Wavelet Tour of Signal Processing. San Diego, CA: Academic Press.

[11] The Mathworks, Inc., 2008. *MATLAB*, Natick, Mass. (www.mathworks.com).

[12] Trefethen, L.N.; Bau III, D., 1997. Numerical linear algebra. Society for Industrial and Applied Mathematics, Philadelphia. ISBN 978-0-89871-361-9.

[13] Yang, W.-X., Barry Hull, J., Seymour, M.D., 2006. Detecting the singularities in engineering signals. Journal of Materials Processing Technology 175, 439-445.

[14] Lang, F.H., 1987. Correlation Techniques. D. Van Nostrand Company, New Jersey.

Monitoring of steel-lined pressure shafts using water-hammer records and wavelet filtering and decomposition

F.H. Hachem[1] and A.J. Schleiss[1]
[1]Laboratory of Hydraulic Constructions (LCH)
Ecole Polytechnique Fédérale de Lausanne (EPFL)
Station 18, 1015 Lausanne
SWITZERLAND
E-mail: fadi.hachem@epfl.ch

Abstract: *The failure of steel liner of pressure shafts of hydropower plants can have catastrophic consequences. The partial or total loss of the liner support's rigidity is characterized by a local change of the hydro-acoustic properties and creates reflection boundaries for the water waves. This paper presents a new monitoring method for detecting and locating weak reaches by processing reflected water-hammer waves at the boundaries of the shaft. These water-hammers are generated experimentally by a shut-off valve installed at the downstream end of a test pipe. The weak reaches are modeled by replacing the steel of the pipe's wall with aluminum and PVC materials. Different test pipe configurations are created by changing the position of these reaches along the test pipe. The monitoring procedure uses the Fast Fourier Transform and wavelet decomposition techniques to estimate the incident-reflection travel time between the pressure sensors and the weak reaches boundaries.*

Keywords: *Steel-lined pressure tunnels and shafts, pipe wall stiffness, water-hammer, wavelet decomposition, weak reaches, wave reflection.*

1. INTRODUCTION

One of the multiple objectives of the so called *HydroNet* research project (Modern methodologies for the design, manufacturing and operation of pumped-storage plants) is the creation an enhancement of new non-intrusive monitoring methods for steel-lined pressure shafts and tunnels. The idea is to access records of the dynamic water pressure acquired during the water-hammer phenomena in purpose to identify the existence and location of a weak reach. This latter is generated by the local structural deterioration of the backfill concrete and/or the rock mass surrounding the liner. This reduces the overall wave speed and creates reflection boundaries for the incident pressure waves.

From a simple state-of-the-art review, it can be concluded that there is a large number of techniques that deal with another type of faults in pipelines such as leak detection (Ferrante & Brunone, 2002, Covas ***et*** al., 2005, Shamloo & Haghighi, 2009, Taghvaei ***et*** al., 2010, etc). In all these methods, the pressure wave speed is assumed to be a constant value throughout the pipeline length. No works or references were found for investigating the wave reflections coming from weak reaches with different hydro-acoustic parameters such as wave speed.

Under an axi-symmetrical behavior, the multilayer system (steel–concrete–rock) of the pressurized shaft can be modeled by one layer system of a steel test pipe which is divided into several reaches. The weak reach is simulated by exchanging the steel reach with an aluminum or PVC material. To detect the longitudinal stiffness heterogeneity, different geometric configurations of the steel test pipe were examined experimentally by changing systematically the position of an aluminum and PVC pipe reach of 50 cm length.

For the estimation of the wave speed and the prediction of the incident–reflection travel time between the weak reach boundaries and the pressure sensors, the Fast Fourier Transform, the cross-correlation technique and the wavelet filtering and decomposition methods were applied on the pressure data records at the both end of the test pipe.

2. THEORY

2.1. Water-hammer

When water flow in pressurized waterways (pipes, tunnels and shafts) is suddenly stopped, pressure waves, known as water-hammer, are generated according to the acoustic plane wave equation written as follows (Parmakian, 1963 and Bergant *et* al., 2008):

$$g\frac{\partial^2 h}{\partial x^2} - \frac{g}{a^2}\frac{\partial^2 h}{\partial t^2} = -f\frac{|v|}{D}\frac{\partial v}{\partial x} \qquad (1)$$

where, $h(x,t)$ is the piezometric head, $v(x,t)$ is the water flow velocity, t is the time, x is the longitudinal dimension, g is the acceleration due to gravity, a is the speed of sound in water or the pressure wave velocity, f is the Darcy–Weisbach friction factor and D is the internal diameter of the waterway. These waves travel along the waterway until they hit the borders (or junction) of a reach having different hydro-acoustic properties (different flow area and/or pressure wave velocity) from the rest of the waterway. At these boundaries, the waves are partly transmitted and partly reflected back towards the source. For steel-lined pressure tunnels, such a different hydro-acoustic reach may exist when a decrease of the wave speed appears due to a partial or total loss of the stiffness of the exterior support of the steel liner which is provided by the surrounding backfill concrete and rock mass. This reach with a wave speed lower than the rest of the tunnel is called ''weak reach'' throughout this paper.

Figure 1a shows a schematic profile of the test pipe with a weak reach having boundaries situated at distances x_1 and x_2 from the pressure sensor p2. This weak reach has a wave speed value a_2 lower than the rest of the test pipe (a_1). An incident pressure wave of magnitude (h_i-h_0) coming from the shut-off valve is divided into transmitted and reflected waves when crossing junction 1. For a uniform cross-section flow area and a frictionless pipe, the magnitude of the transmitted wave (h_{t1}-h_0) is given by (Wylie *et* al., 1993):

$$h_{t1} - h_0 = \frac{2}{1+\frac{a_1}{a_2}}\left(h_i - h_0\right) \qquad (2)$$

where, h_0, h_i and h_{t1} are the steady-state, incident and transmitted piezometric heads, respectively. The same phenomenon is reproduced when the pressure wave crosses the downstream end of the weak reach (junction 2). According to the direction of the first incident wave h_i, junctions 1 and 2 are called the upstream and downstream ends of the weak reach. Figures 1b and 1c show the normalized pressure records p1 and p2 obtained from a numerical calculation that uses the method of characteristic to solve Eq. (1) and Eq. (2) to evaluate the transmitted and reflected waves generated by the weak reach. In these numerical results, the pressure reflections from the boundaries of the weak reach can be easily identified by the pressure drop shown on Figure 1b. The value of the mean wave speed (a_{mean}) can be extracted by dividing the known distance separating the two pressure sensors by the predicted travel time (t_1-t_2). The incident-reflection travel times from the boundaries of the weak reach (t_{up} and t_{down}) can be clearly identified on Figure 1b. The weak reach can then be located by the two longitudinal coordinates x_1 and x_2 as follows:

$$x_{1,2} = a_{mean} \cdot t_{up,down} \qquad (3)$$

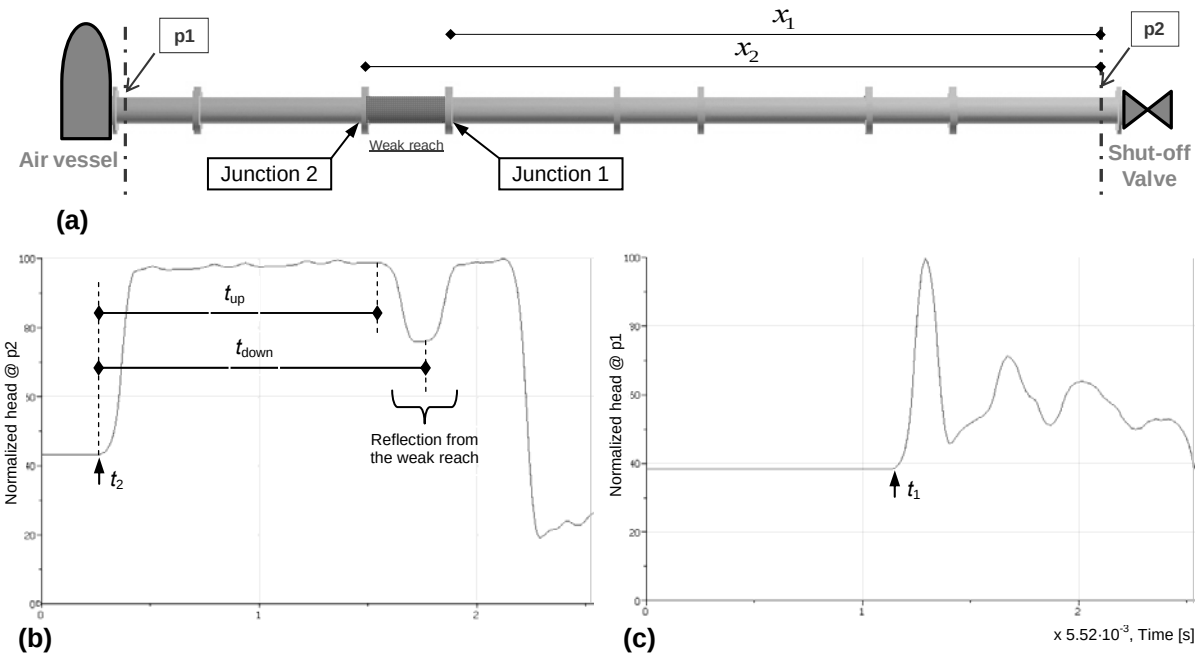

Figure 1 a) Schematic view of the test pipe, b) the normalized head at the pressure sensor p2 obtained from numerical calculation, and c) the normalized head at the pressure sensor p1 of the same numerical model

In plain strain conditions and considering the hypothesis of linear elasticity and small deformations, the wave velocity can be estimated by the following formula (Halliwell, 1963):

$$a = \sqrt{\frac{1}{\rho_w \left(\frac{1}{K_w} + \frac{2}{r_i} \cdot \frac{\mathrm{d}u_r^s(r)}{\mathrm{d}p} \right)}} \qquad (4)$$

in which $\frac{\mathrm{d}u_r^s(r)}{\mathrm{d}p}$ is the first derivative of the radial displacement of the steel liner u_r^s relative to the internal pressure p at the water–liner interface of radius r_i. The $\frac{\mathrm{d}u_r^s(r)}{\mathrm{d}p}$ ratio is nothing else than the inverse of the radial stiffness of the tunnel wall. By ignoring the presence of air in water, the velocity of a pressure wave travelling between two cross-sections of a tunnel will be affected by every change of the radial stiffness of its wall. In laboratory tests, the change of the wall stiffness is modeled by using pipe reaches having different ($E \cdot th$) values than the rest of the test pipe. E is the Young modulus and th is the thickness of the pipe wall.

2.2. Signal processing

The signal processing is needed to access the experimental data which are more difficult to analyse than the numerical results shown on Figures 1b and 1c. This is mainly due to the presence of noise and to the wave dispersion and attenuation phenomena.

The processing of experimental pressure signals p1 and p2 is done using the filtering and decomposition techniques of wavelets (Mallat, 1990). The main advantage provided by such a technique is its ability to de-noise the signal without significant degradation and distortion. Similar to the Fourier transform which uses sine waves of various frequencies as basis, wavelet analysis is the breaking up of the signal into shifted and scaled versions of the original (or mother) wavelet.

The wavelet transform provides coefficients $C(\lambda,u)$ that represent a sort of correlation degree between

the wavelet, scaled to λ, and the section of the signal at time u. The wavelet coefficient expression for a signal $p(t)$ can be written as follows:

$$C(\lambda,u) = \frac{1}{\sqrt{\lambda}} \int p(t)\ \psi\left(\frac{t-u}{\lambda}\right) dt \qquad (5)$$

where, λ and u are the dilation or scale, and the translation parameter, respectively. $\Psi(\lambda,u)$ are the transform basis functions or wavelets.

The wavelet coefficients and basis functions are then used to decompose the signal into a hierarchical set of so called approximations and details. At each decomposition level j, the signal is passed through a pair of high-pass and low-pass filters. The details coefficients are the result of the former filter while the approximation coefficients are those obtained from the latter one. The detail coefficient D_j at level j is given by the following equation (The Mathworks Inc., 2008):

$$D_j(t) = \sum_{k\in\mathbb{Z}} C(j,k) \cdot \frac{1}{\sqrt{j}} \psi\left(\frac{t-k}{j}\right) \qquad (6)$$

where, $\lambda = 2^j$ and $u = k \cdot 2^j$. The parameter k is called the time index.

After J levels of decomposition, the original pressure signal $p(t)$ can be expressed as:

$$p(t) = A_J(t) + \sum_{j=1}^{J} D_j(t) \qquad (7)$$

where, the approximation coefficients A_J is given by:

$$A_J(t) = \sum_{j>J} D_j(t) \qquad (8)$$

3. EXPERIMENTS

3.1. Description of the experimental set-up

The experimental facility is designed to produce water-hammer transients inside a multi-reach steel test pipe of 6 m length and 150 mm of internal diameter. It's divided longitudinally into several reaches of 0.5 m and 1.0 m length connected together with flanges (Figure 2a). These flanges are used to fix rigidly the test pipe to minimize its axial and transversal movements during water-hammer events. The local change in the wall stiffness of the test pipe is produced by replacing one or several steel reaches by aluminum or PVC materials. To detect the presence of these weak reaches, water-hammer pressure recordings p1 and p2 at the both ends of the pipe are acquired and analyzed.

The water supply is provided by a reservoir having a volume of 5 m^3, a variable speed pump and a conduit of 10 m length equipped with an electromagnetic flow meter to measure the steady state flow. A pressurized air vessel protects the entire supply system from water-hammer overpressures.

The downstream end of the test pipe is equipped with a shut-off valve to generate the transient events (Figure 2b). The closure of this valve is carried out automatically using an air jack with an input and output electro-valves. The volume and pressure of the needed air to activate the jack are provided by an air compressor with a constant pressure of 10 bars. The opened and closed positions of the shut-off valve are detected by two diffuse sensors with an infrared beam.

The data acquisition system is composed of: (i) two pressure transducers (HKM-375M-7-BAR-A, Kulite) with a maximum pressure of 7 bars and an accuracy of 0.5 %, (ii) a NI-USB-6259 acquisition card M series with a maximum of 32 analogue input channels and 2 analogue output channels, and

(iii) a notebook computer connected to the acquisition card by a USB cable. The sampling frequency is fixed to 20 KHz. LabView 8.6, Diadem 11.0, and MATLAB 7.7 software are used for acquiring, controlling and processing the experimental data.

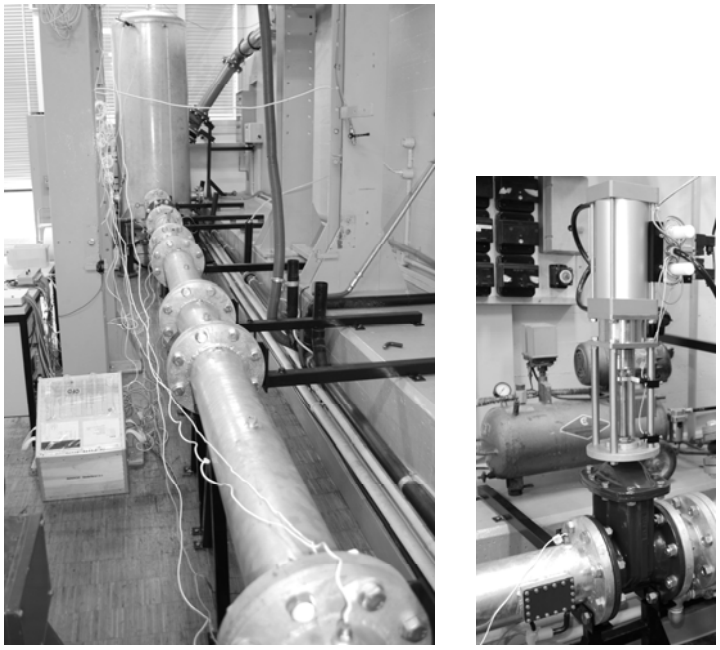

(a) **(b)**

Figure 2 a) The test pipe shown from the shut-off valve position, b) the shut-off valve with its air jack and the air compressor

3.2. Test pipe configurations

A total number of 84 tests have been carried out on the seven pipe configurations shown in Figure 3. The initial steady flow conditions, the air pressure in the compressor, and the mean pressure at the entrance of the test pipe were maintained constant for all tests. The basic configuration of the test pipe, named “Steel”, corresponds to steel pipe reaches of 100 and 50 cm length with 4.5 mm wall thickness. In the configuration “Steel+Alu1, 2, or 3,” the first, second or third 50 cm pipe reach (the first pipe reach is that nearest the air vessel) is replaced by an aluminum pipe with 5 mm wall thickness. In the configurations “Steel+PVC1, 2 or 3” the 50 cm long pipe reach is replaced by a 5 mm thick PVC pipe. For each test pipe configuration, 12 repetitive tests were carried out. The theoretical radial stiffness ($E \cdot th$) of steel, aluminum and PVC reaches are 945, 345 and 15 MN/m, respectively.

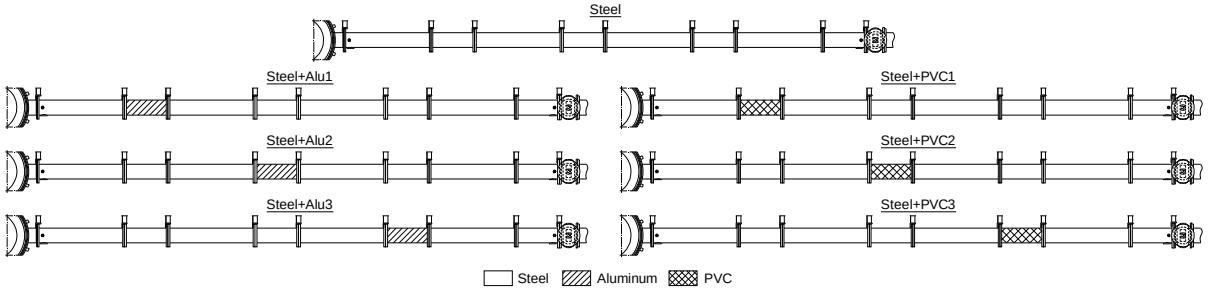

Figure 3 The seven different configurations of the test pipe

3.3. Test results and analysis

3.3.1. Estimation of the water-hammer wave speed

In Hachem & Schleiss (2010), it was possible to follow the propagation of the first wave front generated by an exterior impulse and to determine the travel time between the two pressure sensors. In the case of water-hammer pulses induced by the closure of the shut-off valve, many pressure fluctuations are generated inside the test pipe. Therefore, there is no clear wave front that can be easily identified and followed. The energy approach was used in Hachem & Schleiss (2011) to define a portion of the filtered and decomposed signal p2 that has a higher amount of energy from the precedent part of the signal. This selected portion was considered as a sort of ''pressure signature'' that has an enough amount of energy to interact with the test pipe's wall. It was then cross-correlated with the filtered and decomposed pressure signal p1 to estimate the water-hammer wave speed of the test pipe.

The same estimation procedure of the wave speed has been applied in this paper to all the test pipe configurations shown in Figure 3. The wavelet decomposition up to level 7 of the water-hammer signals p1 and p2 was carried out using the *Daubechies* (db10) mother wavelet. A new pressure signal was constructed from each pressure record by adding its details from D4 to D7. In Figure 4a, one record of the new constructed transient water pressure, p1, for the test pipe configuration "Steel+Alu1" is shown. Figure 4b depicts the constructed pressure signals p2 and its signature for the same test. In Figures 4c the root mean square (RMS) of the pressure signal p2 is shown and Figure 4d gives the cross-correlation results between p1 and the signature of p2. The estimated travel time between p1 and p2 is 0.00475 second and the mean wave speed of this test pipe configuration is 1237.9 m/s.

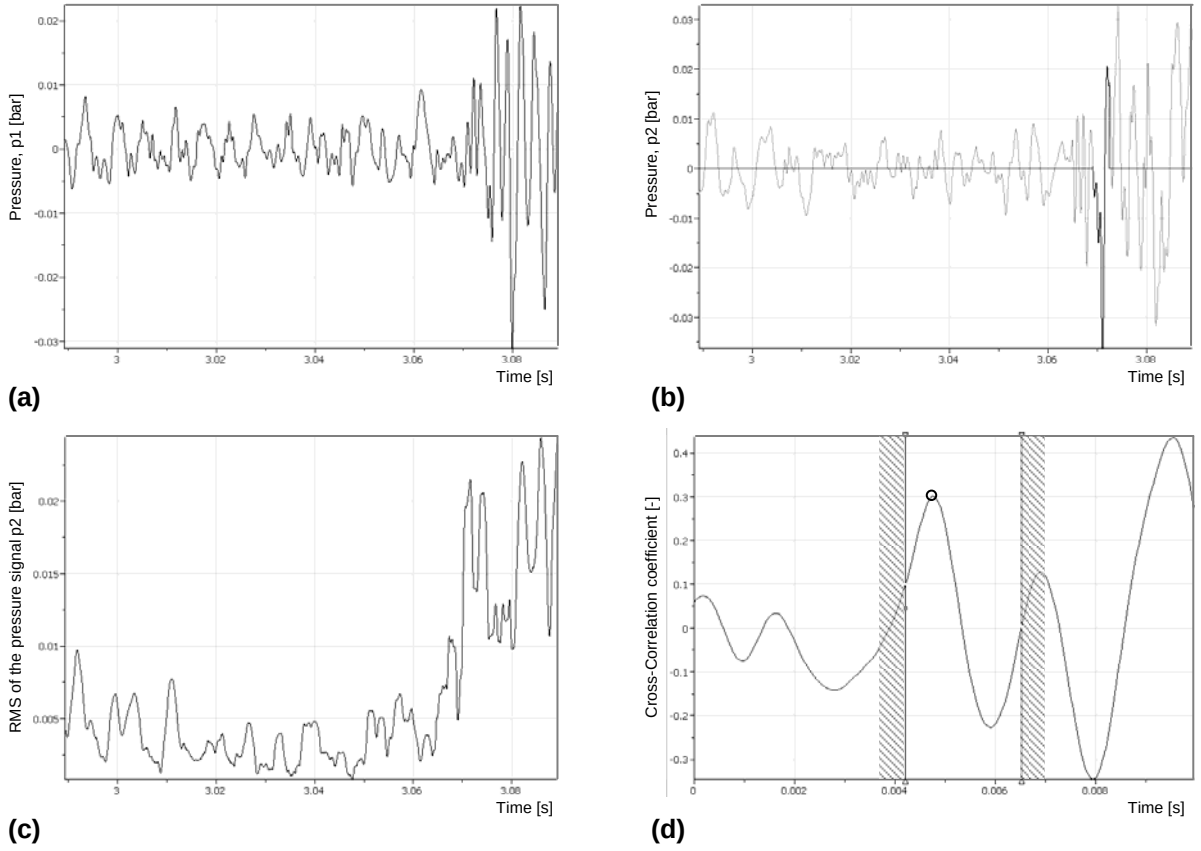

Figure 4 a) The constructed pressure signal p1, b) the constructed pressure signal p2 and its signature, c) the RMS of the constructed pressure p2, and c) the cross-correlation results between pressure p1 and the signature of pressure p2

The estimated values of the water-hammer wave speed for all the pipe configurations are shown in Figure 5 with their means and standard deviations evaluated for each pipe configuration. The change of the means of the wave speed indicates the presence of a local weak reach in the test pipe. The relative differences between these means are proportional to the severity of the stiffness change.

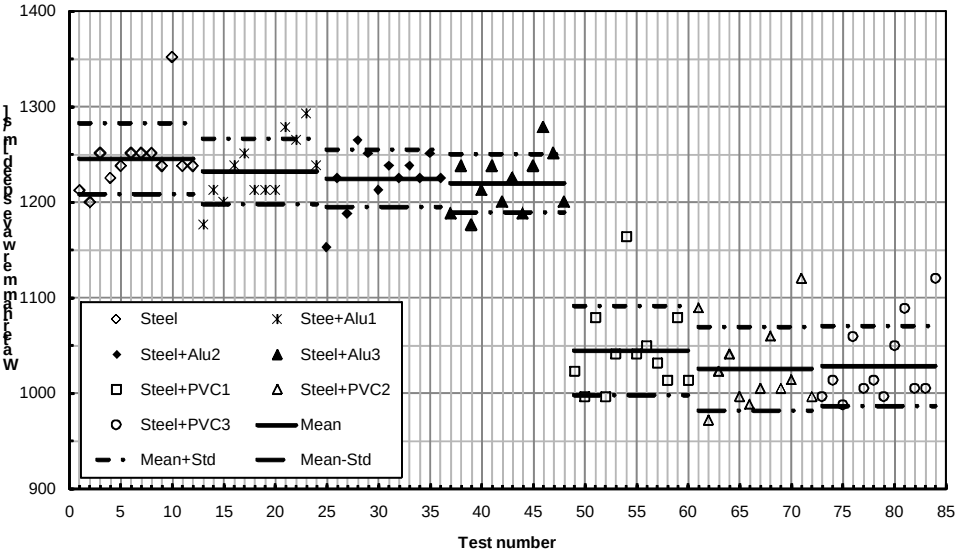

Figure 5 The estimated water-hammer wave speed, their means, and their standard deviations for the 84 tests carried out on the seven pipe configurations

3.3.2. Locating of the weak reach

The incident-reflection travel times, t_{up} and t_{down}, are estimated by the mean of the Fast Fourier Transform (FFT) of the 12 constructed pressure records p1 and p2 carried out for each test pipe configuration. The FFT gives a global representation of the frequency content of these signals over the entire time domain. For the configurations with weak reach, peaks should occur at the fundamental and harmonic frequencies. They correspond to the wave reflection solicitations issuing from the weak reach boundaries. Many samples of the steady-state pressure signals for each water-hammer test and samples of the pressure taken during the valve closure with no-flow condition were analyzed in order to determine the noise level and the FFT noise peaks caused by the valve and the pump. The normalized mean FFT (RMS amplitude) of p1 and p2 inside the frequency interval [100, 400] Hz and for the "Steel+Alu1" test pipe configuration are shown in Figures 6a and 6b.

At each time, a couple of peak frequencies composed by one FFT of p1 and one FFT of p2 peaks (indicated by circles in Figures 6), is chosen. The frequency $f_{p1,p2}$ of the propagating wave between sensors p1 and p2 is then estimated according to the following equation:

$$f_{p1,p2} = \frac{f_{\max\ p1} \cdot f_{\max\ p2}}{f_{\max\ p1} + f_{\max\ p2}} \qquad (9)$$

where $f_{\max\ p1}$ and $f_{\max\ p2}$ are the frequencies at the FFT maximum peak of p1 and p2, respectively. The frequencies $f_{p1,p2}$ are then compared to the theoretical value obtained from the ratio $a_{mean} / (2 \cdot d_{p1,p2})$ where a_{mean} is the estimated wave speed of the test pipe configuration and $d_{p1,p2}$ is the distance separating the two pressure sensors. The pair of frequencies which gives the nearest $f_{p1,p2}$ frequency relative to the theoretical value is retained.

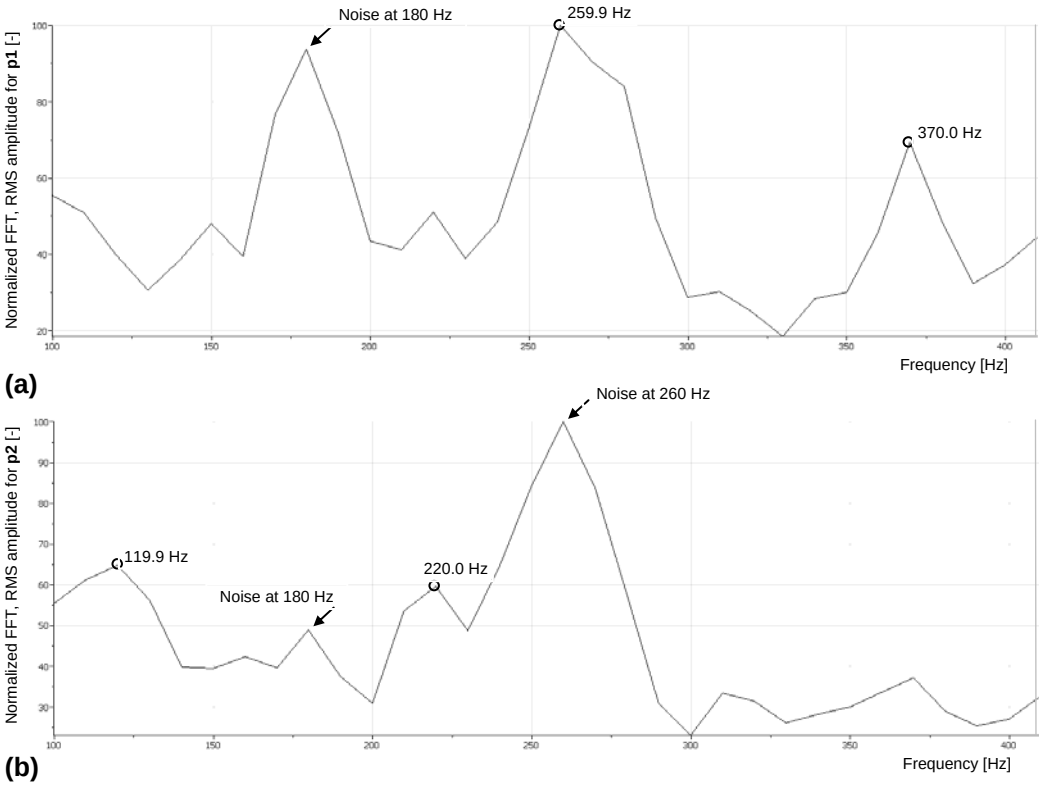

Figure 6 The mean FFT (RMS amplitude) of the 12 tests carried out on the "Steel+Alu1" test pipe configuration. a) The FFT for the constructed pressure records p1 and b) the FFT for the constructed pressure records p2

By repeating this procedure for all the test pipe configurations it was possible to estimate the approximate position of the weak reach. Figures 7a and 7b show the predicted and the real center position of the weak reaches evaluated relative to the positions of sensors p1 and p2. The differences of predicting the weak reach location relative to the sensors distance of 5.88 m are also shown on the same figures. These differences vary between 5.7% and 13.6%.

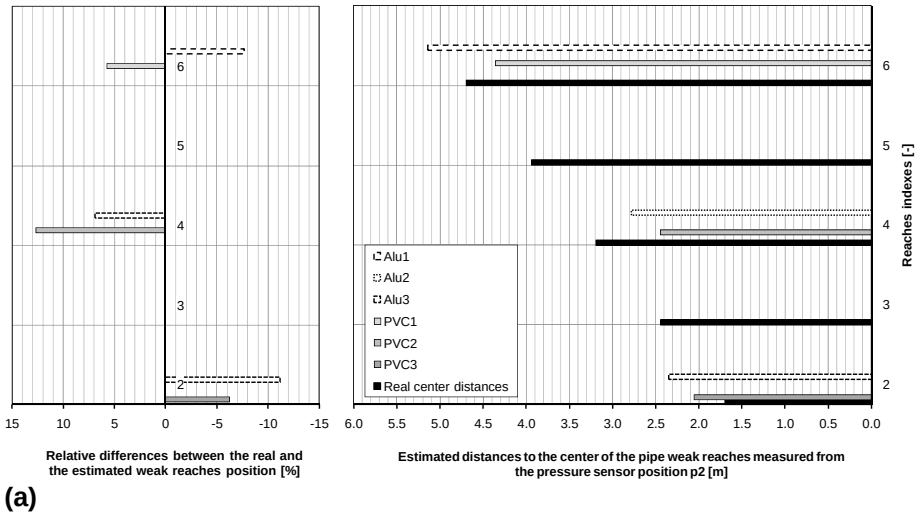

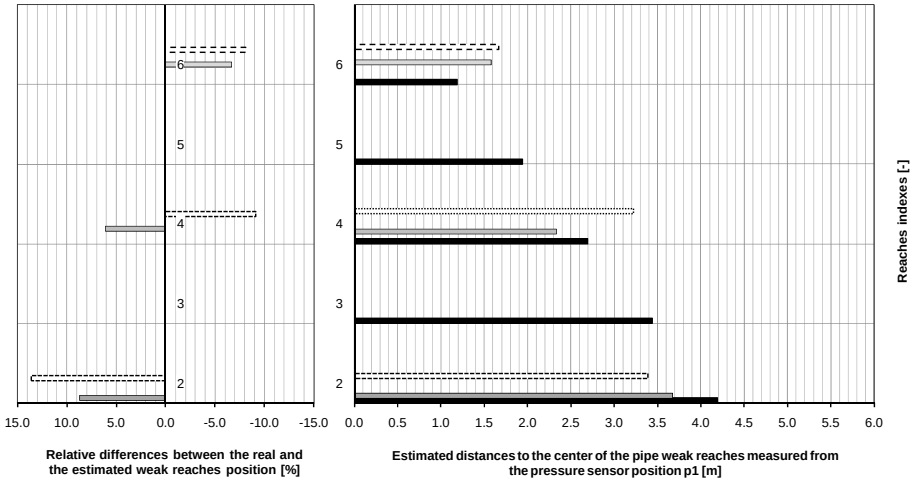

(b)

Figure 7 The estimated, real and relative differences of distances from the sensors positions to the center of the weak reach for all the tested configurations. a) Relative to position p1 and b) relative to position p2

4. CONCLUSIONS

In this paper, an experimental facility capable of producing water-hammer inside a test pipe has been described. The results of a large number of tests carried out on seven test pipe configurations have been also presented and analyzed. After a short theoretical description of the main equations that govern the water-hammer phenomenon, some general outlines of a data processing technique based on filtering and decomposition using the wavelets theory was introduced. By applying this technique on the dynamic pressure records and by using the cross-correlation methods, it was possible to estimate the water-hammer wave speed for each pipe configuration as well as the position of a 50 cm reach of aluminum or PVC that has replaced a steel reach in each of the six tested pipe configurations with weak reaches. An important drop of the estimated mean values of the wave speed has been identified in configurations with PVC reaches. This drop was smaller when aluminum reaches were used. This has made more difficult the detection of their presence based only on the measured pressure data. The approximate position of the center of these weak reaches relative to the two sensors positions has been also determined based on the Fast Fourier Transform and the estimated wave speed values. The differences in predicting the location of the weak reach relative to the distance separating the two pressure sensors vary between 5.7% and 13.6%.

The ongoing work will try to validate the estimation procedure of the water-hammer wave speed for other test pipe configurations. More analyses still to be done to enhance the methodology of localization of the weak reaches. In-situ dynamic pressure measurements at both ends of a pressure shaft of a pumped-storage power plant will also be carried out. They will give us additional information about the steepness, energy and dissipation of water-hammer wave generated during start-up and shut-down of pumps and turbines. The influence of the water temperature, turbidity, and the captured air inside the shaft on the estimation of the wave speed will be also investigated. The localization procedure of weak reaches will be implemented in purpose to detect the position of some eventual geological and geotechnical weaknesses of the rock mass surrounding the steel liner. The estimated positions will be compared to the real ones which can be obtained from the existing as-built drawings of the shaft.

5. ACKNOWLEDGMENTS

The study is part of the research project *HydroNet* for the design, manufacture and operation of pumped storage plants funded by the *Swiss Competence Center Energy and Mobility* (CCEM-CH), the *Swiss Electrical Research* and the *Swiss Office for Energy*.

6. REFERENCES

Bergant, A., Tijsseling, A., Vitkovsky, J., Covas, D., Simpson, A. and Lambert, M. (2008). *Parameters affecting water-hammer wave attenuation, shape and timing—Part 1: Mathematical tools*, Journal of Hydraulic Research, 46 (3), 373–381.

Covas, D., Ramos, H. and Betâmio de Almeida, A. (2005), *Standing wave difference method for leak detection in pipeline systems*, Journal of Hydraulic Engineering, 131 (12), 1106–1116.

Ferrante, M. and Brunone, B. (2002), *Pipe system diagnosis and leak detection by unsteady-state tests. 2. Wavelet analysis*, Advances in Water Resources, 26, 107–116.

Hachem, F.E. and Schleiss, A.J. (2010), *Detection of local wall stiffness drops in pipes using steep pressure wave excitation and wavelet decomposition*, Under reviewing process in the Journal of Hydraulic Engineering, ASCE.

Hachem, F.E. and Schleiss, A.J. (2011), *Physical tests estimating the water-hammer wave speed in pipes and tunnels with local weak wall stiffness*, under reviewing for the *2011 World Environmental & Water Resources Congress (EWRI)*, Palm Springs, California, May 22 – 26, 2011.

Halliwell, A.R. (1963). *Velocity of a Waterhammer Wave in an Elastic Pipe*, Journal of the Hydraulics Division, ASCE, 89 (HY4), 1–21.

Mallat, S.G. (1990). *A Wavelet Tour of Signal Processing*, Academic Press, San Diego, CA.

Parmakian, J. (1963), *Waterhammer analysis*, Dover, New York.

Shamloo, H. and Haghighi, A. (2009), *Leak detection in pipelines by inverse backward transient analysis*, Journal of Hydraulic Research, 47 (3), 311-318.

Taghvaei, M., Beck, S.B.M. and Boxall, J.B. (2010), *Leak detection in pipes using induced water hammer pulses and cepstrum analysis*, International Journal of COMADEM , 13 (1), 19-25.

The Mathworks, Inc. (2008). *MATLAB*, Natick, Mass. (www.mathworks.com).

Wylie, E.B., Suo, L. and Streeter, V.L. (1993). *Fluid Transients in Systems*, facsimile edition, Prentice Hall, Englewood Cliffs, NJ.

INFLUENCE OF LOCAL STIFFNESS OF CONDUITS ON WATER HAMMER PROPAGATION SIGNAL

F.E. Hachem[1] and A.J. Schleiss[2]
[1]Research assistant and [2]Professor and Director, Laboratory of Hydraulic Constructions (LCH-EPFL), Ecole Polytechnique Fédérale de Lausanne, Station 18, 1015 Lausanne, Switzerland.

In the framework of a so called *HydroNet* project (Modern methodologies for the design, manufacturing and operation of pumped-storage plants), the design criteria and the non-intrusive monitoring for steel lined pressure tunnels will be enhanced. The Fluid-Structure Interaction and the propagating wave modes during water hammer phenomena of an experimental steel pipe will be studied. The goals are to link pressure and wave signals in water to the pressure wave signals measured at the outer surface of the pipe and to detect the amplitude and location of a changed stiffness of the pipe at defined locations.

The experimental set-up consists of a steel pipe supplied with pressurized water and equipped with a shut-off valve. The pipe is divided into several reaches with different wall stiffness. The pressure fluctuations during transients at different measurement sections of the test pipe are measured. The measurement sections are also equipped with geophones. At the downstream end of the conduit pipe a hydrophone sensor is placed for acquisition of acoustic plane waves in water generated by the pressure fluctuations and pipe wall vibrations. The measured signals are processed and studied in time and frequency domains.

Based on preliminary experiments, results and their analysis regarding the influence of local stiffness of conduits on water hammer propagation signal are presented.

INTRODUCTION AND MOTIVATION

The phenomenon of water hammer in pressurized waterways has been noticed long ago [1, 2]. In former years, the safety margin for water hammer dynamic load in steel-lined pressure tunnels and shafts of hydropower plants was considered as acceptable. Because of the higher energy demands, existing plants are operating under rough conditions with relatively fast valve opening or closing to regulate the discharge. Thus, higher water hammer loads are induced. For this reason and for others related to the aging of steel liners and to the deterioration of the backfill concrete and the near rock field surrounding the liner, non-intrusive monitoring and control methods for existing steel-lined pressurized shafts and tunnels need to be enhanced [3].

Because of the Fluid-Structure Interaction, the propagating wave modes in water and in steel liner's wall during water hammer phenomena are affected by the elastic properties and stiffness of the liner [4, 5]. This fact is used as a guide to develop monitoring methods to detect, in real time, the amplitude and location of a change of wall stiffness of shafts and tunnels based on recorded signals at their both accessible ends.

In this paper, we consider that the multilayer system (steel-concrete-rock) of pressurized shafts and tunnels behaves axisymmetrically under internal loads. We suppose also that only waves that propagate along the axial direction of these structures are of interest. Under these hypotheses, the multilayer system can be modeled by one layer system. Thus, a pipe divided into several reaches with different wall stiffness is used. As long as the search for longitudinal stiffness heterogeneity is concerned, different geometric configurations of the test pipe are examined by changing systematically the position of the steel pipe flanges and by exchanging steel for PVC for some of the pipe's wall reaches.

EXPERIMENTAL SET-UP

Description of the experimental set-up

An experimental facility with a close system was assembled at the Laboratory of Hydraulic Machines of the EPFL (Ecole Polytechnique Fédérale de Lausanne). This facility was specially designed for detecting the change of wall stiffness of the test pipe using recorded data generated by water hammer phenomena inside the pipe.

The configuration of the experimental set-up (Figure 1) consists of a test pipe with 150 mm of internal diameter and 6 m of length supplied with water by a reservoir and a variable speed pump. The pipe is divided into several reaches of 0.5 m and 1.0 m long connected together with flanges having 285 mm of external diameter and 24 mm of thickness. The flanges are used also to anchor rigidly the test pipe along its length in order to minimize any longitudinal and transversal movement during the water hammer events.

On the supplying conduit of 10 m long, made of steel and PVC materials, an electromagnetic flow meter is placed to measure the steady state flow. A first control and security valve followed by an elastic deformable joint (TUBOFLEX) are located at the downstream end of the supplying conduit. This later is protected from the water hammer overpressures by a pressurized air vessel.

The downstream end of the test pipe is equipped with a shut-off valve to generate the transient events followed by a purge valve, an elastic TUBOFLEX joint and a second control valve located at the entrance of the supplying reservoir. The closure of the shut-off valve is carried out automatically using an air jack with an input and output electro-valves. The volume of air needed to activate the jack is ensured by an air compressor with a constant air pressure of 10 bars. The open and close states of the shut-off valve are detected using two diffuse sensors with infrared beam.

The data acquisition system is composed of:

- Seven pressure transducers (HKM-375M-7-BAR-A, Kulite) with a pressure range from 0 to 7 bars and an accuracy of 0.5 %.
- Five geophones (SM-6/UB 4.5 Hz, 3500 ohm, SENSOR Nederland b.v.) with a sensitivity of 78.9 V/m/s and a tolerance of ± 5 %.
- One hydrophone (CRT CR1-8298-05, Cetacean Research Technology) with a sensitivity of -197.95 dB and a capacitance of 10.01 nF.
- An NI-USB-6259 acquisition card M series with 32 analogue input channels to receive signals from the measurement equipments and with 2 analogue output channels to activate the two electro-valves of the shut-off valve. The sampling rate was fixed to 15 KHz.
- One notebook computer connected to the acquisition through a USB cable in which LabView 8.6 and Diadem 11.0 software were used for acquiring, controlling and processing experimental data.

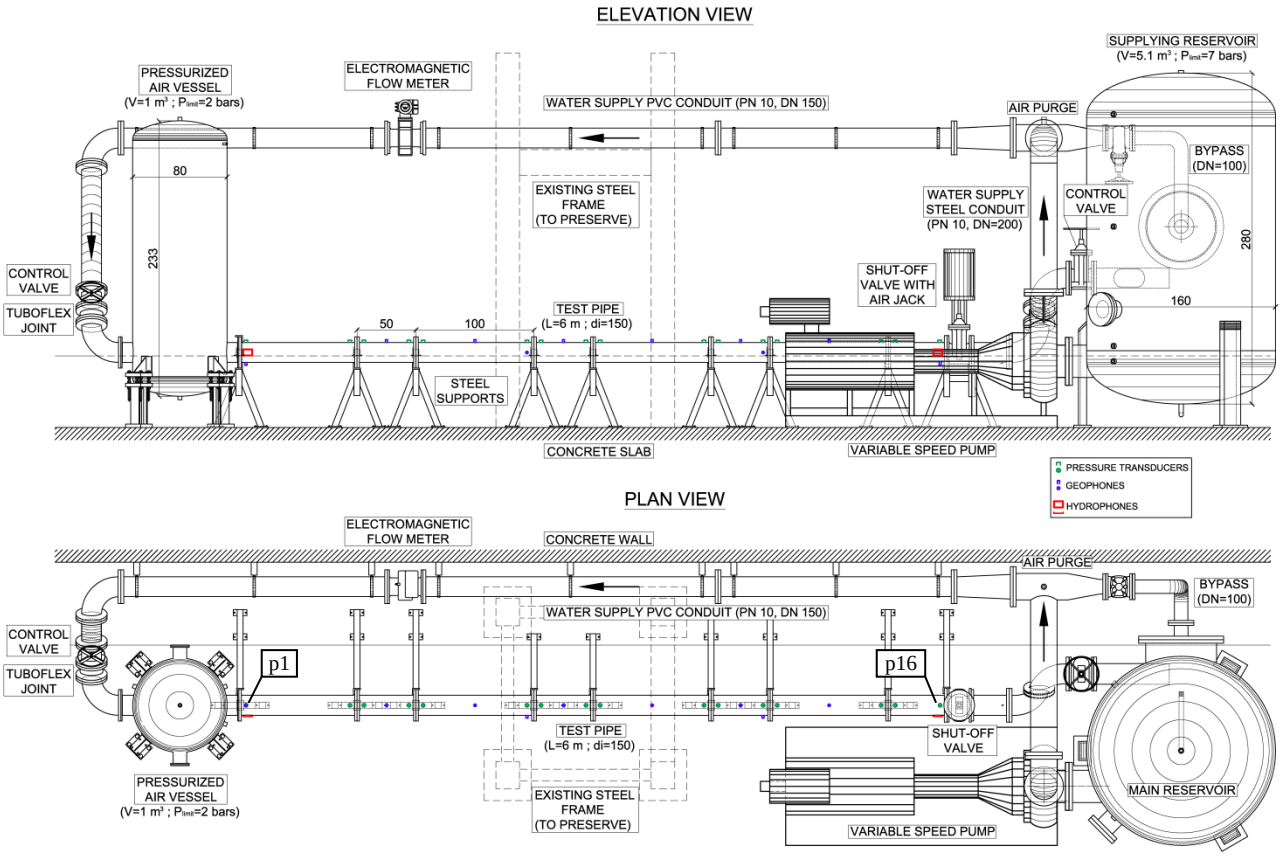

Figure 1: Elevation and plan views of the experimental facility

Test pipe configurations

Eight test pipe configurations was examined with, more or less, the same initial conditions regarding the steady flow, the mean pressure at the entrance of the test pipe and the closure time of the shut-off valve (Figure 2). Nomenclatures *A* and *B* used in the test pipe configurations correspond respectively to pipe reaches of 100 and 50 cm long. The combination of these two letters, from left to right, indicates the length of reaches that build the test pipe from upstream (air vessel side) to downstream side. The word *_STEEL* added at the end of the configuration name *ABABABAB* means that all reaches are made of steel while *_STEEL+PVC1*, *2* or *3* means respectively that the first, second or third *B* reach is of PVC type.

For each test pipe configuration, three repetitive tests with flow and three others with no-flow conditions were carried out with a defined scheme of sensors positions. Positions for sixteen pressure sensors, ten geophones and two hydrophones, according to Figure 1, were scanned with the available number of transducers. The two pressure and geophone positions at both ends of the test pipe were always equipped with sensors in all the conducted tests. The geophones can be placed on the test pipe in both longitudinal and transversal directions relative to the test pipe axis.

They can also be fixed on horizontal supports to measure the vibration velocities in both horizontal and vertical directions.

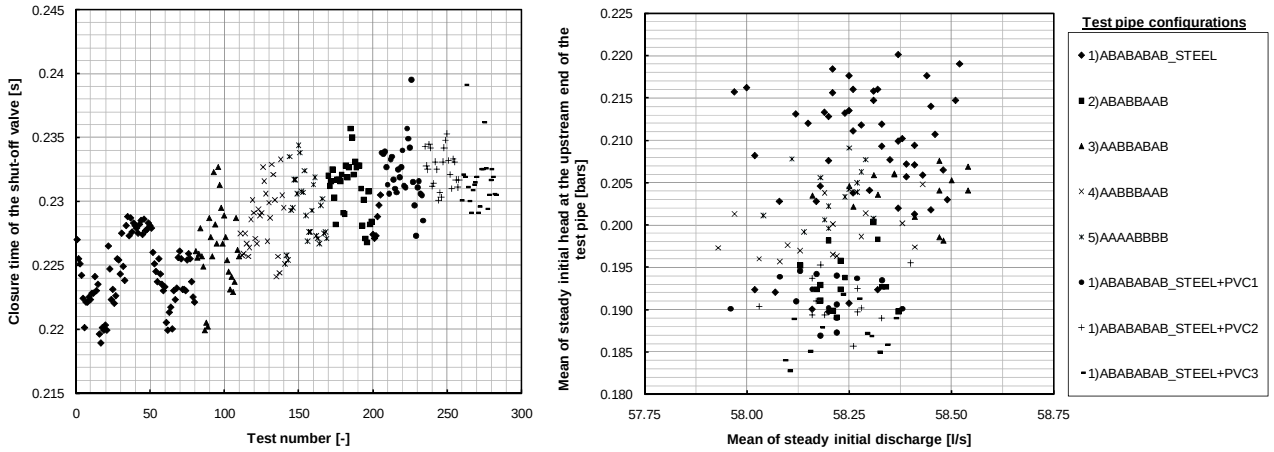

(a) (b)

Figure 2: a) Closure time evolution of the shut-off valve versus the cumulative number of tests conducted, b) Initial conditions regarding the mean head and discharge for all tests

DATA COLLECTION AND ANALYSIS

Data collection

The whole data acquisition and storage procedure starts before 2 seconds from the beginning of the valve shut-off process and ends 6 seconds after. All signals are disturbed by the vibration of the test pipe due to the impact of the valve during closing and opening maneuvers. These vibrations die out rapidly after about 0.05 seconds from the time where the valve is totally closed. In this paper, only the pressure signals collected by the pressure transducers at positions *p1* and *p16* (Figure 1) will be presented and analyzed. Some samples of the collected data are shown in Figure 3 for the eight test pipe configurations.

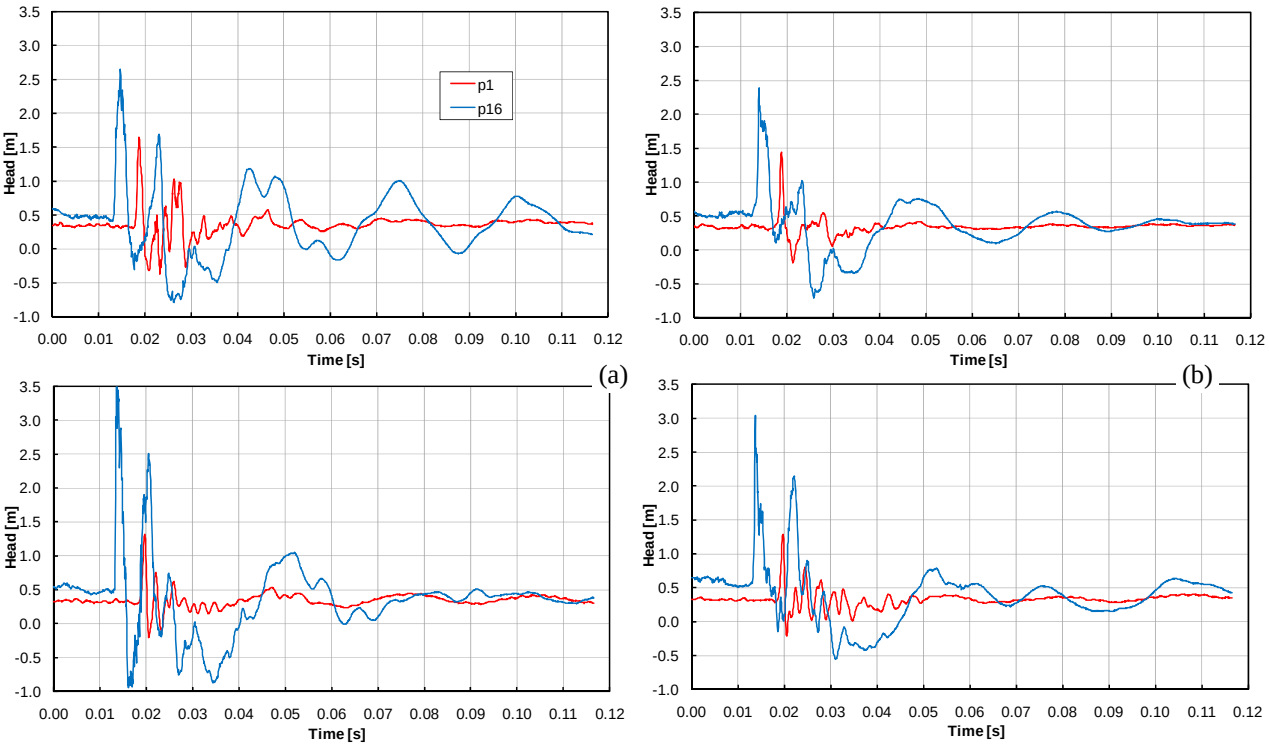

Figure 3: Transient pressure data for configurations, a) ABABABAB_STEEL, b) AABBABAB, c) ABABABAB_STEEL+PVC1 and d) ABABABAB_STEEL+PVC2

Data analysis

1. Statistical approach

First, a global analysis of the test results is done based on a statistical approach. The mean and the standard deviation of the water-hammer wave speed for each test pipe configuration are computed (Figure 4a). The wave speed calculation is conducted in the time domain. For each wave front, a reference point is defined as the intersection of the mean line of data between times 0 and 0.01 second with the line joining two points on the wave front. The travelling time Δt separating the two waves' fronts of signals *p1* and *p16* is then determined as the difference in time between the two intersection points.

An attenuation factor for the maximum pressure of the front wave, (*p16-p1*)/*p16* is also computed for each configuration tested (Figure 4b).

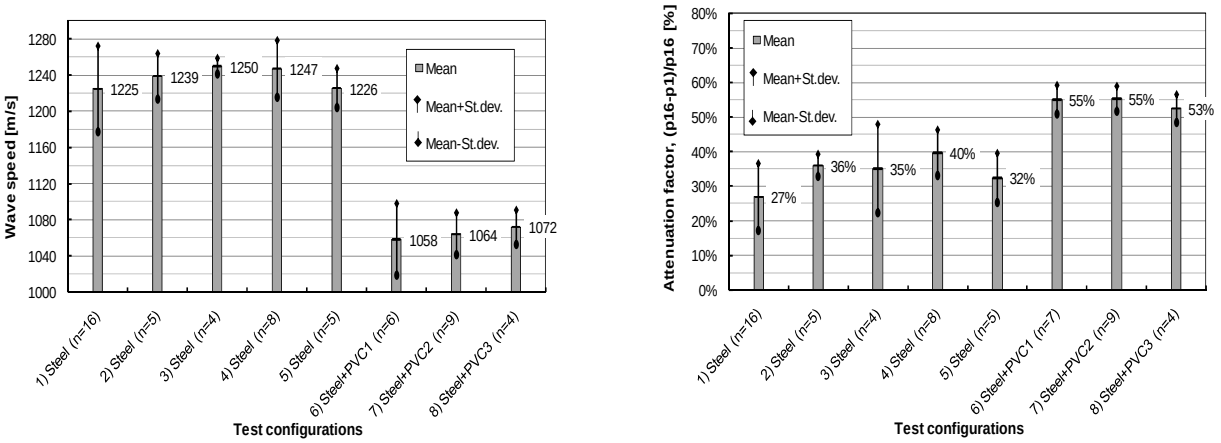

(a) (b)

Figure 4: a) Mean front speeds of water hammer wave traveling from sensor position *p1* to *p16*, b) Attenuation factors of the maximum pressure of the front wave between *p1* and *p16*

Figure 4a shows a clear difference between the mean wave speeds computed in cases where all reaches of the test pipe are of steel material and cases where a steel reach of 50 cm of length is replaced by PVC material. For test pipe configurations made of steel, the change of the position of flasks doesn't affect significantly the wave speed values. The wave speed computed between the both ends of the test pipe can be considered as a global indicator of a large change of rigidity of the pipe's wall.

The mean attenuation factor shown in Figure 4b gives also interesting results. It has smaller values in case of steel pipe configurations than those made of steel and PVC reaches. The pressure at the wave front between positions *p1* and *p16* is much more attenuated in the latter case. Similar to the mean wave speed, the attenuation factor of the maximum pressures of the wave front can be considered as another global indicator of the presence of weak zones in the pipe's wall.

2. Wavelet analysis approach

The wavelet analysis transform is used to retain information coming from the time domain analysis. Unlike the standard Fourier transform, the wavelet technique is able to capture both rapid local changes and large fluctuation in the signal [6]. Wavelet are often compared to a microscope for their ability to reveal particular aspects of the signal at different scales just by ''adjusting the focus''. As well known, the propagation of water hammer pressure waves are partially reflected when they reach a pipe region of different wall stiffness [7]. As a result, the pressure signal shows sharp variations at times corresponding to the arrival of pressure waves at the measurement sections *p1* and *p16*. By considering the wave arrival time, it is then possible to locate the change of stiffness of the pipe's wall.

The wavelet transform provides a time-frequency map called *scalogram*. Its expression for a signal $p(t)$, known also as wavelet coefficients, can be written as:

$$\widehat{p}(\lambda,u) = \frac{1}{\sqrt{\lambda}} \int p(t)\ \psi\left(\frac{t-u}{\lambda}\right) dt \tag{1}$$

where, λ and u are the dilation or scale, and the translation parameter respectively. $\Psi(\lambda,u)$ are the transform basis functions or wavelets. The translation parameter u stands for time and the scale parameter λ can be related to signal frequencies f [Hz] by the relation:

$$\lambda = \frac{f_s \cdot f_c}{f} \tag{2}$$

where, fs is the sampling frequency of the signal and fc the center frequency of a wavelet in Hz.

In this paper, only the signal of the *p16* sensor is analyzed for the two test configurations ABABABAB_STEEL (considered as the basic configuration) and AABBABAB. The Fast Fourier transform applied on to the *p16* signals for all the no-flow tests reveal the presence of peaks of frequencies below 40 Hz. These frequencies seem to be related to the principal vibration modes of the test set-up. They are lower than frequencies of interest that are higher than 100 Hz.

Figures 5a and 5b show respectively the time-scale maps (using the *Morlet* mother wavelet) of a part of *p16* pressure signals presented in Figures 3a and 3b. The lower time boundary of the analyzed signals corresponds to the arrival of the front of the first water hammer wave to sensor p16. The upper time boundary is the pipe characteristic time $T_c = 2l/a$, where l is the pipe length and a is the theoretical pressure wave speed in the test pipe. The time axis is presented in number of samples acquired at the sampling frequency *fs* (=15 kHz).

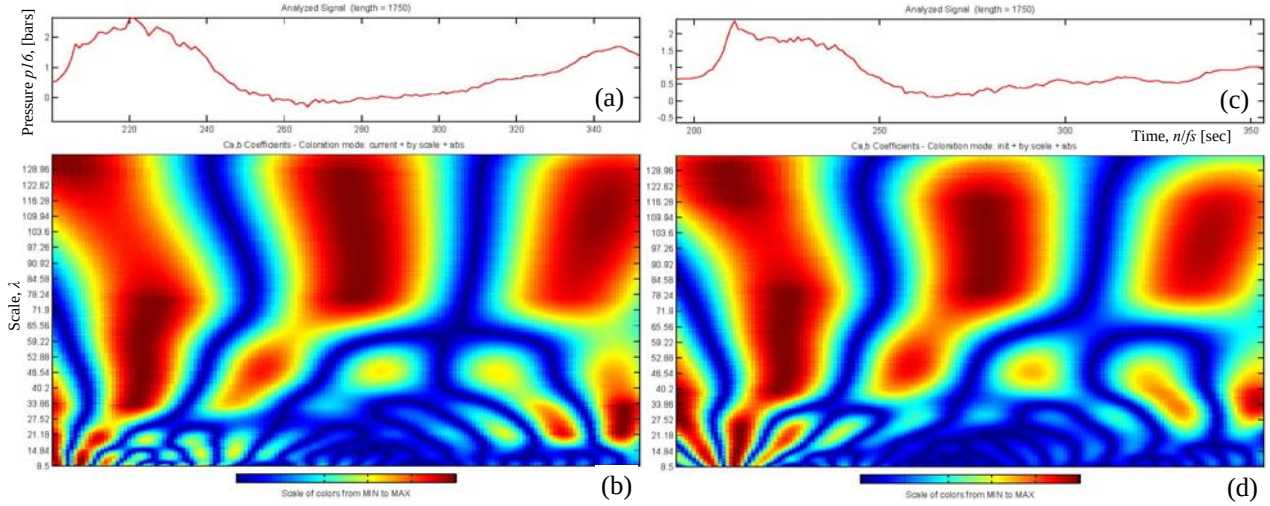

Figure 5: a) Pressure signal of the configuration ABABABAB_STEEL, b) Wavelet transform of signal shown in a), b) Pressure signal of the configuration AABBABAB, c) Wavelet transform of signal shown in b)

In the upper part (low frequencies, see equation (2)) of the two wavelet maps (Fig. 5), it can be seen clearly the periodic behavior of the water hammer oscillation mode between the valve and the air vessel. The two maps show almost the same form of valleys and mountains. In the lower part (high frequencies), the visual interpretation of the maps colors are not so easy. The examination of the wavelet coefficients values determined by equation (1) shows that many of them are very small in magnitude. Large magnitude coefficients, known as *local maxima*, are present at time points where the maximum change in the signal has occurred. Jumps or singularities in the signal can therefore be identified by the presence of these *local maxima* at specific time points in the wavelet map [8]. A less consuming alternative to the extraction of the *local maxima* line is to simply look at the decay of the wavelet coefficients across the scales for each time point [9]. Time Points where large changes occur in the signal will have large coefficients at all the different scales, thus having little decay. The measure of this decay is the *Hölder exponent* of the signal at a given time point [10]. By examining the change of this exponent in time, singularities due to the reflexion of the pressure wave from zone of different stiffness than the test pipe (flasks and PVC reaches) could be identified.

CONCLUSION

In this paper, an experimental physical facility generating water hammer phenomena has been presented in detail.

Preliminary tests showed that the wave speed of the water hammer propagation mode inside the test pipe, computed between its both ends, can be considered as a global indicator of a large change of rigidity of the pipe's wall. This change of rigidity was simulated on the test pipe by replacing a steel reach of 50 cm long with PVC material. In this latter case, the water hammer wave is slower by 14% compared to the case where all reaches are of steel material.

The mean attenuation factor between the maximum pressures of the wave front measured at both ends of the pipe has been also calculated. This factor can be considered as another global parameter of the presence of weak zones in the test pipe's wall. More attenuation was observed in case of the presence of PVC reach. The mean attenuation factor, computed for the five steel pipe configurations, is equal to 34%. In case of steel + PVC test pipe, it reaches 54%. For test pipe configurations made of steel, the change of the position of flasks doesn't affect significantly the values of the wave speed and attenuation factors.

The Wavelet analysis approach has been suggested to detect the location of the change of stiffness of the test pipe's wall. A portion of the pressure signal measured at the downstream end of the pipe has been analyzed using the *Morlet* mother wavelet type. The computed *scalogram* has shown clearly the water hammer oscillation mode of low frequency between the air vessel and the shut-off valve. For the wave oscillations with higher frequencies that include information

about the reflected waves from the change of stiffness of the pipe's wall need a more detailed investigation. The determination of the *local maxima lines* and/or the *Hölder exponent* can be used to examine the wavelet coefficients in these high frequencies zone of the *scalogram*.

REFERENCES

[1] Allievi, L., 1925. Theory of waterhammer. Translated by E.E. Halmos, printed by Riccardo Garoni, Rome, Italy.

[2] Parmakian, J., 1963. Waterhammer analysis. Dover Publications, Inc., New York.

[3] Hachem, F., Schleiss, A., 2009. The design of steel-lined pressure tunnels and shafts. The International Journal on Hydropower & Dams 16(3), 142-151.

[4] Kuiken, G.D.C., 1988. Amplification of pressure fluctuations due to fluid-structure interaction. Journal of Fluids and Structures 2, 425-435.

[5] Tijsseling, A.S., 1996. Fluid-Structure Interaction in Liquid-Filled Pipe Systems: A Review. Journal of Fluids and Structures 10, 109-146.

[6] Mallat S.G., 1992. Singularity detection and processing with wavelets. IEEE Trans Inf Theo (38), 617-43.

[7] Wylie, E.B., Suo, L., Streeter, V.L., 1993. Fluid Transients in Systems. Prentice Hall, Fascimile Edition.

[8] Mallat S.G., 1990. A Wavelet Tour of Signal Processing. San Diego, CA: Academic Perss.

[9] Ferrante, M., Brunone, B., 2002. Pipe system diagnosis and leak detection by unsteady-state tests. 2. Wavelet analysis. Advances in Water Resources 26, 107-116.

[10] Roberstone, A. N., Farrar, C. R. and Sohn, H., 2002. Singularity detection for structural health monitoring using Hölder exponents. Mechanical Systems and Signal Processing 17(6), 1163-1184.

Schweizerische Eidgenossenschaft
Confédération suisse
Confederazione Svizzera
Confederaziun svizra

Office fédéral de l'énergie OFEN

energeia.

Bulletin de l'Office fédéral de l'énergie OFEN **Numéro 3 | Mai 2010**

Interview
L'orientation des trois géants suisses de l'énergie **page 2**

Cleuson-Dixence
Le géant hydroélectrique à nouveau en service après quatre ans de travaux **page 4**

Electricité

Construire le futur

Recherche tuyaux pour prévenir les ruptures de conduites

Internet

Recherche énergétique à l'Office fédéral de l'énergie:
www.recherche-energetique.ch

Laboratoire des constructions hydrauliques à l'EPFL:
http://lch.epfl.ch

Laboratoire de machines hydrauliques à l'EPFL:
http://lmh.epfl.ch

HydroNet:
http://hydronet.epfl.ch

Les puissantes turbines hydrauliques actuelles imposent des contraintes mécaniques importantes aux puits blindés qui amènent l'eau d'un barrage à une usine électrique. Dans le pire des cas, cela peut aller jusqu'à la rupture comme en décembre 2000 sur l'aménagement de Cleuson-Dixence. En 2008, l'Ecole polytechnique fédérale de Lausanne a lancé, avec le soutien de l'Office fédéral de l'énergie et celui du consortium HydroNet du Centre de compétence énergie et mobilité, un projet de recherche visant à développer une nouvelle méthode améliorée de calcul permettant de dimensionner au mieux ces puits blindés et également de surveiller leur comportement après leur mise en service.

Nos belles montagnes sont trouées de toutes parts. Pas uniquement par des infrastructures militaires cachées, mais également par de véritables autoroutes hydrauliques qui permettent d'amener à grande vitesse l'eau d'un barrage vers une usine électrique. Dans le seul cas de l'aménagement de la Grande Dixence, dont la production électrique équivaut à quelque 4% de la consommation suisse, ce sont environ 100 kilomètres de galeries souterraines qui ont été creusées entre la vallée de Matter (Zermatt) et celle de Bagnes (Fionnay). Ces galeries sont de différents types et peuvent être revêtues d'un blindage d'acier selon la pression à laquelle elles sont soumises.

Aujourd'hui, le développement de la force hydraulique en Suisse passe notamment par l'extension des aménagements existants et l'augmentation de la puissance de turbinage. Avec pour objectif de produire de l'énergie de super pointe qui peut être injectée sur demande et dans des délais très courts dans le réseau électrique. Des questions se posent alors. Les puits blindés existants sont-ils adaptés à ces nouvelles puissances? Comment dimensionner au mieux les nouvelles galeries et puits blindés pour limiter au maximum le risque de rupture?

Acier cassant comme du verre

L'équipe du professeur Anton Schleiss au Laboratoire des constructions hydrauliques de l'Ecole polytechnique fédérale de Lausanne (EPFL) s'intéresse à toutes ces questions. «Outre l'augmentation de la puissance des turbines, explique Anton Schleiss, l'évolution des propriétés de l'acier utilisé pour le blindage des galeries et puits est aussi un paramètre à prendre en compte. Pour limiter l'épaisseur du blindage, on recourt aujourd'hui à un acier à haute performance. Inconvénient, cet acier est moins ductile que les aciers traditionnels qui sont capables de se déformer d'une manière plastique pour absorber localement de fortes contraintes. En présence de microfissures, le nouveau matériau peut casser d'un coup, comme du verre.»

Selon le professeur Schleiss, les méthodes de calcul classiques ne tiennent pas compte de cette évolution. C'est la raison pour laquelle il a lancé, en 2008 et avec le soutien de l'Office fédéral de l'énergie, un nouveau projet de recherche intitulé «Dimensionnement des galeries et puits blindés». Cette recherche, effectuée dans le cadre d'un travail de thèse par le doctorant Fadi Hachem, devrait être terminée début 2012. L'objectif est double. En premier, il s'agit de développer une nouvelle méthode améliorée de calcul pour le dimensionnement des puits blindés qui tient compte des nouvelles propriétés des aciers à haute performance. Deuxièmement, il s'agit de concevoir un dispositif de surveillance des conduites existantes. «Aujourd'hui, il n'y a pas

de surveillance directe des puits blindés, analyse Anton Schleiss. Les exploitants mesurent uniquement les éventuelles pertes d'eau entre le haut et le bas de la conduite. Or, si une perte est constatée, c'est généralement déjà trop tard.»

Le coup de bélier

Que ce soit pour développer la nouvelle méthode de calcul ou encore pour concevoir le dispositif de surveillance non invasif, le travail de recherche de l'équipe lausannoise repose sur l'analyse du signal du phénomène physique appelé coup de bélier. «Ce phénomène intervient lors d'une variation brusque de la vitesse d'un liquide dans une conduite, suite à la fermeture ou à l'ouverture rapide d'une vanne ou d'une turbine», développe Anton Schleiss. C'est le même phénomène qui s'observe, ou plutôt qui s'entend, dans les conduites des anciennes maisons. Pour le comprendre, il faut s'imaginer un train lancé à vive allure contre un mur. Alors que le premier wagon sera stoppé net au moment du choc, les suivants poursuivront leur chemin et viendront se tamponner les uns après les autres. L'eau dans la partie supérieure de la conduite poursuit également son déplacement même une fois la vanne fermée. Il en résulte une surpression dans la conduite. Cette surpression va se déplacer rapidement sous la forme d'une onde et effectuer des allers-retours dans la conduite. Au fil des cycles, l'onde va s'atténuer avant de disparaître entièrement.

«Pour éviter que l'onde du coup de bélier se propage dans la galerie d'amenée jusqu'au barrage, poursuit Anton Schleiss, une chambre d'équilibre est aménagée en amont du puits blindé. Elle peut être comparée à une voie de détresse pour l'eau. Malgré cette précaution, le coup de bélier peut encore conduire à une surpression d'environ 10%. Pour atténuer davantage encore le phénomène, il faudrait éviter les fermetures et les ouvertures trop rapides des vannes.» Or cela n'est évidemment pas dans l'intérêt des exploitants qui souhaitent au contraire pouvoir répondre le plus rapidement possible à la demande d'énergie. A noter que l'exploitation toujours plus intensive des centrales hydrauliques à accumulation pour produire de l'énergie de pointe peut également augmenter le risque d'une rupture par fatigue d'un puits blindé, en raison de coups de bélier de plus en plus fréquents.

Jusqu'à 1200 mètres par seconde

Pour développer leur nouvelle méthode de calcul ainsi que leur dispositif de surveillance, les chercheurs de l'EPFL ont construit un modèle réduit de conduite dans les locaux du Laboratoire de machines hydrauliques en plein cœur de Lausanne. Cette installation expérimentale se compose d'un tuyau en acier dans lequel circule de l'eau sous pression. Le tuyau est muni d'une valve de fermeture à l'extrémité inférieure. La conduite est divisée en plusieurs sections de différentes rigidités. «La vitesse de propagation de l'onde de pression dans le tuyau dépend de la rigidité de la conduite. Plus le tuyau est rigide, comme c'est le cas avec un acier à haute résistance, plus la vitesse est grande. Ca peut aller jusqu'à 1200 mètres par seconde, soit un peu moins que la vitesse de déplacement du son dans l'eau.»

Les différentes sections du tuyau sont interchangeables. De plus, les éléments en acier peuvent être échangés avec des éléments faits d'un autre matériau, du PVC ou de l'aluminium notamment. Des appareils de mesure de l'onde de pression tels que des sondes de pression et des microphones sont installés sur toutes les sections du tuyau ainsi qu'aux extrémités. «Grâce à cette installation, nous pouvons mesurer précisément la vitesse de propagation de l'onde de pression et sa dépendance par rapport à la composition du tuyau.» Et le chercheur de poursuivre: «Imaginons une fissure à un endroit précis de la conduite. La rigidité de la conduite et donc également la vitesse de déplacement de l'onde sont aussitôt réduites de manière très locale. Par nos mesures, nous pouvons localiser immédiatement la zone fragilisée.»

«Par nos mesures, nous pouvons localiser immédiatement la zone fragilisée.»
Professeur Anton Schleiss, directeur du Laboratoire des constructions hydrauliques à l'Ecole polytechnique fédérale de Lausanne.

Grimsel 2 examiné

Afin de calibrer le modèle théorique et de valider la procédure de surveillance, des mesures sont également réalisées sur une installation grandeur nature, l'aménagement de pompage-turbinage de Grimsel 2 en l'occurrence, en collaboration avec la société des Forces motrices de l'Oberhasli. «Des visites ont été faites à la fin 2009 pour identifier les endroits stratégiques où poser les appareils de mesure explique Anton Schleiss. La récolte des données a démarré en avril 2010 et devrait durer une année.» Il restera ensuite une année pour analyser toutes les données et développer le modèle de calcul et le système de surveillance. Une pierre à l'édifice de la sécurité des centrales hydroélectriques qui jouent un rôle central dans l'approvisionnement électrique de notre pays. Même si elles trouent nos montagnes.

(bum)

HydroNet, un consortium de recherche multidisciplinaire

L'essor des nouvelles énergies renouvelables constitue un cadre très favorable à la production hydroélectrique et plus particulièrement aux centrales de pompage-turbinage. Celles-ci permettent en effet de stocker de l'énergie électrique produite en excédant et de la restituer en période de pointe. La Suisse, où la production électrique est majoritairement d'origine hydraulique, occupe aujourd'hui déjà une position privilégiée dans ce secteur. Avec la libéralisation du marché de l'électricité, les perspectives deviennent plus intéressantes encore et elles favorisent l'accroissement des capacités de production dans le segment de l'électricité de pointe.

En Suisse comme ailleurs, d'importants investissements sont déjà engagés pour réhabiliter de vieilles centrales et pour en construire de nouvelles. Toutefois, les centrales de pompage-turbinage continuent de poser des défis techniques majeurs dans les domaines de l'hydrodynamique, de l'électricité, du génie civil et de l'environnement. Pour étudier ces problèmes et pour développer une méthodologie standardisée pour la conception, la fabrication, l'exploitation et la surveillance des centrales de pompage-turbinage, le consortium «HydroNet» a été lancé en 2007, impliquant six laboratoires suisses et partiellement financé par le Centre de compétences énergie et mobilité du domaine des Ecoles polytechniques fédérales ainsi que par Swisselectric research. Deux projets de recherche dans le cadre d'«HydroNet», dont celui intitulé «Dimensionnement des galeries et puits blindés» mené par l'équipe du professeur Anton Schleiss à l'EPFL (lire l'article principal), sont actuellement cofinancés par l'Office fédéral de l'énergie.

Pour en savoir plus:
http://hydronet.epfl.ch